Downloaded from orbit.dtu.dk on: May 06, 2023

DTU Library

Effects of temperature and ionization density in medical luminescence dosimetry using Al2O3:C

Edmund, Jens Morgenthaler

Publication date:
2007

Document Version
Publisher's PDF, also known as Version of record

Link back to DTU Orbit

Citation (APA):
Edmund, J. M. (2007). *Effects of temperature and ionization density in medical luminescence dosimetry using Al2O3:C*. Risø National Laboratory. Risø-PhD No. 38(EN)

General rights
Copyright and moral rights for the publications made accessible in the public portal are retained by the authors and/or other copyright owners and it is a condition of accessing publications that users recognise and abide by the legal requirements associated with these rights.

- Users may download and print one copy of any publication from the public portal for the purpose of private study or research.
- You may not further distribute the material or use it for any profit-making activity or commercial gain
- You may freely distribute the URL identifying the publication in the public portal

If you believe that this document breaches copyright please contact us providing details, and we will remove access to the work immediately and investigate your claim.

RISØ

Risø-PhD-thesis

Effects of temperature and ionization density in medical luminescence dosimetry using Al_2O_3:C

Jens Morgenthaler Edmund

Risø-PhD-38(EN)

I wish I didn't glow. And if he didn't constantly change my temperature I wouldn't have to open and close the window all the time. But that research idiot keeps irradiating me so I simply can't help it. I feel like a woman in her menopause."

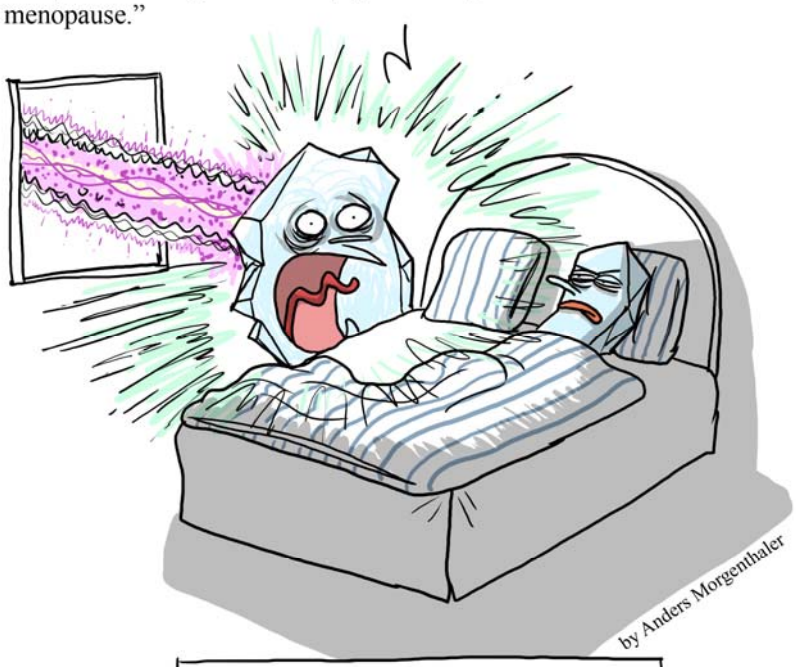

PhD destroys an otherwise well functioning crystal marriage.

Risø National Laboratory
Technical University of Denmark
Roskilde, Denmark
November 2007

DTU

Author: Jens Morgenthaler Edmund
Title: Effects of temperature and ionization density in medical luminescence dosimetry using Al_2O_3:C
Department: Radiation Research Department

This thesis is submitted in partial fulfilment of the requirements for the Ph.D. degree at University of Copenhagen

Risø-PhD-38(EN)
November 2007

Abstract (max. 2000 char.):

A new system containing small crystals of aluminum oxide doped with carbon (Al_2O_3:C) attached to optical fiber cables has recently been introduced.
During irradiation, the system monitors the radioluminescence (RL) from the crystals and after irradiation, an optically stimulated luminescence (OSL) signal can be read out by stimulating the crystal with light. This thesis applies the initial part and the total area of the resulting OSL decay curve for dosimetry measurements and investigates the effects of temperature and proton energy, i.e. ionization density, on the RL and OSL signals from Al_2O_3:C.
In the temperature study, it was found that the OSL signal depends on both irradiation and stimulation temperature while the RL signal is effected only by the irradiation temperature. The initial OSL signal is increasing with temperature whereas the total OSL area is decreasing. Therefore, if the irradiation temperature is kept constant, one can find an integration time which provides an OSL signal independent of stimulation temperature.
Overall, the RL and OSL signals vary between -0.2 to 0.6% per C. Thermal effects were simulated with a band structure model and indicated that the temperature effects are caused by the combined efforts of energetic shallow traps and thermal excitation from intermediate states in deeper traps.
In the study of ionization density, we investigated protons with energies between 10 and 60 MeV (4.57 to 1.08 keV/µm in water). Experimentally, we observed that the initial OSL signal provided a signal independent of linear energy transfer (LET) for all energies at 0.3 Gy. The total OSL area showed an LET dependent behavior at all doses and energies. We used track structure theory (TST) to give possible explanations for the LET dependence of the OSL signal. From these calculations, we found that the initial OSL signal is, in general, not LET independent which makes Al_2O_3:C unsuitable for OSL proton dosimetry. The initial OSL signal can, however, be combined with the total OSL signal to provide an LET independent response for a given dose and LET interval. On the basis of TST, we estimate a so–called “target radius” to be between 30 and 150 nm and associated this radius with a charge migration distance in the crystal.

ISBN 978-87-550-3643-7

Contract no.:

Group's own reg. no.:

Sponsorship:

Cover :

Cover by courtesy of Anders Morgentahler

Pages: 139
Tables: 5
References: 99

Information Service Department
Risø National Laboratory
Technical University of Denmark
P.O.Box 49
DK-4000 Roskilde
Denmark
Telephone +45 46774004
bibl@risoe.dk
Fax +45 46774013
www.risoe.dk

Contents

1 Introduction

According to the World Health Organization (WHO), more than 11 million people are diagnosed with cancer every year with an estimated 1.1 million people in 2005 for Europe alone [83, 69, 38]. The incidence of cancer is increasing with our increased lifespan and by the year 2020, the number of people diagnosed with cancer is estimated to be 16 million per year, an increase of about 50% relative to the present level. In Denmark (2007), roughly 30000 people are annually diagnosed with cancer and despite extensive research only about 45% of the cancer patients are successfully cured, i.e. survives for more than five years without further symptoms. Around 22% of diagnosed cancer patients are cured through surgery alone, 18% by radiation therapy alone or in combination with either surgery and/or chemotherapy, and the remaining 5% by chemotherapy alone or in combination with surgery [87, 18, 32]. The objective of radiation therapy is the destruction of cancer tissue by means of radiation.

Therapeutic radiation oncology requires delivery of highly localized doses of radiation to patient target tissue and organs infected with cancer. It is inevitable that healthy organs and tissue will also be exposed during treatment and overexposure carries with it a concomitant risk of secondary cancers. In addition, underexposure is likely to induce cancer in healthy tissue without killing the tumor. Both tumor control and normal tissue complication probabilities are steep functions of absorbed dose and therefore the efficiency of the treatment requires knowledge of the absorbed dose at the target organ to better than $\pm 5\%$ with a higher risk of local recurrence or a higher risk of complications resulting from incorrect exposure [46, 78]. It is necessary to take all possible measures to reduce the toxicity effects of undesired exposure to a minimum. This requires the accurate calibration of radiotherapy sources, the accurate positioning and fixation of patients and the ability of precisely planned dose delivery at critical locations within the body. Furthermore, quality assurance and dose verification of treatment plans are necessary to avoid accidents due to, for example, incorrect positioning or calibration. This

in turn requires the ability to perform precise dosimetry since improper use of dosimeters in medical applications may lead to unacceptable bias and large uncertainties in the dose estimation.

The need for small, unobtrusive radiation dosimeters capable of performing real-time, i.e. during irradiation of the patient, or near real-time measurements on, and preferably inside, the patient is increasing due to the increased complexity of the treatment techniques. In fact, *in–vivo* dosimetry has been recommended as a possible tool to avoid accidents in radiation therapy [46]. This could, for example, be intensity modulated radiation therapy (IMRT) for external radiation treatment (teletherapy) or internal brachytherapy or in the use of radiopharmaceuticals. Patient monitoring has so far been carried out with radiochromic dye films, plastic scintillators, diode detectors, MOSFET[1] detectors or thermoluminescence (TL) dosimeters. In TL dosimetry, the readout system is not coupled directly to the detectors and requires a separate post-irradiation read out evaluation of the dosimeters thereby excluding real-time dose estimates. Recently, electronic portal imaging devices (EPIDs) mounted on medical linear accelerators are being used for dosimetry by providing two dimensional portal dose maps from the acquired portal images. Portal dosimetry is, however, not yet provided on a routine basis.

In this thesis, we will use a newly introduced system that monitors the radioluminescence (RL) and the optically stimulated luminescence (OSL) signal from small carbon doped aluminum oxide (Al_2O_3:C) crystals to investigate the effects of temperature and ionization density on dose determination. Since the luminescence phenomenon plays a key role in this study we will consider it in more detail first in this introduction. Hereafter, the applications of TL, RL and OSL in medical dosimetry are reviewed and finally, the investigation of temperature and ionization density effects is explained more extensively.

1.1 Luminescence

When part of the energy absorbed by a material is re-emitted as light we name this process luminescence. It is a light emission representing an excess over black body radiation that lasts for a time exceeding the period of electromagnetic oscillation ($< 10^{-15}$ s). In luminescence, there are intermediate processes between absorption and emission which exceed the period of electromagnetic oscillation and as a result luminescence looses correlation between phases of absorbed and emitted light in contrast to reflected light, where a phase correlation is always observed. The delay between absorption

[1] Metal oxide semiconductor field transistor.

of energy and re-emission of light is determined by the lifetime of excitation states and based on practical observations, two types of luminescence has historically been established - fluorescence and phosphorescence. The distinction between the two is the delay time in emission. If we characterize the time after exposure before emitting light by a constant τ, the light is characterized as fluorescence for $\tau < 10^{-8}$ s and as phosphorescence for larger τ (including seconds, hours or even days) [59]. Fluorescence is used in everyday practical applications such as industrial and residential lightning (neon and fluorescent lamps). Phosphorescence glowing lasts long after the excitation source is gone. This effect is, for example, used with road signs to attract drivers attention.

A number of different ways by which energy is deposited in a material can result in the production of luminescence. These include mechanical energy (triboluminescence), electrical energy (electroluminescence) and excitation by optical or ultra-violet light (photoluminescence). Electroluminescence is created by applying an electromagnetic field in the material where electrical discharge results in excited molecules that emits light. Light emitting diodes (LEDs) is probably the most well-known application of electroluminescence. Triboluminescence occurs when a material is scratched, crushed, rubbed or stressed mechanically in any way. This stress results in electrical charge being produced which recombines and produce light. Since electrical discharge is the foundation of triboluminescence, it can be classified as part of electroluminescence. Blue or red triboluminescence can be observed when sawing a diamond during the cutting process. Photoluminescence represents any process in which a material absorbs electromagnetic energy at a certain wavelength and emits a part of it at a different (usually longer) wavelength. The part of the energy not re-emitted ends up as molecular vibrations or simply as heat.

When the energy deposition in a material is caused by ionizing radiation like γ-rays, β-particles, X-rays or heavy charged particles (HCPs), we term the resulting production of prompt light radioluminescence (RL) or scintillation. The emitted light has a longer wavelength than the incident radiation and is thus a characteristic property of the irradiated material and not of the radiation itself. Radioluminescence is widely used in medical physics, dosimetry, television and radar screens.

1.1.1 Stimulated relaxation phenomena

The absorption of energy from ionizing radiation by an insulator or a semiconductor causes the excitation of free electrons and holes and the subsequent trapping of these charge carriers at defects within the material. The radia-

tion absorption and excitation of charge leads to a perturbation of the system from a state of thermodynamic equilibrium to a metastable state. The system will eventually return to equilibrium by relaxation but this could take days, months or years depending on the stability of the pertubated state. The system can, however, be stimulated such that it relaxes back to thermodynamic equilibrium faster. During the relaxation process recombination of the electrons with holes occurs and, if the recombination is radiative, luminescence is emitted [22].

OSL is just one member of a family of stimulated relaxation phenomena. Here, the stimulating energy source is light, i.e. UV, visible or infra red. The intensity of the emitted luminescence is related to the rate at which the system returns to equilibrium. This rate is a function of the concentration of trapped (metastable) charge and the intensity of the stimulating light. In the simplest (first-order) case with constant stimulation intensity, the rate is linearly proportional to the trapped charge concentration. Normally, one monitors the intensity of the luminescence as a function of stimulation time, resulting in a characteristic luminescence decay curve. In this readout mode, termed continuous wave OSL (cw-OSL), the intensity of the stimulating light is constant and the luminescence monitored during stimulation. The integral of the curve is thus related to trapped charge which in turn is proportional (in the ideal case) to the initial dose of the absorbed radiation. This is the basis of OSL in radiation dosimetry (see figure 1.1).

Only a very small fraction of the radiation energy is available from the metastable states and both the OSL and TL efficiency is low compared to luminescence induced by other means.

- In black body radiation $\sim 5\%$ of the thermal energy is re-emitted as light.
- In photoluminescence $\sim 20\%$ of the photon energy is re-emitted as light.
- In cathodeluminescence $\sim 10\%$ of the electronic energy is re-emitted as light.
- In electroluminescence 0.1-50% of the energy from the applied electromagnetic field is re-emitted as light.
- In TL, only 0.01-1% of the energy provided by the ionizing radiation is re-emitted as light [20, 54] and similar efficiencies are seen for OSL.

In other stimulated relaxation phenomena, the form of stimulation may differ and the monitored signal during stimulation may be different. In TL,

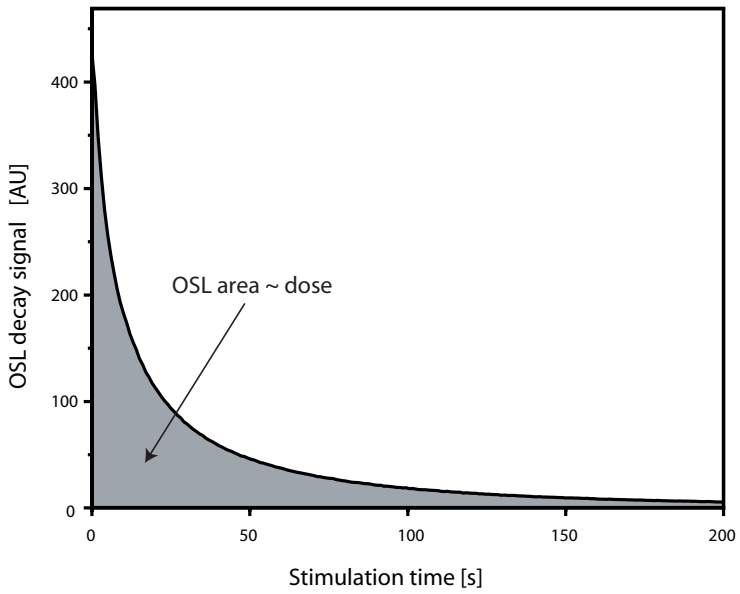

Figure 1.1: A cw-OSL decay curve from Al_2O_3:C crystal after a 2.7 Gy irradiation with a ^{137}Cs γ-source. The area under the OSL curve is ideally proportional to the dose.

the luminescence is stimulated thermally by heating the sample. In thermally stimulated conductivity (TSC) or photoconductivity (PC), the signal monitored is the freed charge during the migration through the delocalised bands. For thermally or optically stimulated exoelectron emission (TSEE or OSEE), the signal is the exoemission of electrons from the surface of the sample during the relaxation process.

Thermoluminescence dosimeters (TLDs) and optically stimulated dosimeters (OSLDs) both measure dose by the emission of light from a solid state insulator or semiconductor[2]. The signal is usually characterized as phosphorescence and provides information about the accumulated dose. Due to the close resemblance between TL and OSL and the fact that TL is a very well-established technique, it is useful for the discussion to devote further attention to existing TL medical applications.

1.1.2 Thermoluminescence

TL should not be confused with light spontaneously emitted from a substance when it is heated to incandescence (black body radiation). TL is thermally stimulated emission of light following the previous absorption of radiation.

[2]Metals do not have luminescence properties.

A TL material is thus a material that during exposure to ionizing radiation absorbs some energy which is stored. The stored energy is released in the form of visible light when the material is heated. This means that a TL material cannot emit light again by simply cooling the sample and then heating it again.

TLDs have been widely used since the 1950s in a number of applications with different materials. These applications include personal dosimetry, environmental and retrospective dosimetry, geological and archaeological dating, and in a variety of medical applications such as radiation therapy, diagnostic radiology and radiotherapy mailed dosimetry. For diagnostic radiology, a dosimeter with a flat energy response to low energy photons is preferred. For mailed dosimetry, where the TL material may be exposed to extreme environmental conditions, low fading is important. Fading is the spontaneous loss of signal with time. In dosimetric applications where the dose distribution is steep, such as brachytherapy or teletherapy, a small physical size of the TL element is an obvious requirement. Radiation therapy often involves dose levels where many TL materials exhibit a so-called supralinear dose-response curve and a dosimeter with linear response characteristics provides a clear advantage. The typical doses of interest in radiation therapy dosimetry can be 2 Gy [25].

For many years, lithium fluoride doped with magnesium and titanium (LiF:Mg,Ti) has been the workhorse of TL medical dosimetry. It is normally available in three commercial versions named TLD-100, TLD-600 and TLD-700 depending on the concentration of the two natural lithium isotopes ^{6}Li and ^{7}Li. LiF:Mg,Ti is popular because of its high TL sensitivity[3] and good tissue equivalence. By "tissue equivalence" we mean that the dosimeter material receive the same absorbed dose as tissue when exposed to an equal amount of radiation. The prime parameters are the effective atom numbers, Z_{eff}, and the density but the degree of tissue equivalence may depend on the radiation quality under consideration. For example, for low energy radiation ($\sim$ keV) where the photoelectric effect is important, Z_{eff} of the dosimeter material and tissue (water) should be similar whereas for higher energies, where Compton scattering is dominating, the electronic densities should be very close. Human tissue has a Z_{eff} equal to 7.6 and Z_{eff} for LiF:Mg,Ti is equal to 8.31 [49]. In recent years a relative new material LiF:Mg,Cu,P has attracted the attention of the medical dosimetry community. The TL characteristics of this material are particular useful for clinical radiation dosimetry due to a high sensitivity compared to LiF:Mg,Ti, an almost flat photon energy response, a low rate of fading and a linear dose response [66].

[3] In contrast to the TL sensitivity, the OSL sensitivity of LiF:Mg,Ti is not very high.

1.2 The development of OSL

The OSL technique was first suggested as a dosimetry tool in the 1950s and 1960s but did not become a practical tool in radiation dosimetry due to strong fading, i.e. loss of signal over time. However, in the 1980s advances in the optical instrumentation were made and the OSL technique became popular in the archeological and geological dating community as a method of dose determination in natural materials like quartz and feldspar. For example, since the late 1980s, the Health Physics Instrument Development Group at Risø National Laboratory in Denmark has been involved with the development and research of OSL techniques resulting in the so-called Risø reader capable of performing both OSL and TL measurements (TL/OSL-DA-20). The system has found worldwide use in research within dating, retrospective and personal dosimetry [21].

The ideal OSL material should satisfy several characteristics. It should have deep thermally stable traps for long-term storage of dosimetric information without significant fading at room temperature. These traps should at the same time be optically accessible using light sources with wavelengths well separated from the emission bands of the recombination centers. There is no fundamental difference between TL and OSL materials and all efficient dosimetric phosphors might exhibit both TL and OSL properties. The real advantage of some of the materials in comparison with others is simply in the right combination of thermal and optical energy depths of the traps, in good separation between emission and stimulation bands and a large ionization cross-section of the traps. Single crystals of anion deficient aluminum oxide doped with carbon (Al_2O_3:C), first developed as a highly sensitive TL material was found to satisfy all these requirements and became widely used as an OSL dosimeter [7, 6]. During the 1990s, this material together with a pulsed OSL (POSL) readout protocol were introduced for personal dosimetry and are, for example, available today as the commercial system Landuer Luxel^{TM} [22, 64, 9]. In POSL, the OSL signal is recorded between stimulation pulses as opposed to cw-OSL where the OSL signal is recorded during stimulation.

1.2.1 OSL and RL in medical dosimetry

At the beginning of the new millennium, research was initiated to investigate the potential use of the OSL technique and Al_2O_3:C in medical dosimetry [61, 72, 71, 29, 28, 43]. About this time at Risø, the idea of attaching luminescent crystals to optical fiber cables emerged and in 2001 this was specified to a single-fiber approach in which both stimulation and luminescence light can be transported. An all-optical luminescence fiber system for real-time

in–vivo dosimetry in radiotherapy was developed [10]. Small ($\sim$ 0.5 mm) Al_2O_3:C probes are attached to 10-15 m optical fiber cables and placed inside a patient. In addition to the accumulated dose information provided by the OSL, the prompt RL signal generated by the therapy radiation source directly reflects the dose rate at any time during treatment. Thus, the main advantage of optical fiber dosimeters in clinical applications are the capability of measuring both real-time dose rate and accumulated dose (see section 3.1). The first paper describing the RL/OSL system was published in 2002 at the international symposium of IAEA in Vienna [10]. In 2003, the first patient measurements were carried out in mammography and radiotherapy to investigate the systems ability to function in both the diagnostic ($\sim$ mGy) and therapeutic ($\sim$ Gy) area of medical dosimetry [15, 16, 14].

The application of the RL signal from Al_2O_3:C for dose rate measurements is complicated for two reasons. The first problem is that radiation-induced light from the optical fiber cable itself (primarily Čerenkov light and fluorescence) is not always negligible compared with the RL signal generated in the probe. This problem is usually referred to as "the stem effect". The second problem is that the RL signal from Al_2O_3:C is not simply proportional to the absorbed dose rate but depends on the accumulated dose.

A Čerenkov signal emerges from the dosimeter and fiber when exposed to high-energy radiation and since the fiber is considerable larger than the dosimeter the Čerenkov signal from the fiber dominates. This signal has a physically different origin than the RL signal and they cannot be easily distinguished in many cases. This stem effect carries with it no spatial information since an unknown length of the exposed fiber contributes to the signal as opposed to a small dosimeter. Thus if the stem and RL signals are not separated spatial information is lost. The stem signal may scale with the dose rate as well as the field size, i.e. the amount of fiber exposed.

There are several ways to overcome the stem effect. With the introduction of a gated fiber system [26, 50] for pulsed linear accelerator beams, the prompt Čerenkov light and fluorescence from the fiber cable can be separated in time from the delayed RL crystal response. This delay is due to a forbidden triplet–to–singlet transition in the recombination center (known as the F–center) of Al_2O_3:C which has a life time of about 35 ms [55].

Polf et al. designed a dual-fiber system for real time dose monitoring [73, 71]. The procedure for real-time OSL involves the periodic pulsing of the optical stimulation simultaneously with the irradiation while monitoring the luminescence emission. Note that although the stimulation is pulsed, the OSL monitored is cw-OSL, i.e. the OSL is monitored during the optical stimulation, the period of which is longer that the lifetime of the intrinsic luminescence emission (35 ms in Al_2O_3). RL is measured in the periods be-

tween pulses while the OSL+RL is monitored during the stimulation periods and by subtraction, the OSL signal can be extracted. Since the OSL signal does not suffer from stem effects, the subtraction will eliminate this effect.

The dependence of RL signal on accumulated dose has also been addressed. Andersen et al. presented an algorithm which corrects for sensitivity changes in the RL signal in a purely empirical way [13]. With a known initial sensitivity of the Al_2O_3:C probe and with the pre-calibrated dose dependence of the sensitivity, the estimation of the accumulated absorbed dose and dose rate is performed in parallel with an iterative sensitivity correction. Gaza et al. developed an algorithm to correct for sensitivity changes using the real-time OSL protocol. An advantage of this protocol is the lack of saturation effects. Instead, a dynamic equilibrium between the processes of trap filling during irradiation and depletion during stimulation will occur for a sufficiently long irradiation at a fixed dose rate. However, a rather complicated correction algorithm must be applied to keep track of the charge population level in the so-called OSL trap [28].

The applicability of the Risø RL/OSL system in medical dosimetry was tested using therapeutic photons beams and soft X-ray beams at radiotherapy facilities at Malmö University Hospital (Sweden) and Copenhagen University Hospital (Denmark) by Aznar et al. [14]. From a clinical point of view it was important to evaluate the ability of a new dosimeter to resolve depth dose distributions and lateral profiles compared to well-established dosimeters. The RL and OSL data were compared with those obtained using a commercially available p-doped Si-diode detector and an agreement better than 1 % was found between the diode and the RL/OSL probes. These results showed that the spatial resolution of the RL/OSL system makes it suitable for measurements of depth and lateral dose distributions in clinical photon beams. At radiotherapy energies, the variation of the signal with beam parameters was overall smaller than 2%. Treatment-like experiments in phantoms, and *in–vivo* measurements during complex patient treatments (such as IMRT) indicated that the RL/OSL dosimetry system could reliably measure the absorbed dose within 2%. On the basis of these results, it was concluded that the RL/OSL dosimetry system showed a considerable potential for applications in both radiotherapy and mammography.

1.3 This thesis

The promising results of the RL/OSL dosimetry system for clinical applications motivated further research to study some basic dosimetric properties of Al_2O_3:C in more detail. One of the fundamental problems of the OSL signal

from Al_2O_3:C is the rate with which it decays, i.e. the rate of which the system returns to equilibrium. In the ideal case, the area under the OSL decay curve increases linearly with dose (trapped charge concentration) effecting only the amplitude of the signal and leaving the rate of decay unchanged. In this ideal situation, applying any part of the OSL signal will result in the same dose estimate. However, the OSL decay of Al_2O_3:C changes shape with dose, temperature and ionization density as illustrated in figure 1.2.

1.3.1 Effects of dose

The left panel in figure 1.2 illustrates how the OSL signal decays faster with increasing dose. Furthermore, as shown qualitatively in figure 1.3, it has been established that the total area under the curve is not increasing proportionally with dose [98, 95]. This provides us at least two important pieces of information. First, the increase in decay rate is not merely a redistribution of an otherwise dose-proportional signal with a larger and larger fraction of this signal being read out in the beginning of the stimulation as the dose increases. Secondly, the shape of the dose-response curve based on the OSL signal is going to depend on which part of the OSL signal that is being used (see figure 1.3).

The OSL decay rate of Al_2O_3:C also depends on other factors than dose and here, we address the effects of temperature and proton energy on the OSL signal. The influence of these quantities are shown in the middle and right panel of figure 1.2. As is the case with dose, the OSL decay rate increases with temperature whereas it decreases with proton energy. In order to make general statements, it is necessary to investigate both the temperature and energy effects at different doses.

1.3.2 Effects of temperature

The RL/OSL system is suitable for *in–vivo* dose verification in radiotherapy of cancer patients which, if not for other reasons, introduces a temperature issue [25]. The Al_2O_3:C crystal may, as an example, be calibrated outside the patient at room temperature while the measurement is obtained at body temperature by placing the crystal inside a body cavity of the patient (see figure 1.4). As already mentioned, radiotherapy is subject to strict precision requirements because small deviations in the target dose may cause damaging rather than curative effects. An overall uncertainty better than 5 % in radiation therapy is usually a requirement and *in–vivo* dose verification should consequently have an uncertainty smaller than this to detect errors

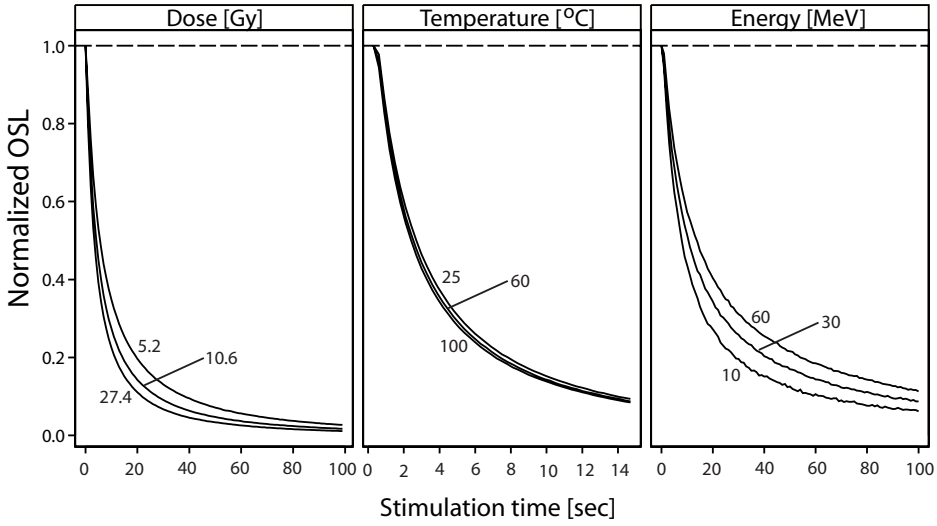

Figure 1.2: The change in OSL decay rate with dose (left), temperature (middle) and proton energy (right). Left panel: The doses were given with a ^{137}Cs γ-source and numbers are in Gy. Middle panel: A constant dose of 2.4 Gy was given with a β-source and numbers indicate the temperature in °C. Right panel: A constant dose of 0.25 Gy was given with protons of different energy corresponding to the numbers in MeV.

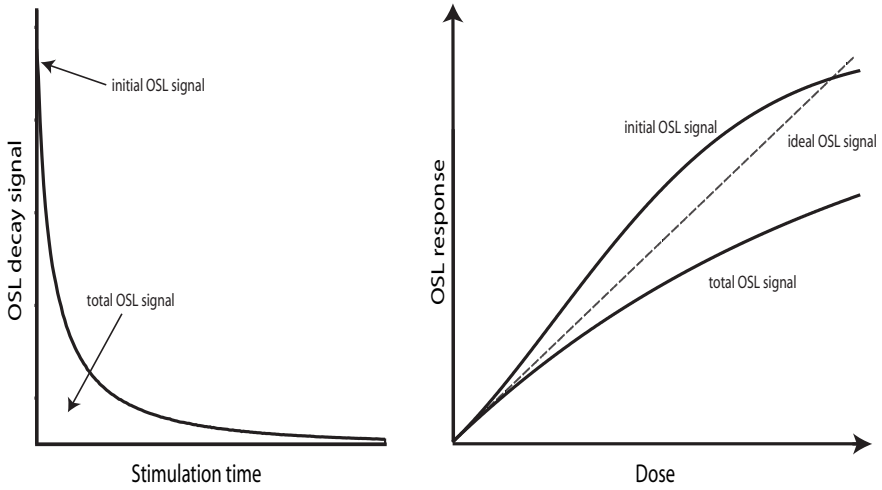

Figure 1.3: Illustration of the consequence on the dose-response curve of using different parts of the OSL signal. The initial part of the OSL signal gives a supralinear dose-response, i.e. the response increases more than twice when doubling the dose, while the total OSL signal gives a sublinear dose-response, i.e. the response increases less than twice when doubling the dose, compared to an ideal detector signal which gives a linear dose-response.

of that order. One significant contributor to uncertainties in most OSL ma-

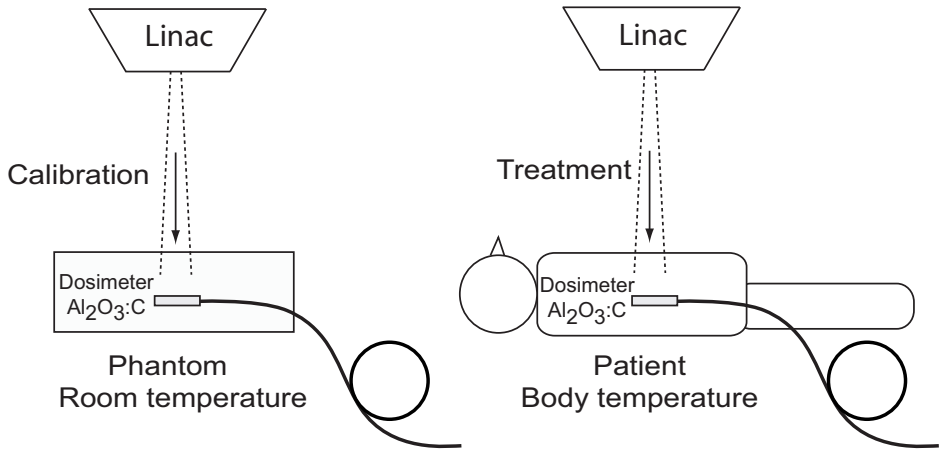

Figure 1.4: Principle of temperature effect. The Al_2O_3:C crystal (attached to a fiber cable) is calibrated in a phantom at room temperature while the treatment measurement is carried out *in–vivo* at body temperature. A typical clinical radiation accelerator is the electron linear accelerator (linac) as shown in the figure [86].

terials is the temperature dependence of the luminescence signal. In this thesis, we analyze and characterize how both the OSL and RL signal change when the irradiation and/or the stimulation temperature is changed. For *in–vivo* dosimetry, the primary concern is the difference between room and body temperature.

1.3.3 Effects of proton energy

As will be demonstrated later, the energy of protons is directly related to the density of ionizations they cause in the target material. Over the last years, particle therapy with protons has gained increasing interest due to the advantages of this treatment compared to conventional external beam therapy with high energy photons. Today about 25 facilities treat patients with protons worldwide and more than 20 new facilities (mainly hospital based) are under construction or are being planned within the next five years [81]. Approximately 40000 patients have already been treated with proton therapy and over 4000 with HCPs like carbon ions [69]. Protons are well-suited for radiotherapy because they exert their greatest effect deep within the body, inside the tumor, and thus allow healthy tissue to be better protected than by traditional radiation therapy (see figure 1.5). This is particularly useful for treatment of eye or brain tumors because of the very sensitive tissue and organs in this region of the human body. The energy of the protons can be adjusted such that the dose peak is placed in the tumor while the dose

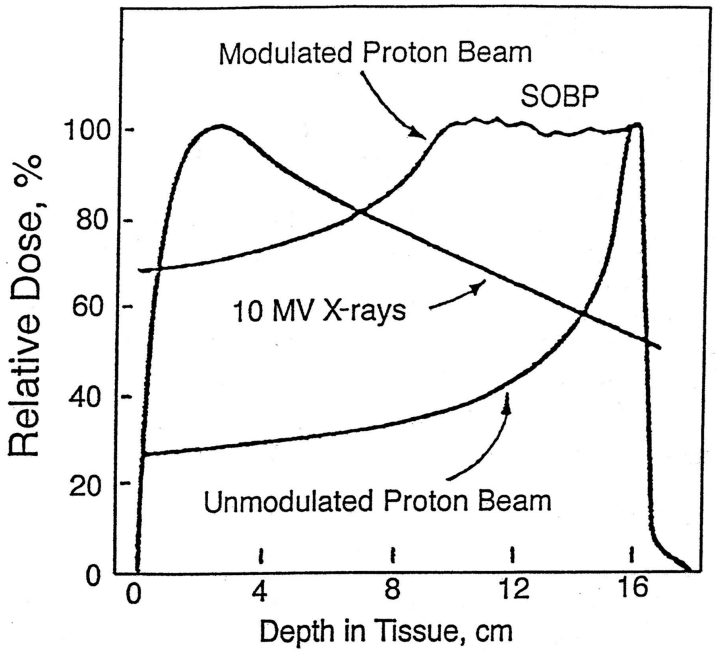

Figure 1.5: A depth–dose curve in tissue for 10 MV photons and 160 MeV protons. The depth–dose curve of protons is also referred to as a Bragg–curve and the dose peak as the Bragg peak. The Bragg–curve can be spread out by a modulator resulting in a constant elevated dose level referred to as a spread out Bragg peak (SOBP). The figure is a reprint from [82].

plateau is placed in the healthy tissue. With the use of a modulator, Bragg peaks of different energies can be superposed resulting in a spread-out Bragg peak (SOBP) which covers the volume of the tumor. In this way, the dose peak–to–plateau ratio decreases and the treatment loose some of its advantage compared to the photons. However, there is also an advantage in the direction lateral to the direction of the beam where much more spread is encountered with photons.

We investigate the change in the OSL response when identical doses are given to the Al_2O_3:C dosimeter with either γ-rays or protons at different energies, i.e. different ionization density, and focus on the important issue of change in OSL with linear energy transfer (LET). The use of Al_2O_3:C in hadron dosimetry is also currently being investigated for monitoring the dose delivered to astronauts in space [97] and to estimate the dose rate at the surface of Mars to date sediments [48].

1.3.4 Model explanations

Several models have been developed over the years to explain the dose-response of luminescence materials with special focus on the linear/supralinear/sublinear behaviour of this response (see figure 1.3) [42]. To explore and understand the physical processes that cause the change in OSL response, we interpret and analyze the temperature and energy results using two models - one based on band structure theory and the other based on radiological concepts named track structure theory (TST). The band structure model and the TST model are largely two complimentary models that deals with separate phenomena of solid state dosimeters [42].

Band structure modeling is based on the conduction band/valence band models' kinetic theory of the transport of charge carriers. The ideas is fairly straight forward: supralinearity arises from the decreased efficiency of the competitive processes relative to the luminescence processes. This model ignores the effects of ionization density but can reproduce the shape of both TL glow curves and OSL decay curves [22, 59] and we use this model to correlate temperature-dependent changes in the OSL signal with physical mechanisms in the crystal.

TST, first introduced by Katz in the late 1960s, is a radiological model which is mainly based on statistical (cumulative Poisson distribution) single/multiple hit interaction of the dose deposition mechanism [23, 52, 51]. Again, the idea is simple and intuitively appealing: sensitive sites or targets susceptible to single-hits lead to linear behavior whereas multiple hits lead to a supralinear dose-response. The model has successfully described and predicted the response of HCPs for many different dosimeters and biological systems. The HCP-response of a dosimeter is predicted by folding the γ-response of the dosimeter with a dose distribution around the track of the HCP. We use TST to investigate the effect of energetic protons on the OSL response from Al_2O_3:C.

Another model of interest is the unified interaction model (UNIM). In UNIM, the dosimeter response arises from a mixture of localized and delocalized recombination mechanisms. At low doses, the distance between trap centers and luminescence centers is large and delocalized recombination which is subject to competition is dominating. At larger doses, this distance decreases and localized recombination which is not subject to competition is now also possible. This can explain the supralinear dose response [41]. Although this model was not directly applied on data in this thesis, it provides a framework for physical interpretation on which the extracted parameters from TST can be based.

1.3.5 Thesis structure

In chapter 2, the band structure and track structure models are described along with some fundamental quantities and units for ionizing radiation which play a key role in radiation dosimetry. Chapter 3 describes the detector systems, crystals and fiber cables used in the different experiments. Chapter 4 presents the experiments and results of the temperature study which deals with the changes in RL and OSL response when the stimulation and irradiation temperature of the Al_2O_3:C crystal is varied in the room to body temperature region (20–40°C). These results are compared with band structure model simulations and on the basis of this comparison two possible mechanisms are suggested to cause the temperature changes. Chapter 5 presents the results of the change in OSL response to protons of different energies (ionization densities). Here, the key quantity of interest is how much luminescence is produced per dose unit when irradiating with protons of different energy compared to gamma irradiation. The TST model is fitted to data and we interpret the data in terms of the extracted parameters from these fits in the framework of UNIM. Chapter 6 collects and summarizes the experimental and theoretical results from the two preceding chapters. Finally, we ask the question whether an optimal OSL protocol, i.e. a protocol which is independent of temperature and energy effects, is possible and what aspects that could be considered in order to create such a protocol.

During the PhD study, the following articles have been produced:

1. **J.M. Edmund**; C.E. Andersen; C.J. Marckmann; M.C. Aznar; M.S. Akselrod; L. Bøtter-Jensen, CW-OSL measurement protocols using optical fibre Al_2O_3:C dosemeters, Radiation Protection Dosimetry, 2006 119: 368-374.

2. **J.M. Edmund**; C.E. Andersen; Temperature dependence of the Al_2O_3:C response in medical luminescence dosimetry, Radiation Measurements, 2007 42: 177-189.

3. **J.M. Edmund**; C.E. Andersen; S. Greilich; G.O. Sawakuchi; E.G. Yukihara; M. Jain; W. Hajdas; S. Mattsson, Optically stimulated luminescence from Al_2O_3:C irradiated with 10-60 MeV protons, Nucl. Instrum. Meths A, 2007 580: 210-213.

4. **J.M. Edmund**; C.E. Andersen; S. Greilich, A track structure model of optically stimulated luminescence from Al_2O_3:C irradiated with 10-60 MeV protons, Nucl. Instrum. Meths B, 2007 262: 261-275.

5. C.E. Andersen; **J.M. Edmund**; M. Jain; E. Grusell; J. Medin; S. Mattsson, Medical proton dosimetry using radioluminescence from aluminium oxide crystals attached to optical fiber cables, Nucl. Instrum. Meths A, 2007 580: 466-468.

6. M. Jain; C.E. Andersen; W. Hajdas; **J.M. Edmund**; L. Bøtter-Jensen, Luminescence response to proton irradiation in some natural dosemeters: Implications for martian sediment dating, Nucl. Instrum. Meths A, 2007 580: 652-655.

Articles 2 and 4 contain the results on which the majority of this thesis is based. Furthermore, the following abstracts have been submitted to the 15th Solid State Dosimetry Conference and is expected to appear in a special conference proceedings issue of Radiation Measurements by the end of 2007:

1. S. Greilich; **J.M. Edmund**; M. Jain; C.E. Andersen, A coupled RL and transport model for mixed-field proton irradiation of Al_2O_3:C.

2. C.E. Andersen; **J.M. Edmund**; S.M.S. Damkjær; S. Greilich, Temperature coefficients for in vivo RL and OSL dosimetry using Al_2O_3:C.

2 Theory

This chapter introduces and describes the band structure and track structure models which are used to make statements about the underlying physical mechanisms that influence the OSL response. The band structure model includes the delocalised conduction and valence bands which are separated by a forbidden energy band gap in which localized energy defect states can be found. The OSL response can then be described by the kinetics of charge carriers migration between these localized and delocalised states. The theory is first described in general and then specifically for Al_2O_3:C. The last part of the chapter presents the track structure theory which describes the effects of ionization density on the OSL response. Here, the sublinear and supralinear dose-response of the dosimeter is ascribed to the activation of one- and two-hit targets. The increase or decrease in the OSL response to proton irradiation can then be explained by folding the OSL γ-response of the dosimeter with the track structure of the proton. The track structure theory contains a distinction between so-called ion- and gamma-kills which is explained in detail at the end of the chapter. First, however, we will start by introducing some basic radiation quantities which are useful for ionizing radiation research in general and for this study in particular.

2.1 Radiation quantities

When a beam of photons (X- or γ-rays), electrons, neutrons, protons or other HCPs, interact with molecules or atoms of a target material, we use interaction coefficients to describe the likelihood for a specific type of interaction to occur. The interaction depends on the energy and type of the radiation and the target material.

2.1.1 Cross-section

The fundamental interaction coefficient is the cross-section, σ, and we define the cross-section for a specific event as the quotient of P by ϕ where P is the probability for the event to occur per target of a material and ϕ is the fluence of the incident radiation [45] on that material, i.e.

$$\sigma = \frac{P \text{ (probability for a given event per target material)}}{\phi \text{ (number of particles per unit area)}} \tag{2.1}$$

The term "event" is considered very general. For example, it could be the deflection of a particle in a given angular direction or the loss of a certain amount of energy or both. The classical interpretation of cross-section is that it is the area an incident particle must hit in order for the event to occur.

The differential cross-section, $d\sigma$, describes events that occur in an interval. If the cross-section describes the deflection in an angle θ or the loss of energy E, the differential cross-section $d\sigma/d\theta$ describes the deflection in the interval $[\theta,\theta + d\theta]$ and $d\sigma/dE$ describes the loss of energy in the interval $[E,E + dE]$.

To describe the luminescence processes in a crystal, we introduce the photoionization cross-section, σ_{ion}, the capture cross-section, σ_{cap}, and the recombination cross-section, σ_{rec}. σ_{ion} describes how hard it is to ionize a charge carrier (a hole or electron) from a given trap defect in the crystal by the absorption of a photon from a stimulation light source - typically a laser or light emitting diodes (LEDs). σ_{cap} describes the ability for a given defect in the crystal to capture or trap a charge carrier and σ_{rec} describes a defects ability to capture charges of opposite sign resulting in recombination. In TST, the cross-section for emitting electrons along the trajectory of a HCP is essential for the basic deviation of the radial dose distribution.

2.1.2 Linear energy transfer (LET)

For charged particle like electrons, protons and other HCPs, the mass-stopping-power is used to describe the loss of energy when traversing a target material. The mass-stopping-power is defined as

$$\frac{S}{\rho} = \frac{1}{\rho}\frac{dE}{dl} \tag{2.2}$$

where $S = dE/dl$ is the linear stopping-power and ρ is the density of the target material. dE is the energy lost by the charged particle when traversing a distance dl. The mass-stopping-power is the sum of the electronic (or collision), radiative and nuclear mass-stopping-power but since the latter two

are negligible for the energies investigated here, we will refer to the electronic mass-stopping-power as the mass-stopping power. The linear energy transfer, L_Δ, can then be written as

$$L_\Delta = S - \frac{dE_\Delta}{dl} \tag{2.3}$$

where dE_Δ is the sum of kinetic energies greater than Δ of all electrons released by the charged particle traversing a distance dl [45]. It describes how much energy is deposited in the material from the irradiating beam by ionized electrons with kinetic energy less than Δ. Here, we will refer to the unrestricted linear energy transfer, L_∞, which is equal to the linear stopping-power, such that we have $LET = L_\infty/\rho = S/\rho$ throughout the thesis. We have conveniently chosen the unit of LET to be either $\mathrm{MeVcm^2g^{-1}}$ or keV/μm.

2.1.3 Absorbed dose

The absorbed dose is defined as

$$D = \frac{d\overline{\epsilon}}{dm} \tag{2.4}$$

where $d\overline{\epsilon}$ is the mean energy imparted to the matter of mass dm [45]. The imparted energy ϵ is a stochastic quantity and subject to statistical fluctuations. Although the absorbed dose is defined in a point, it is the expectation value (or average) of imparted energy which makes it a non-stochastic quantity. The unit for the absorbed dose is J/kg and it has the special name gray (Gy)[1].

2.1.4 Ionization density

As will be described in detail later, low- and high-LET particles, like γ-rays and protons respectively, deposit energy in a material very differently although they may, on average, deliver the same absorbed dose to the material. The ionization density describes how many electron-hole pairs, N_{eh}, are created in a volume, dV, that absorbs the energy dE. Basically, high-LET particles deposit the same energy as low-LET particles over a much smaller volume and therefore the ionization density is much higher for high-LET particles compared to low-LET particles.

[1] Although the term "dose" does not have a unique definition, it is here implicitly taken to be the absorbed dose whenever encountered in text.

2.2 Band structure theory

The transformation of energy levels in atoms to energy bands in crystals is based on a periodic potential formalism. One can then describe the transport of charge between different energy states by introducing kinetic rate equations.

2.2.1 Periodic potential

In a crystalline solid, the molecules are arranged in a regular pattern called a crystal lattice which can be broken down into multiple repetitions of a single cell which is specific for the given type of lattice. The electrons of the solid therefore experience a periodic potential and the Hamiltonian, $\hat{H}$, is given as

$$\hat{H} = \frac{\hat{p}}{2m} + V(x) \tag{2.5a}$$

$$V(x) = V(x+d) \tag{2.5b}$$

where $\hat{p}$ is the kinetic energy operator, m is the mass of an electron, V is the potential and d is the period length or lattice constant. For simplicity, we have chosen the one-dimensional case but the argumentation applies for three dimensions as well. Bloch's theorem states that the eigenfunctions of a periodic Hamiltonian is given by the product form

$$\varphi(x) = e^{ikx}u(x) \tag{2.6a}$$

$$u(x) = u(x+d) \tag{2.6b}$$

where k is the wavenumber and $u(x)$ is a periodic function with the period of the potential. For a free electron the relation between k and energy E is $E = \hbar^2 k^2/2m$ where m is the mass of an electron and $\hbar$ is Planck's constant divided by 2π. From eq. (2.6), we see that $\varphi(x+d) = e^{ikd}\varphi(x)$. If a lattice consists of N molecules, we have that $\varphi(x+Nd) = \varphi(x)$ is true if

$$e^{ikNd} = 1, \quad kNd = 2n\pi \quad (n = 0, \pm 1, \pm 2, \ldots) \tag{2.7}$$

This implies that the allowed electron-states (k-values) are given in the form of a discrete spectrum ($k_n = n(2\pi/Nd)$). We know from the Pauli exclusion principle that no two electrons can occupy the same state so the values of k also reflects the spectra of energies since n is the principal quantum number. If N is very large the difference between each allowed value of k (energy) is small and the spectrum may be taken to comprise a continuum [56, 67] (see fig. 2.1A).

We can use the so-called Kronig-Penny model to describe the potential of the crystal lattice and this leads to a dispersion relation for the wave number k [56]. From this, sections of allowed and forbidden intervals of k are created and since the density of states in these intervals is given by the number of molecules in the lattice, we arrive at an energy structure of a crystal solid which consists of allowed and forbidden energy bands. The forbidden bands are usually referred to as "energy gaps" and the next highest and highest allowed energy band are referred to as the "valence band" and "conduction band", respectively. The energy band structure is outlined in figures 2.1B and C.

2.2.2 Isolators, semiconductors and conductors

The Fermi energy, E_f, is defined as the energy of the topmost filled energy level of an electron system in its ground state (at 0 kelvin) and is a consequence of Pauli's exclusion principle for fermions. At absolute zero temperature, the energy levels below E_f are completely full whereas the levels above E_f are completely empty. When the Fermi energy is placed within the valence band, the band is only partially filled and valence electrons can easily move to higher energetic states and thereby conduct electricity when an electric field is applied. This type of solid is referred to as conductors or metals. When the Fermi energy lies in the band gap, electrons can not move easily because all allowed states are already filled with electrons. In order for the electrons to move, they have to gain enough energy to cross the band gap and occupy the lower energy levels of the conduction bands. When the energy gap is relative small, we refer to the solid as a semi-conductor and when it is large we call the solid an isolator. The situation is depicted in figure 2.2.

The crystal described so far is a perfect one and for this situation figures 2.1 and 2.2 appropriately describe the energy structure of the electrons in the crystal. When an electron is ionized from the valence band into the conduction band, it not only occupies a state there but also leaves behind an unoccupied state in the valence band. This absence of an electron is termed a "hole" and can be considered as a particle with opposite charge.

In reality there is no such thing as a perfect crystal since all materials have a natural contamination of impurities that breaks down the periodicity of the potential in eq. (2.5) and consequently electrons can occupy energy levels in the band gap that otherwise would be forbidden in the perfect crystal structure. The energy levels of defects can be illustrated by considering an Y^+X^- alkali halide crystal. If the crystal lattice contains a vacant anion site (missing an X^- ion), an electron from the conduction band may be captured

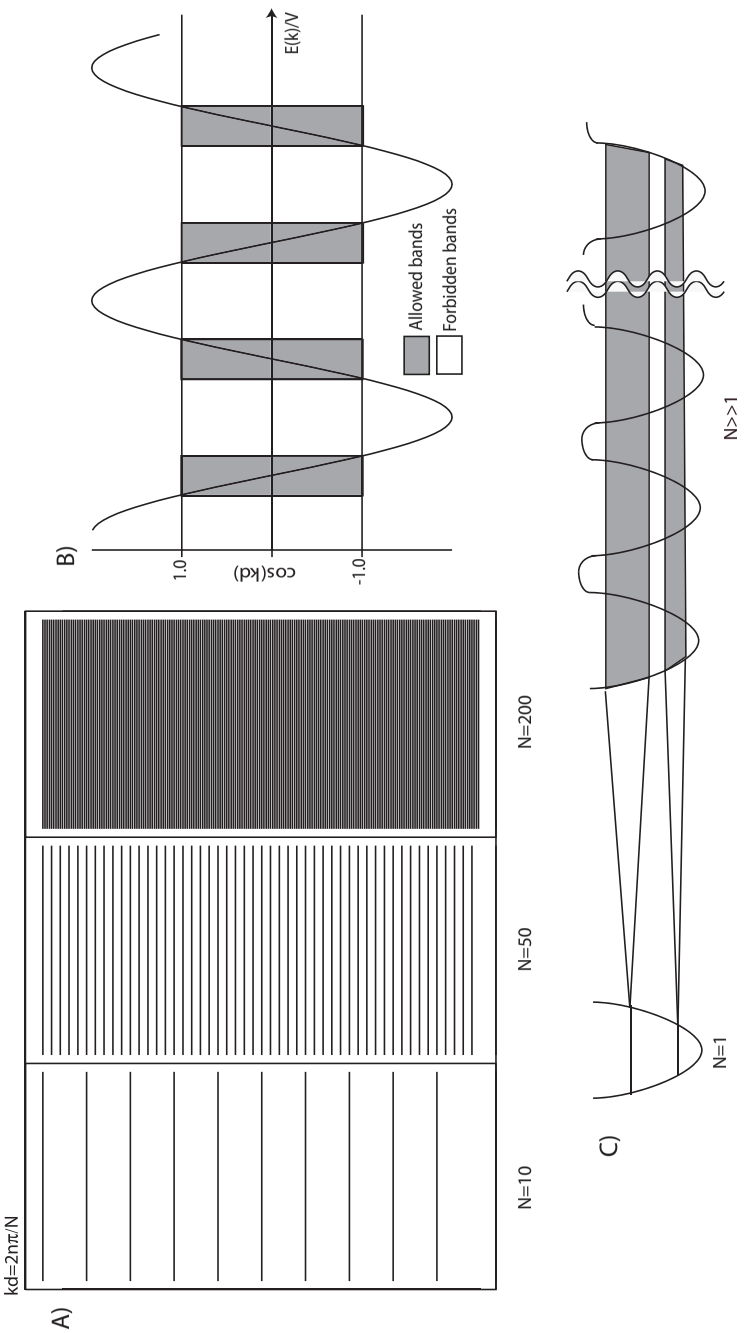

Figure 2.1: A) The density of energy levels increase with the number of atoms or molecules in a crystal. B) A qualitative sketch of the outcome of the dispersion relation for the wavevector k. The energy bands from A) are divided into forbidden and allowed intervals. C) The transition from energy levels in an atom to energy bands in a crystal.

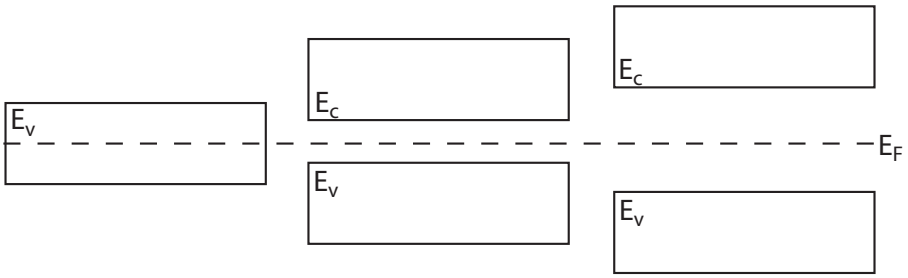

Figure 2.2: The principe of energy levels in a conductor (left), a semi-conductor (middle) and an isolator (right). E_f is the Fermi energy, E_c is the minimum energy level in the conduction band and E_v is the maximum energy level in the valence band. The distinction between an isolator and a semiconductor is that semiconductors can have electrons in the conduction band at room temperature whereas this is not the case for isolators. Diamond has an energy gap of about 7 eV and is thus an isolator whereas silicon has a band gap of about 1 eV and is a semiconductor [67].

here and does no longer contribute to conductivity. The energy required to realize the electron from the site is less than the energy required to free a valence electron from an X^- ion. The anion vacancy (the defect) therefore has an energy level which lies in the energy gap between the valence and conduction band. This kind of defect acts as an electron trap and the energy level is located just below the minimum energy level of the conduction band (E_c in fig. 2.3A). Similar, a cation vacancy (missing a Y^+ ion) can create an excess amount of negative charge and thus it requires less energy to free valence electrons from this site. This defect acts a hole trap because little energy is required to remove the electron which leaves behind a hole. The hole trap posseses an energy level in the forbidden band gap just above the maximum energy of the valence band (E_v in fig. 2.3A) [59].

The valence and conduction band ideally extend throughout the crystal without any deformation which means that the wave functions of the electrons and holes in the delocalised bands have an equal probability of being everywhere in the crystal. The energy levels associated with the defect are centered upon these and are localized. If large clusters of defects exist or the edge of the crystal is reached, however, the valence and conduction band can be severely distorted and the width of the forbidden band gap can either widen or narrow around local defects [59]. The situation is shown in figure 2.3B.

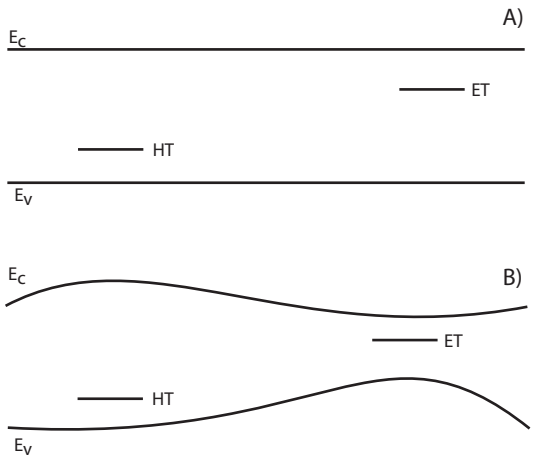

Figure 2.3: A) The energy level of an electron trap (ET) and hole trap (HT) located just below the minimum energy level E_c of the conduction band and above the maximum energy level E_v of the of the valence band. The conduction and valence band are perfectly delocalized. B) A more realistic picture of a crystal energy structure. The energy band gap shows local variations depending on local defect concentrations.

2.2.3 Transitions

In order to understand the luminescence phenomenon of crystalline solids, we need to examine the different possible transitions between localized defects and delocalized energy bands for holes and electrons which are shown in figure 2.4. Transition (1) is the process of ionization and is the result of

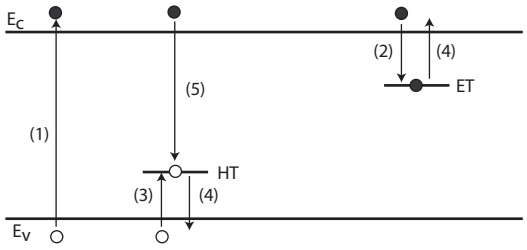

Figure 2.4: The different kinetic transitions of charge carriers in a crystal. (1) Ionization and creation of electron-hole pairs. (2) Capturing of electrons by an electron trap (ET). (3) Capturing of a hole by a hole trap (HT). (4) Release of electrons or holes by stimulation of either heat or light. (5) Recombination of delocalized electrons with localized holes. This can lead to the production of luminescence.

the absorption of energy from radiation. This creates electron-hole pairs

which migrate throughout the crystal until they become localized at defect centers. The localization leads to trapped electrons (2) or holes (3) and is a consequence of the defects ability of capturing charge which is described by the traps capturing cross-section σ_{cap} (see section 2.1.1). The captured electrons and holes may be released from their traps by stimulating with either heat or light (4). The release of charge by heat is described by the product of a trap–specific frequency factor s given in s^{-1} and the Boltzmann factor, $\exp(-E_t/kT)$, where E_t is the energy depth of the trap, k is the Boltzmann constant and T is the stimulation temperature in kelvin. At room temperature, the thermal energy, kT_{room}, is equal to 0.025 eV. The release of charge by light is described by the photoionization cross-section σ_{ion} of the trap and the flux of the stimulating light. In addition to being trapped, free electrons and holes may also annihilate with a charge carrier of opposite sign through recombination. Although local and direct recombination exist, we will here only consider recombination of free electrons with captured holes (5) since this is the dominating process in Al_2O_3:C. Thus, a recombination center is a hole trap that possess the ability to capture electrons. If the emission of light is accompanying the recombination, we have the production of luminescence and the recombination center is then also referred to as a luminescence center.

The quantities associated with the different transitions in figure 2.4 are

$$R = \xi \cdot \Gamma \qquad \text{irradiation (1)} \qquad (2.8a)$$

$$A_n = \sigma^e_{cap} \cdot \nu^e_{con} \qquad \text{electron-trapping (2)} \qquad (2.8b)$$

$$A_m = \sigma^h_{cap} \cdot \nu^h_{val} \qquad \text{hole-trapping (3)} \qquad (2.8c)$$

$$f = \sigma_{ion} \cdot \Phi \qquad \text{stimulation (4)} \qquad (2.8d)$$

$$A_{mn} = \sigma^h_{rec} \cdot \nu^e_{con} \qquad \text{recombination (5)} \qquad (2.8e)$$

R is the creation rate of electron-hole pairs in s^{-1}, ξ is the number of electron-hole pairs per unit dose in Gy^{-1} and Γ is the dose-rate of the incident radiation in Gy/s. A_n, A_m and A_{mn} is the trapping and recombination probability density rate of the electron and hole traps and recombination centers given in cm^3/s. The capturing and recombination cross-section, σ_{cap} and σ_{rec}, for electrons (e) and holes (h), respectively, are in cm^2. ν^e_{con} is the mean velocity of electrons in the conduction band and ν^h_{val} is the mean velocity of holes in the valence band in cm/s. Finally, f is the stimulation probability rate in s^{-1}, Φ is the photon flux in $cm^{-2}s^{-1}$ and σ_{ion} is the photoionization cross-section in cm^2 [59, 22, 98].

2.3 Model for Al_2O_3:C

A generalized model describing the OSL signal from isolating materials has been proposed and is shown in figure 2.5 [65, 62, 60, 22]. It includes three electron traps of different energy depths and two types of hole traps. It has been established that Al_2O_3:C includes all of these components [96, 99]. In general, the TL and OSL properties of Al_2O_3:C crystals are seen to greatly depend on the growth method used to produce them [3] and variations in the luminescence properties of one crystal to another are quite common. Still, the model provides a qualitatively good description of the physics in Al_2O_3:C.

2.3.1 Electron traps

Each trap represents a distribution of energy depths around a mean value [8, 63, 71]. Two shallow traps are identified in Al_2O_3:C, one at -13 °C and another at 37 °C but only the latter has relevance at room and body temperatures. The main dosimetry trap is reported extensively throughout the literature [8, 63, 7, 22]. It is centered around 180°C and is believed to be the main charge contributer associated with the broad absorption band centered at 480 nm. The energy depth is a distribution centered around 1.5 eV. Although the nature of crystal defects causing this trap is unknown, experimental evidence using UV light indicates that it is an electron trap. Deep traps are located in the temperature region 700–1000°C and have an energy depth in the order of 3 eV or higher [99, 2, 93, 58].

2.3.2 Recombination centers

Recombination centers are basically deep (stable) hole traps which contain a trapping cross-section for electrons. When electrons recombine with holes this may or may not result in luminescence emission. The recombination centers in Al_2O_3:C are mainly created by oxygen (anion) vacancies called F^+ and F centers with either one or two captured electrons, respectively. Al_2O_3:C has a high initial concentration of F and F^+ centers as a result of sample production and has a much higher sensitivity than natural Al_2O_3. The basic luminescence process is believed to be the recombination of one electron with an F^+ center. This creates an excited F center which decays to its ground state by emitting a photon with a wavelength at 420 nm. The recombination process is usually summarized in the reaction scheme

$$F^+ + e^- \rightarrow F^* \rightarrow F + h\nu_{420nm} \tag{2.9}$$

The relaxation of the excited F-center to its ground state is a forbidden triplet–to-singlet transition and so has a long lifetime τ of about 35 ms [55]. As described in the introduction, one can exploit this feature to separate the short–lived florescence signal of the fiber cable from the RL signal of Al_2O_3:C if the radiation source is pulsed.

During irradiation, holes are trapped at F centers resulting in the production of F^+ centers. Like F centers, F^+ centers can relax to their ground state by emitting a photon according to the scheme

$$F + h^+ \rightarrow F^{+*} \rightarrow F^+ + h\nu_{325nm} \tag{2.10}$$

Therefore, there exists an equilibrium between F and F^+ centers that is shifted towards one or the other depending on the presence of electron and hole traps. The main recombination process on which this study focuses, namely the F center emission, suggests that the shallow, main and deep traps mentioned above are indeed electron traps. This hypothesis have been supported experimentally by considering the shift in equilibrium between F and F^+ centers. A deep hole trap has been identified in the region 500–600°C by similar arguments to the above. Although holes trapped here are also able to recombine with electrons, the recombination does not result in luminescence and is therefore not detected. This trap is suggested to cause a sensitivity decrease after the luminescence response has saturated and could be due to a high concentration and/or low capturing cross–section [73, 99, 96, 76].

2.3.3 Population rate equations

The transition between the different energy levels during irradiation and optical stimulation can be described by a set of non-linear, coupled rate equations using the quantities introduced in equations (2.8a-e). The rate equations describing the model in figure 2.5 are purely empirical and all first order kinetics, i.e. the rate of change in population is proportional to the population itself only to the first power. Although each trap represents a distribution of energy depths, we will here consider the traps as discrete energy levels representing an average of the different energy distributions.

For the electron traps, we have

$$\frac{dn_i}{dt} = n_c(N_i - n_i)A_i - n_i s_i \exp(-E_i/kT) - f_i n_i \tag{2.11}$$

for $i = 1, 2, 3$ where 1=shallow, 2=main and 3=deep. In a similar fashion, we can write for the hole traps

$$\frac{dm_j}{dt} = n_v(M_j - m_j)A_j - n_c m_j A_{mj} \tag{2.12}$$

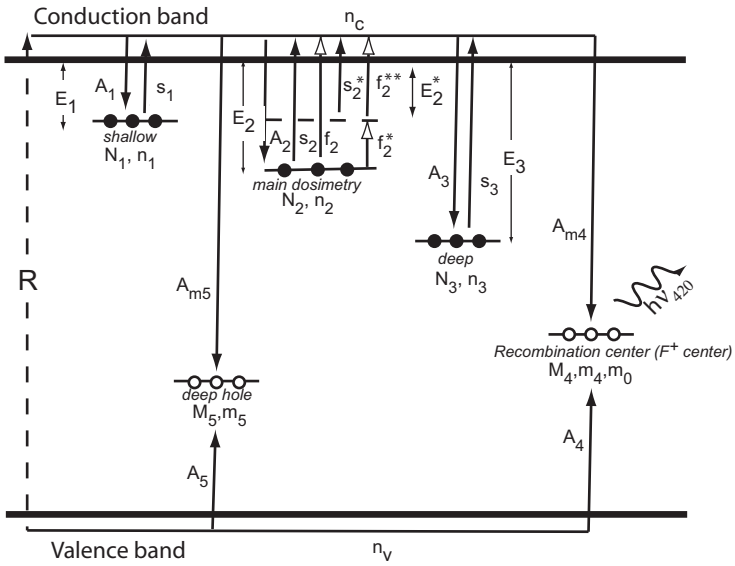

Figure 2.5: Energy band model describing charge transitions through the delocalized bands in Al_2O_3:C. Parameters are placed next to the process they describe. Subscripts: 1=shallow traps, 2=main dosimetry trap, 3=deep trap, 4=radiative hole trap, 5=non-radiative hole trap, and asterix=thermal excitation parameters. Optical transitions are indicated by open upwards arrows, whereas passive trapping and thermal assistance is indicated with closed arrows. Filled circles=electrons and open circles=holes. See also text for details.

for $j = 4, 5$ where 4=radiative hole trap and 5= non–radiative hole trap. For the rate change in the delocalized populations, we have

$$\frac{dn_c}{dt} = R - \sum_i \frac{dn_i}{dt} - n_c \sum_j m_j A_{mj} \tag{2.13}$$

for the conduction band and

$$\frac{dn_v}{dt} = R - n_v \sum_j (M_j - m_j) A_j \tag{2.14}$$

for the valence band. The luminescence is at all times given by

$$L = n_c m_4 A_{m4} \tag{2.15}$$

In the equations, n_i is the concentration of electrons in the ith trap and m_j is the concentration of holes in the jth trap. n_c is the concentration of free (delocalized) electrons and n_v is the concentration of free holes. N_i is the concentration of available electron traps of type i and M_j is the concentration

of available hole traps of type j. A_i is the electron trapping probability of trap i and A_j is the hole trapping probability of trap j. A_{jm} is the recombination probability of the jth trap. An initial population $M_4 = m_0$ of radiative recombination centers, i.e. F^+ centers, are present before irradiation begins and charge neutrality is kept by impurities with opposite charge elsewhere in the crystal. s_i is the frequency factor of the ith electron trap and f_i is the stimulation rate of the ith electron trap during OSL. Only the main dosimetry trap is considered optically active here so $f_1 = f_3 = 0$. R is the irradiation rate, i.e. the electron-hole pair production rate.

2.3.4 OSL decay components

Let us consider a model with only one optical electron trap and one recombination center. During the optical stimulation phase, only electrons are released, i.e. hole traps are assumed to have $\sigma_{ion} = 0$, and we can write a charge neutrality condition as

$$\frac{dn_c}{dt} = \frac{dm}{dt} - \frac{dn}{dt} \tag{2.16}$$

With the so-called "quasi-equilibrium approximation", we have that $dn_c/dt \ll dn/dt$ and $dn_c/dt \ll dm/dt$ and we get

$$\frac{dm}{dt} = \frac{dn}{dt} \tag{2.17}$$

If we neglect re-trapping and thermal excitation, i.e. $n_c(N-n)A_n \ll n_c m A_m$ and $E_t \gg kT$, we can express the luminescence L as

$$L = n_c m A_m = -\frac{dm}{dt} = -\frac{dn}{dt} = fn \tag{2.18}$$

From this, the luminescence can be described with a simple exponential decay form as

$$L(t) = fn(t) = fn_0 e^{-ft} = L_0 e^{-ft} \tag{2.19}$$

where L_0 is the initial OSL intensity and $f = \sigma_{ion}\Phi$. Eq. (2.19) represents the basic (first order) OSL decay curve. In this ideal case, it is clear that the luminescence is directly proportional to the concentration of trapped electrons, n_0, which in turn is proportional to the absorbed dose.

Trap distribution

We mentioned in section 2.3.1 that the main dosimetry trap in reality is a distribution of energy levels centered around an energy depth of 1.5 eV. We

can model this distribution using eq. (2.19) by assuming that the OSL signal is composed of a distribution of optically active traps (the energy spectrum of the main dosimetry trap including both shallow, medium and deep excitation energies) and one recombination centre (the F^+–center). Further, if the traps do not interact, by the superposition principle the OSL output signal, $L(t)$, can be represented as

$$L(t) = \sum_{j=1}^{M} n_{0j}\tau_j e^{-\tau_j t} \tag{2.20}$$

where t is the stimulation time, n_{0j} is the initial number of trapped electrons in the jth optically active trap and $\tau_j = f_j = \Phi\sigma_{ion,j}$ is the OSL decay constant of the jth trap [71].

Regularization

We can apply eq. (2.20) to the OSL curve in figure 2.6A. A spectrum of M decay constants were chosen prior to the fitting procedure. In this way, eq. (2.20) becomes linear and appears as

$$\mathbf{L} = \mathbf{A}\mathbf{n} \tag{2.21}$$

where $\mathbf{L} = L(t_i)$ $(i = 1, \ldots, N_{data})$, $\mathbf{n} = n_{0j}$ $(j = 1, \ldots, M)$ and $\mathbf{A} = \{\tau_j \exp(-\tau_j t_i)\}$. Eq. (2.21) represents the discrete case of a Fredholm integral equation of first kind and is ill-posed [36]. In order to find a useful and stable solution, a regularization constraint must be introduced. Here, the Tikhonov regularization is used to obtain a regularized solution, $\mathbf{n}_\lambda$, as the minimum of the weighted sum of the residual norm and a side constraint

$$\mathbf{n}_\lambda = min\big(\|\mathbf{A}\mathbf{n} - \mathbf{L}\|^2 + \lambda\|\boldsymbol{D}\mathbf{n}\|^2\big) \tag{2.22}$$

where λ is a regularization parameter and $\boldsymbol{D}$ is the discrete approximation to the 2nd derivative operator [37]. Since the stimulation intensity Φ is constant, the choice of decay constants in reality reflects the photoionization cross-sections σ_{ion}. If σ_{ion} of a trap is small, one reasonable interpretation is that the optical energy depth of the trap is deep. The part of $\mathbf{n}_\lambda$ that represents small decay constants is then associated with deep trap depths while the larger decay constants are associated with the medium and shallow trap depths [96]. Figure 2.6B shows the optical energy spectrum using this method. The method provides an indication of the width of the optical trap distribution and was fitted to two Gaussian functions. This procedure has previously been used to establish threshold energy distributions [93, 1, 8].

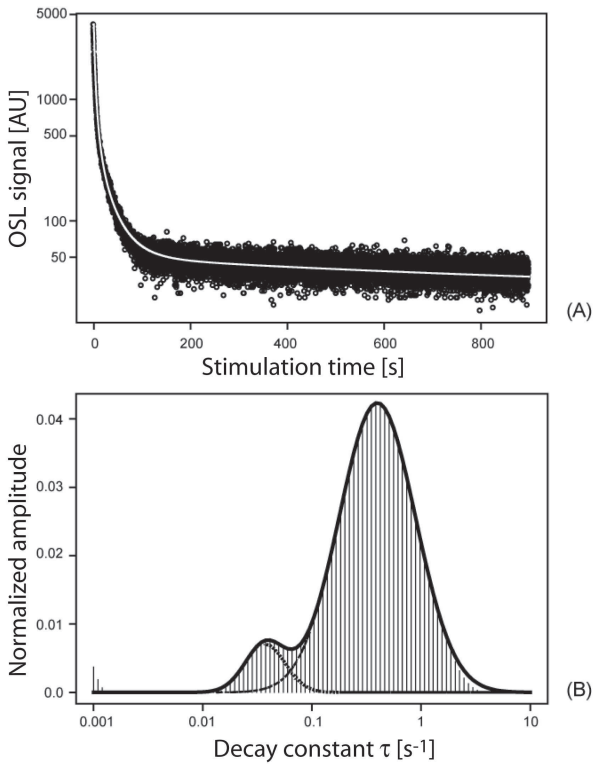

Figure 2.6: **A**: An OSL decay curve (black circles) and a fitted curve (white line) from Al_2O_3:C using Tikhonov regularization. **B**: Corresponding spectrum of optical threshold values covering 4 decades. Small decay constants correspond to large optical threshold energies and vice versa. The lines indicate two individual Gaussian curves and their sum.

2.3.5 Luminescence output (efficiency)

The band structure model does not provide the absolute intensity of the luminescence since its description is phenomenological and does not include specific material characteristics like chemistry or crystal structure. As noted on page 4, the TL and OSL luminescence output efficiencies are between 0.01 and 1% and are here defined as the ratio of the energy emitted as light, E_{emit}, to the energy absorbed by ionizing radiation, E_{abs}. The output efficiency, ϱ, can be quantified by terms describing the different steps involved in the luminescence process as

$$\varrho = \frac{E_{emit}}{E_{abs}} = \frac{h\nu N_{eh}}{E_{abs}} \eta_{trp} pSQ\eta_{esc} \tag{2.23}$$

$h\nu$ is the average energy of the emitted photons and N_{eh} is the number of electron-hole pairs produced by energy deposited by the ionizing radiation.

η_{trp} is the fraction of charge carriers captured by traps during irradiation. p is the probability of releasing the charge carriers from the traps during stimulation and S is the efficiency by which the charge carriers are transported to a luminescence center. Here, the excited luminescence center will de-excite under the emission of a photon with quantum efficiency Q. The fraction of photons that will then escape the crystal without being absorbed (optical self-absorption) is given by η_{esc}. N_{eh} depends on the energy required to create an electron-hole pair, E_{eh}, which is related to the forbidden band gap width, E_g, as $E_{eh} = \beta E_g$ where β is a number between 1 and 4 [20]. We can then write N_{eh} as [70]:

$$N_{eh} = \frac{E_{abs}}{E_{eh}} = \frac{E_{abs}}{\beta E_g} \tag{2.24}$$

If we insert eq. (2.24) into eq. (2.23), the efficiency can be written as

$$\varrho = \frac{h\nu}{\beta E_g} \eta_{trp} p S Q \eta_{esc} \tag{2.25}$$

From this equation, we can set a theoretical upper limit for the luminescence output efficiency if we assume that all created electron-hole pairs are trapped during irradiation ($\eta_{trp} = 1$) and released during stimulation ($p = 1$) with a 100 % efficiency of reaching the luminescence center ($S = 1$) and de-excite under the emission of photons ($Q = 1$) which are not absorbed ($\eta_{esc} = 1$). The maximum luminescence efficiency is then

$$\varrho_{max} = \frac{h\nu}{\beta E_g} \tag{2.26}$$

For Al_2O_3:C, $\beta = 2.7$ and $h\nu = 2.95$ eV and with a band gap about 8.7 eV, η_{max} is estimated to be around 13 % [20].

Until now, we have only characterized the ionizing radiation through the rate, R, by which it produces electron-hole pairs but not how the ionizing radiation deposits its energy in the crystal. This is because the ionization density is considered constant throughout the crystal when describing the physics with the rate equations of the band structure model. The ionization density is not uniform when considering radiation with protons and a distinction between low- and high-LET radiation is necessary. The track structure theory incorporates the ionization density into the response of the dosimeter and this model is the subject of the following sections.

2.4 Target theory

We can think of a dosimeter to consist of identical radio-sensitive volumes which are referred to as sensitive sites or targets. A widespread practice is then to connect the dose deposited in these targets by radiation to the observable effect of the dosimeter [52, 35, 84]. A typical example is photographic grains embedded in a matrix of passive material.

When energy is deposited in a target it has a probability of experiencing a "hit" and initiate an action leading to the observable effect, e.g. the grain becomes dark. In solid state luminescence dosimeters, the targets could for example be crystal defects that capture free holes and electrons which thereby deposit their energy at the defects. The activation of targets is then taken to be responsible for the observed end effect in the form of luminescence and the energy deposition per mass (absorbed dose) is taken as the hit density [31]. In general, the targets need not to have a direct physical existence but can represent an arbitrary sensitive volume of radius a_0 that needs to be hit in order for an observable effect to take place [52] (see fig. 2.7).

If we consider the targets as identical statistical cells, the probability that one cell is hit x times with an average random number of A hits per cell is given by Poisson statistics as $A^x e^{-A}/x!$. If the average number of hits per

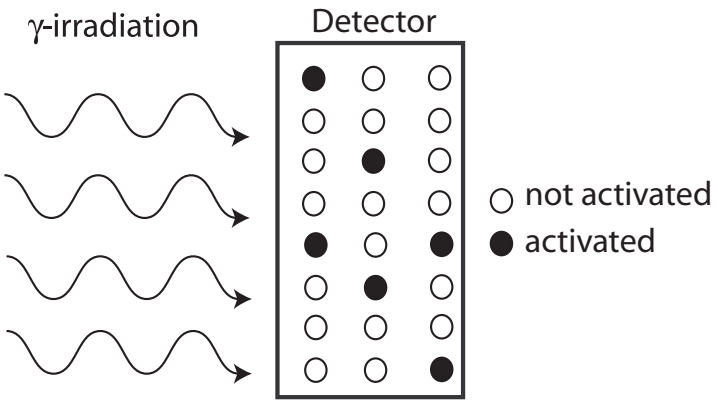

Figure 2.7: The crystal is thought to consist of identical statistical cells (targets) which need c hits to become activated given an average probability of A hits.

target is A and a target needs at least c hits in order to be activated then the probability that a given target will be activated is given by Poisson statistics as

$$P(c, A) = 1 - \sum_{x=0}^{c-1} \frac{A^x e^{-A}}{x!} \tag{2.27}$$

where $A = D/E_c$. D is the dose given to the dosimeter and E_c is a characteristic dose of the dosimeter.

The probability of activating a target given a dose D is taken as the ratio of the dosimeter response, $S(D)$, to the maximum response, S_{max}. For a one-hit dosimeter, i.e. a dosimeter which consists of targets that need at least one hit to be activated, eq. (2.27) becomes

$$\frac{S(D)}{S_{max}} = P_1 = 1 - e^{-D/E_1} \tag{2.28}$$

When $P_1(D)$ has increased to 0.63, $e^{-D/E_1} = e^{-1}$ so at this dose the dosimeter experiences an average of one hit per target leaving 37% of targets not activated and 63% activated by the irradiated dose. At higher doses, D/E_1 represent an average of more than one hit per target and at lower doses the opposite. P_1 is linear at low doses whereafter it becomes sublinear until saturation. The response from a two-hit dosimeter is given by

$$P_2 = 1 - \left(1 + \frac{D}{E_2}\right) e^{-D/E_2} \tag{2.29}$$

where E_2 represent an extrapolation of E_1 [52]. Such a dosimeter displays a sigmoid response and becomes supralinear before saturation.

The γ-response of Al_2O_3:C displays a linear, supralinear and sublinear behavior with dose indicating the presence of both one- and two-hit targets. We can then represent the OSL γ-response (normalized to saturation) as a mixture of these two components

$$\frac{OSL_\gamma(D)}{OSL_\gamma^{max}} = RP_1 + (1 - R)P_2 \tag{2.30}$$

where R is the relative contribution of the one-hit component. A similar behavior from the thermoluminescence (TL) signal of LiF has previously been observed and analyzed [90, 91, 92].

2.5 Track structure theory

The basic mechanisms by which radiation deposits energy in a target material are ionization and excitation of the electrons of the material caused by collisions between the atoms and the incoming radiation [33, 34, 40, 23]. The primary energy transport agents responsible for depositing the collision energy in the dosimeter are delta-rays, here including first, second and

higher order generation electrons[2]. For (β- and) γ-irradiation, the energy is deposited uniformly throughout the dosimeter and can be characterized as a spatially uniform low density sea of initially free electrons and holes. In contrast, protons and other HCPs deposit their energy highly non-uniformly along very localized tracks that are essentially straight lines (and can be approximated by cylinders). The strategy of track structure theory (TST) and other microdosimetric models is to ascribe the difference in dosimeter response of equal doses of γ- and HCP-irradiation to the difference in the spatial distributions of energy deposition, i.e. differences in ionization density.

Katz et al. developed a theory by which the dosimeter response to high-LET irradiation (HCP-irradiation) could be predicted on the basis of a few input parameters and the γ-response of the dosimeter [23, 51, 52]. The principal assumption is that the local efficiency of the dosimeter response taking place in any small volume located in the non-uniformly distribution of dose around the HCPs path is similar to that after irradiation with a uniformly dose distribution of γ-rays. The HCP energy dependence and the γ-ray dose response of a dosimeter is therefore related since saturation of the γ-ray response at high doses then translates to saturation of this response over regions of high dose close to the path of HCPs. A sublinear dose-response to γ-rays will lead to a decrease in the efficiency to HCPs while a supralinear dose-response to γ-rays can lead to an increased efficiency. Therefore, the dosimeter response to HCP-irradiation can be estimated by folding the γ-response, OSL_γ, with a radial dose distribution around the track of a penetrating HCP.

2.5.1 The HCP track

The HPCs trajectory and its immediate vicinity is characterized by a high ionization density of electrons, holes and excitons [40]. At distances further away from the track than the range of the most energetic delta-rays together with other regions of the dosimeter no energy is deposited at all if the flux is low and therefore these areas do not contribute to the dosimeter response. A track is usually approximated as a cylinder which is divided in two regions. The first region is named the "core" and located in the center of the track. Here, the HCP transfer energy to the dosimeter through binary collisions with the material electrons resulting in excitations and production of delta-rays

[2]The radiation induced effects are mainly caused by ionizations and therefore depend on the electrons slowing down spectrum and the dependence of the ionization cross-section on electron energy. These are to a first approximation independent of material and radiation energy [51].

(ionizations). The second region, named the "penumbra", surrounds the core and delta-rays created in the core deposit their energy here (see figure 2.8). Having a uniform dose distribution at low-LET and describing HCP tracks

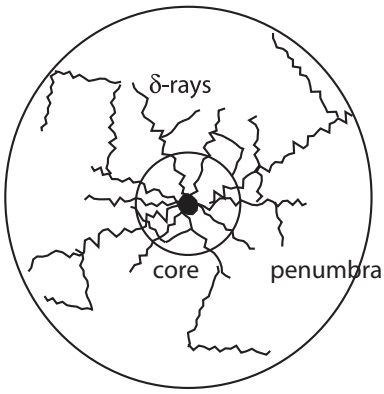

Figure 2.8: A cross-sectional view of a HPC track with the HPC going into the plane of the paper. In the core region, binary collisions and the creation of δ-rays takes place resulting in the deposition of saturation doses. In the penumbra, δ-rays deposit their energy approximately as the inverse square law.

as cylinders with angular and axial symmetries, the difference in the spatial energy deposition can be reduced to a radial dose distribution function $D(r)$.

2.5.2 Radial dose distributions

The original derivation of the dose distribution around an ion track was given assuming a linear energy-range relationship for δ-rays [23]. Later [33, 35, 89], a power-law relation, $r = k \cdot E^{\alpha}$, was used leading to a radial dose-distribution

$$D_{point}(z, \beta, r) = \frac{C}{2\pi} \frac{z^2}{\beta^2 \alpha} \frac{1}{r^2} \left(1 - \frac{r}{R_{max}}\right)^{\alpha^{-1}} \tag{2.31}$$

where $C = 2\pi N e^4 / mc^2$, m and e is the mass and charge of an electron, c is the speed of light and N is the electronic density of the detector. z and β are the effective charge and velocity relative to that of light for the penetrating HCP. r and R_{max} is the radial distance and maximum radial distance from the HCP track, E is the energy of the δ-rays and k and α are constants determined experimentally or by Monte Carlo (MC) simulation. Eq. (2.31) is known as the "point-target" dose distribution because the targets have no physical extension in this distribution (see appendix A.1). Alternatively, we can characterize the size of a target by a radius a_0. Although the volume of the target experiences different doses in the strongly varying field surrounding

the path of the HCP, the target is modeled to respond according to the average dose $\overline{D}(z, \beta, r, a_0)$ delivered to it at a distance r from the track. $\overline{D}(z, \beta, r, a_0)$ is calculated by integrating eq. (2.31) over $2a_0$ a distance r from the track multiplied by a geometry factor [35]. This is known as the "extended target" dose distribution (see appendix A.1.1).

The above distributions are based on the cross-section for ejection of δ-rays along the path of an HCP. Therefore, other types of energy deposition like excitational and vibrational together with the production and subsequent energy deposition of Auger and other low-energy electrons where the ionization potential of the material atoms must be taken into account are neglected. Including the mass-stopping-power[3] of the penetrating HCP in the dose distributions would take these interactions into account as well. Hansen and Olsen proposed such a distribution [33, 35]. The excess energy of the difference between the total and the δ-ray energy deposition is placed in a target positioned in the center of the track [33]. Here, we introduce a simplified version, named D_{Site}, of this distribution as

$$D_{Site}(r) = \begin{cases} (LET - E_\delta)/\pi a_0^2 & \text{for } r \leq a_0, \\ D_{point}(r) & \text{for } a_0 < r \leq R_{max}. \end{cases} \tag{2.32}$$

where $E_\delta = 2\pi \int_{a_0}^{R_{max}} D_{point}(r) r dr$. This is approximatively the same distribution as that introduced by Hansen and Olsen since $D \propto z^2/\beta^2 a_0^2$ is a constant for $r/a_0 < 1$ and $D = D_{point}$ for $r/a_0 > 3a_0$ and therefore the only difference is in the interval $a_0 < r < 3a_0$ [52, 33].

A simplified radial dose distribution was introduced by Scholtz and Kraft in the local effect model (LEM) to predict the relative biological efficiency (RBE) of biological systems [80]. Later, Geiss used this distribution to calculate the relative efficiency of TLDs [30]. It is given by

$$D_{LEM}(r) = \begin{cases} k & \text{for } r \leq a_0, \\ k(\frac{a_0}{r})^2 & \text{for } a_0 < r \leq R_{max}. \end{cases} \tag{2.33}$$

where k is a normalization factor ensuring that all energy deposited equals the mass stopping power, i.e. $LET = 2\pi \int_0^{R_{max}} D_{LEM}(r) r dr$. In D_{LEM}, a_0 is normally considered as a core parameter but here we interpret it as the radius of a centrally placed target in analog with D_{Site}. D_{Site} and D_{LEM} are shown in figure 2.9 and we use both to calculate the detector proton response. The LET-values used in D_{Site} and D_{LEM} are for Al_2O_3 as tabulated by NIST [47].

[3]Here, we take the linear energy transfer (LET) of the penetrating HPC to be the unrestricted LET, termed LET_∞ (see section 2.1.2).

For the δ-rays, we use a power law range-energy relationship adapted from Waligórski et al. scaled with a density factor to apply this relation in Al_2O_3 [89]. The main difference between the distributions is that all energy not

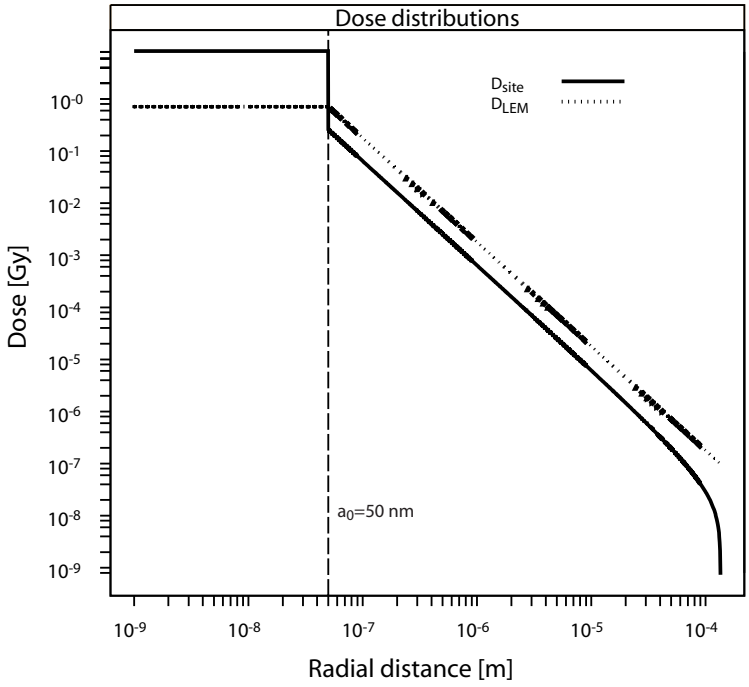

Figure 2.9: The two radial dose distributions D_{site} and D_{LEM} described by eq. (2.32) and eq. (2.33), respectively. The calculation is made for 100 MeV protons in Al_2O_3 with a_0=50 nm using a power law range-energy relationship adapted by Waligórski et al. scaled with a density factor for Al_2O_3 [89].

deposited by δ-rays is placed in the centrally positioned target in D_{Site} while this energy is distributed over the whole track in D_{LEM}. This means that the dose will be higher in D_{site} than D_{LEM} when $r < a_0$ and the opposite when $r > a_0$ in order to keep the areas under the curves equal. Also, the shape of the distributions around a_0 and R_{max} is different.

2.6 Proton response

We introduce two parameters by which most experimental and calculated data for the proton response will be represented. We define the supralinearity factor as

$$f(D) = \frac{S(D)/D}{S(D_0)/D_0} \tag{2.34}$$

where $S(D)$ is the dosimeter response at dose D and D_0 is in the linear region of the dose-response such that $f(D) = 1$ in the linear region. $f(D)$ only describes the dose-dependence for one type of radiation. In general, the relative efficiency, $\eta_{i\gamma}$, is defined as the ratio of the response per dose irradiated with an ion of energy i at a given dose, D, over the response per dose for γ-irradiation at the same dose:

$$\eta_{i\gamma} = \frac{\big[S(D)/D\big]_i}{\big[S(D)/D\big]_\gamma} \tag{2.35}$$

To estimate the effect on targets from a single proton track, we integrate the activation probability over the whole track and call this the activation cross-section. For a c-hit dosimeter, we have

$$\sigma_c = 2\pi \int_0^{R_{max}} P_c\big(D(r)\big) r dr \tag{2.36}$$

where R_{max} is the maximum distance of the δ-rays and D is either LEM or $Site$ and $c = 1$ or 2.

With $D = \phi \cdot LET$, the proton-response from a one-hit dosimeter, k_1, is given by

$$k_1 = 1 - e^{-\sigma_1 \phi} \tag{2.37}$$

where ϕ is the proton fluence. When the LET increases, the local dose close to the path of the proton approaches the saturation region of the detector response. In this situation, further energy deposition does not lead to a larger response and therefore the proton-response declines at high LET values (see figure 2.10). This means that $\eta_{i\gamma} \leq 1$ and due to the exponential form of eq. (2.37) we have that $f(D) \leq 1$. From eq. (2.28), (2.35) and eq. (2.37), we have for small doses that

$$\eta_{i\gamma} = \frac{1 - e^{-\sigma_1 \phi}}{1 - e^{-D/E_1}} \simeq \frac{\sigma_1 \phi}{D/E_1} = \frac{\sigma_1 E_1}{LET} \tag{2.38}$$

Eq. (2.38) is the expression usually used to calculate relative efficiencies for one hit detectors.

For a two-hit dosimeter, we have to distinguish between so-called "ion-kills" and "gamma-kills (γ-kills)" which somewhat artificially divides the two possible ways by which a two-hit target can be activated into two separate modes (see figure 2.11). In the ion-kill mode, the targets are activated by the δ-rays from a single proton and this is therefore a one-hit process [52]. Targets activated by two different protons are not counted in this mode. The process is best described by the concept of cross-section and one-hit (exponential)

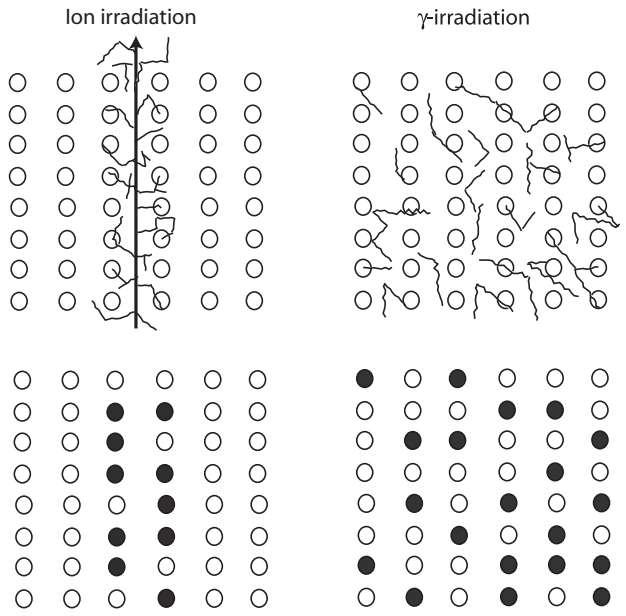

Figure 2.10: Due to the difference in ionization density, local doses reach saturation and fewer targets are available in the proton irradiation compared to the γ-irradiation. In the figure, the number of δ-rays are 30 but they are distributed differently in the ion- and γ-irradiation (the ion being the proton in our case). This leads to the activation of 10 and 20 targets respectively. If one take the number of δ-rays as the dose and the number of activated targets as the response, we get $\eta_{i\gamma}$=0.5.

statistics so the probability of not activating a two-hit dosimeter in this mode is given by

$$\Pi_{ion} = e^{-\sigma_2 \phi} \tag{2.39}$$

As proton energy decreases (LET increases[4]), R_{max} becomes smaller and the δ-rays gets more densely packed around the path of the proton compared to the more dispersedly distributed δ-rays from γ-irradiation at the same dose level. In this situation, the local dose around the path of the proton can be in the supralinear region (1-10 Gy in figures 5.8 and 2.9) and therefore $\eta_{i\gamma}$ might exceed 1 when the dosimeter response is dominated by a two-hit activation from this mode whereas $f(D) \leq 1$ due to the exponential behavior (see figure 2.12).

In the γ-kill mode, targets are activated by the δ-rays from different protons and is consequently a result of track overlap (see figure 2.11). Targets activated by the same proton is not counted in this mode. This resembles the

[4]Essentially, there is a one–to–one relation between proton energy and LET as will be discussed in fig. 5.2.

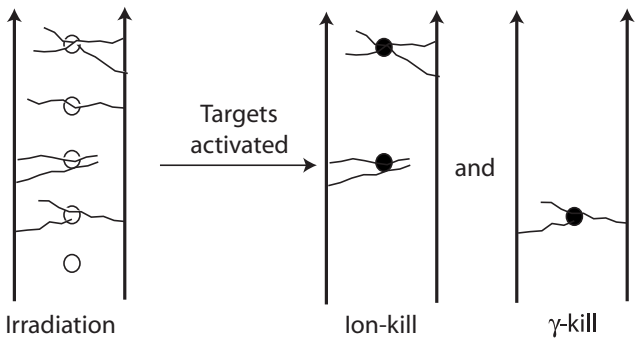

Figure 2.11: Two-hit activation can occur in two ways, either by two δ-rays from the same proton or by two δ-rays from two different protons. This is somewhat artificially separated into two different modes termed "ion-kills" and "γ-kills". The time scale in which activation in the ion-kill mode takes place is less than 10^{-15} seconds whereas the time scale in which activation in the γ-kill mode occurs is in the order of the irradiation time [17].

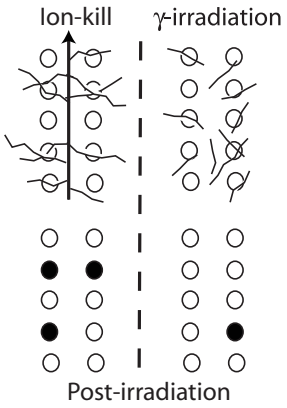

Figure 2.12: If R_{max} is not too small and the energy deposition not too large (i.e. until a certain LET-value), target activation in the ion-kill mode can increase the activation compared to γ-irradiation at the same dose level. This situation will lead to $\eta_{i\gamma} > 1$.

corresponding situation of γ-irradiation where targets are activated by δ-rays from different γ-ray photons. One does not use the concept of cross-section to estimate activation by γ-kills since this mode is described by conditional probability. Instead, a "saturation cross-section" is introduced to discriminate between the two modes (see appendix A.2). Above this cross-section only ion-kills take place. The fraction of dose contributing to the ion-kill mode is then given by

$$P_I = \frac{\sigma_2}{\sigma_0} \tag{2.40}$$

where σ_0 is the saturation cross-section and the fraction of dose contribution to the γ-kill mode is $D_\gamma = (1-P_I)D$. Activation from the γ-kill mode follows the statistics of γ-irradiation (see eq. (2.29)) and therefore the probability of not activating a target in this mode is given by

$$\Pi_\gamma = 1 - P_2(D_\gamma) \tag{2.41}$$

Since the response from this mode follows $P_2(D_\gamma)$, $\eta_{i\gamma} = 1$ and $f(D) \geq 1$ before saturation due to the supralinear behavior of P_2. The proton response from a two-hit dosimeter is then given by the probability of activation from either ion-kill or γ-kill as[5]

$$k_2 = 1 - \Pi_{ion}\Pi_\gamma \tag{2.42}$$

and the proton response from a two-component one- and two-hit dosimeter is given by

$$\frac{OSL_p(D)}{OSL_\gamma^{max}} = Rk_1 + (1-R)k_2 \tag{2.43}$$

where OSL_p is the calculated proton response from a given dosimeter and OSL_γ^{max} and R is the saturation response and fraction of one-hit at γ-irradiation for that dosimeter. The first term effects both the efficiency $\eta_{i\gamma}$ and supralineariy factor $f(D)$ to be less than one. In the second term, $f(D) \leq 1$ for the ion-kill mode and $f(D) \geq 1$ for the γ-kill mode. As the LET increases, the ion-kill mode becomes more dominating and $f(D)$ will decrease whereas $\eta_{i\gamma}$ will increase. Increasing the dose, the γ-kill mode becomes more dominating since $1 - \Pi_\gamma$ increases supralinearly with dose whereas in the ion-kill mode $1 - \Pi_{ion}$ increases linearly with dose.

[5]The probability of not being activated by neither ion- nor γ-kill is $\Pi_{ion}\Pi_\gamma$. Therefore, the probability of activation from either mode is given by $1 - \Pi_{ion}\Pi_\gamma$.

3 Experimental details

This chapter gives a detailed description of the detection systems and crystals and fibers used to collect the experimental data presented in chapter 4 and 5. First, the RL/OSL fiber system which was used in both the temperature and proton experiments is presented. Then, a modified version of the standard TL/OSL Risø reader, used in one of the temperature experiments, is described and then the two different Al_2O_3:C crystal growths applied in the experiments together with the optical fiber cables are presented. Finally, the OSL protocol used in the experiments is described.

3.1 The RL/OSL fiber system

The optical fiber dosimeter system is shown in figure 3.1 and carries the abbreviation ME03 (medical product # 3). The system is controlled by a laptop that has access to two ME03 readers and is therefore easy to transport. The ME03 readers are controlled by a parallel Labview interface from the laptop through a data acquisition card (6036 PCMCIA) by National Instruments and data are stored in an ASCII file.

The data are usually sampled at a rate of 10 samples per sec (10 Hz). A schematic diagram of the prototype optical fiber dosimetry system is shown in figure 3.2. During treatment, the RL signal which mainly consists of blue light (around 420 nm) is carried back from the Al_2O_3:C dosimeter through the optical fiber cable and reflected in a 90° angle by the beam splitter into a photomultiplier tube (PMT). The beam splitter is a dichroic colour beamsplitter (Delta BSP 480) positioned in a 45° angle relative to the incident beam and the PMT is a Perkin-Elmer photomultiplier tube (CP-982) which has a low dark count signal (3-5 counts per second) and an almost constant response from 200 to 650 nm. The luminescence signal is focused onto the PMT via a lens through a band pass filter (BP25-395440 with band pass from 395-440 nm).

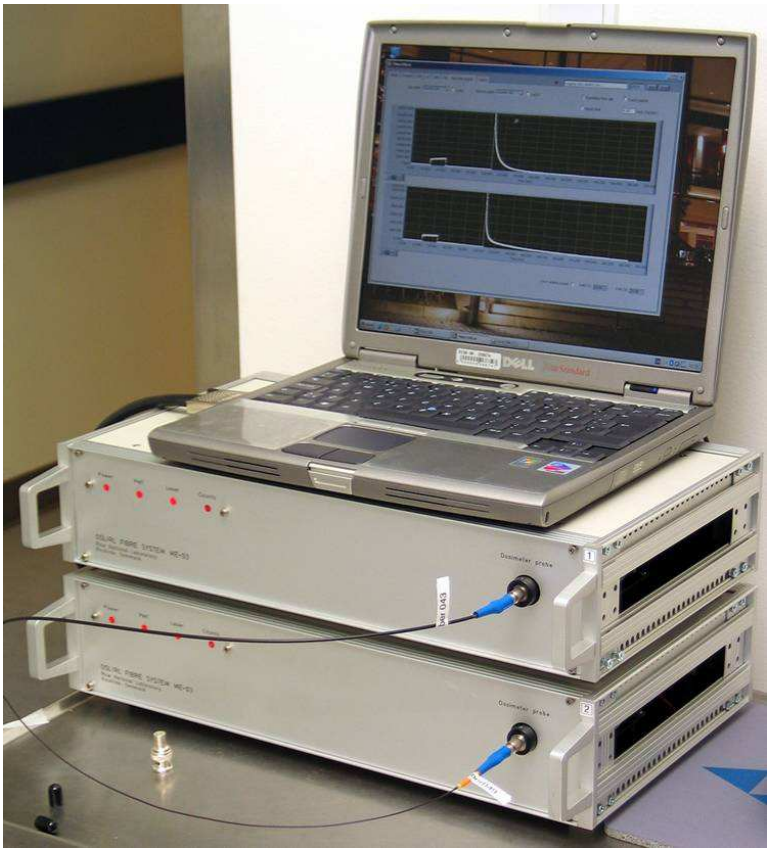

Figure 3.1: The fiber system ME03. Two readers are stacked on top of each other each having one fiber cable attached. A laptop controls both readers and the RL and OSL signals from the two probes can be seen in the Labview program interface.

To produce OSL, a green laser beam (Laser2000, frequency doubled YAG laser, 532 nm, 20 mW) is focused through the beam splitter and a collimator onto the Al_2O_3:C dosimeter via the optical fiber cable. The beam splitter is capable of transmitting more than 90 % of the light in the 500 to 700 nm region. When the laser light interacts with the Al_2O_3:C crystal, OSL is produced and transmitted back through the fiber together with laser light reflected by the crystal. The beam splitter reflects more than 99 % of the light in the 390-425 nm region which means most of the luminescence light. Any reflected laser light is removed by the band pass filter in front of the PMT such that only the luminescence signal is recorded.

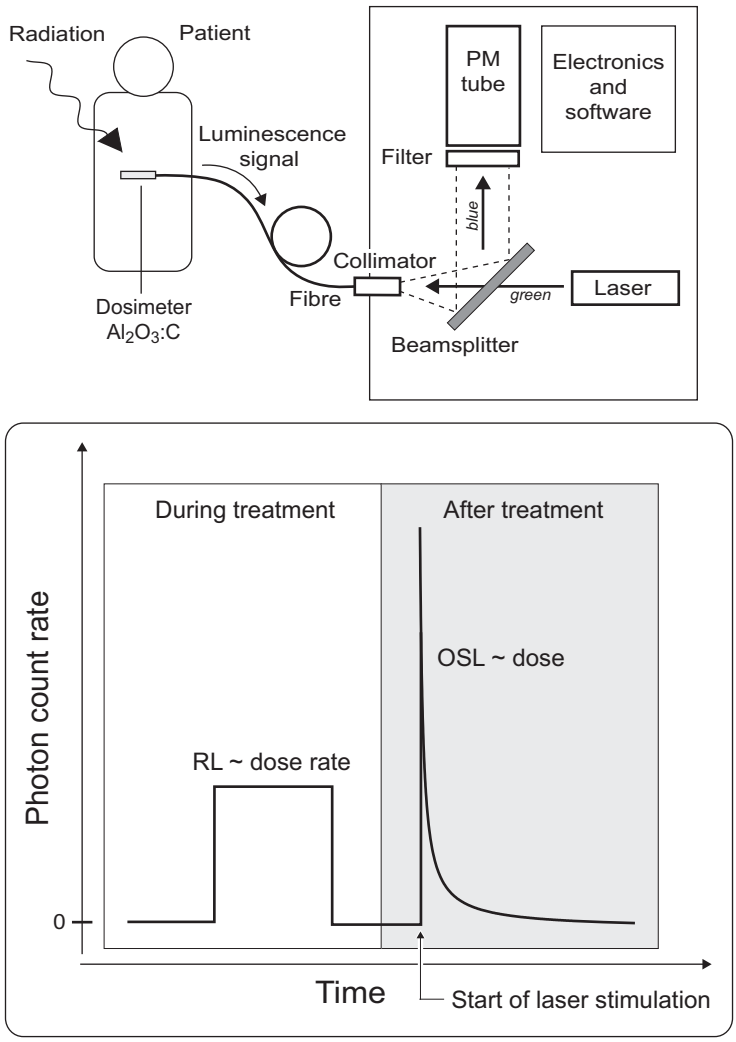

Figure 3.2: A sketch of the fiber system ME03 illustrating an *in–vivo* measurement (top). The Al_2O_3:C probe is placed inside a patient and the RL signal is recorded. After irradiation, the OSL decay curve is recorded by stimulation with a laser (bottom).

3.2 The TL/OSL Risø dosimetry system

Figure 3.3 shows the latest version of the Risø reader model TL/OSL-DA-20. However, the components of interest for this study are identical with the TL/OSL-DA-15 model used in the temperature experiments.

The Risø TL/OSL measurement system basically consists of a turnable wheel where up to 48 samples can be placed and individually be either heated, irradiated or optically stimulated. In this way the Risø reader can per-

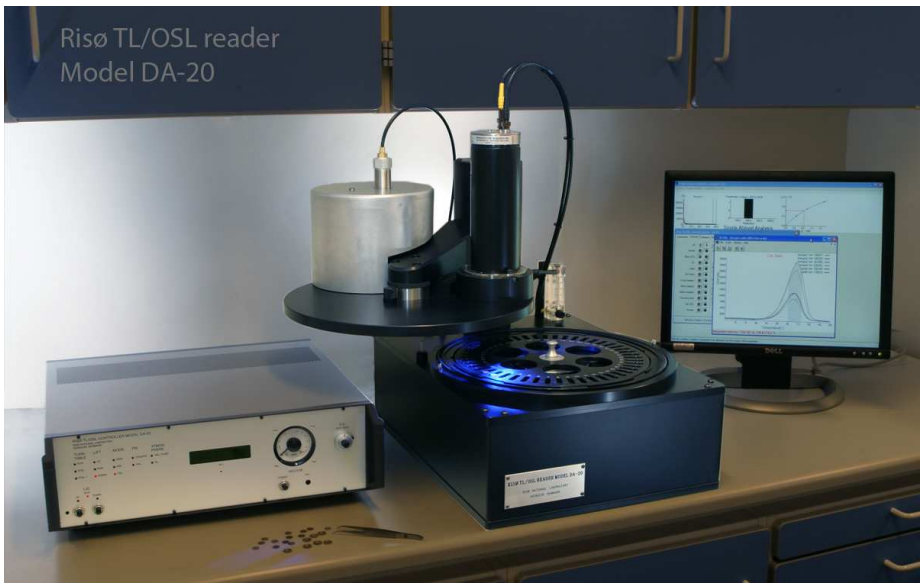

Figure 3.3: The latest version of the Risø reader (TL/OSL-DA-20). To the left is shown the minisys system which provides the basic low-level commands to the reader (middle). The experimental sequences and data collection can be handled from a windows based software (right).

form both TL and OSL measurements. The modified Risø reader used in the temperature experiments is shown in figure 3.4 and is also capable of performing RL measurements. The heating element and lift mechanism is located directly underneath the photomultiplier tube (standard) and irradiation source (optional). The heater strip is made of Kanthal (a high resistivity alloy) and accomplished by feeding a controlled current through the heating element. Feedback control of the temperature employs an Alumel-Cromel thermocouple mounted underneath the heater strip and heating is provided by a non-switching continuous full sine wave generator operating at 20 kHz. The heating system is able to heat samples to 700 °C at linear heating rates from 0.1 to 30 K/s.

The standard PMT in the Risø reader is a bialkali EMI 9235QA PMT, which has maximum detection efficiency at approximately 400 nm. A commonly used detection filter is Hoya U-340, which has a peak transmission around 340 nm (FWHM = 80 nm) and therefore captures the tail of the broad F-center emission band in Al_2O_3:C. Connecting the RL unit to the OSL unit through an optical fiber cable enables the RL to be monitored as well.

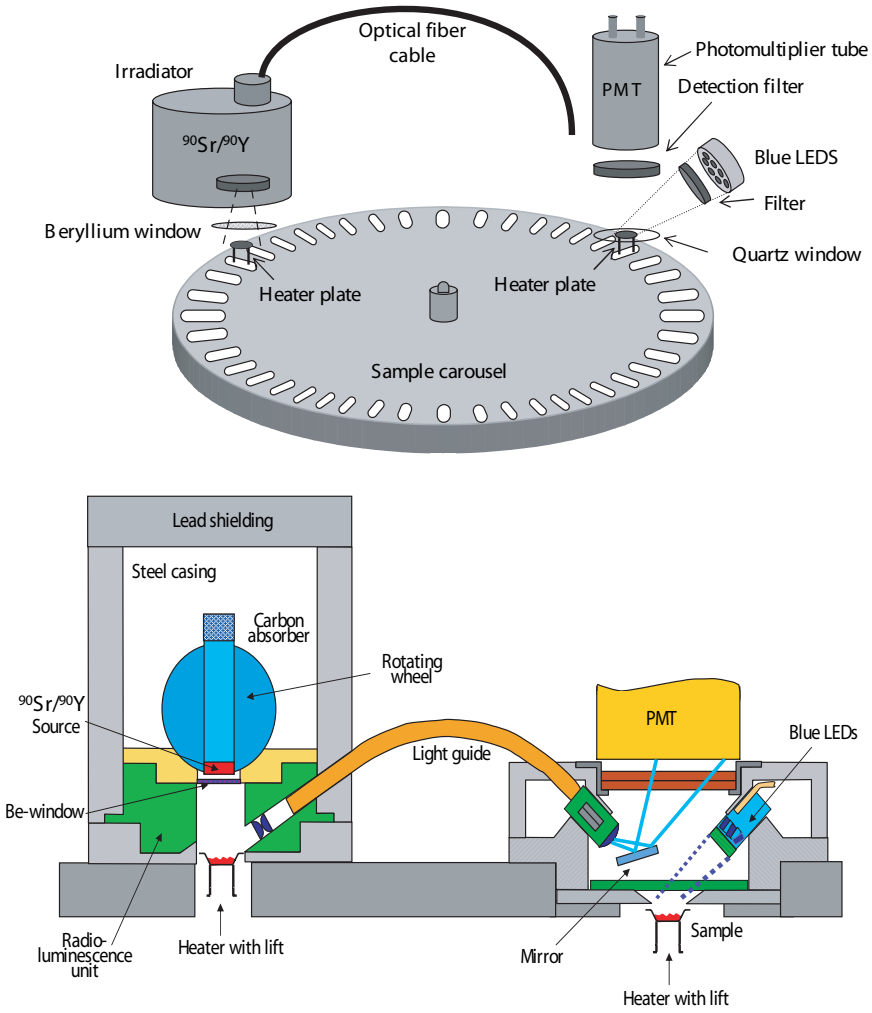

Figure 3.4: A sketch of the modified Risø reader. The sample can be heated during both irradiation and stimulation and both the RL and OSL signals are recorded.

The OSL is carried out with blue LEDs (NISHIA type NSPB-500s) with a peak emission at 470 nm (FWHM = 20 nm). The intensity for one LED at a distance of 2 cm is 1.9 mW per cm^2. The blue LEDs are usually arranged in a ring-shaped holder with 4 clusters each containing seven individual LEDs. The total power from 28 LEDs is > 40 mW/cm^2 at the sample.

3.3 Fiber crystals

Figure 3.5 shows the two different Al_2O_3:C crystal growths used in this study. The thin crystal (left) is a $2\times0.5\times0.5$ mm^3 cut from a bulk crystal grown by Landauer Inc. using the Czochralksi technique. It is named according to its growth method and number and therefore denoted CZ#60. The thick crystal (right) is a $2\times1\times0.8$ mm^3 cut from single crystal standard pellet (5 mm in diameter and 1 mm in thickness) grown according to the Stepanov method and Laser Heated Pedestal Growth method and commonly known under the commercial name TLD-500.

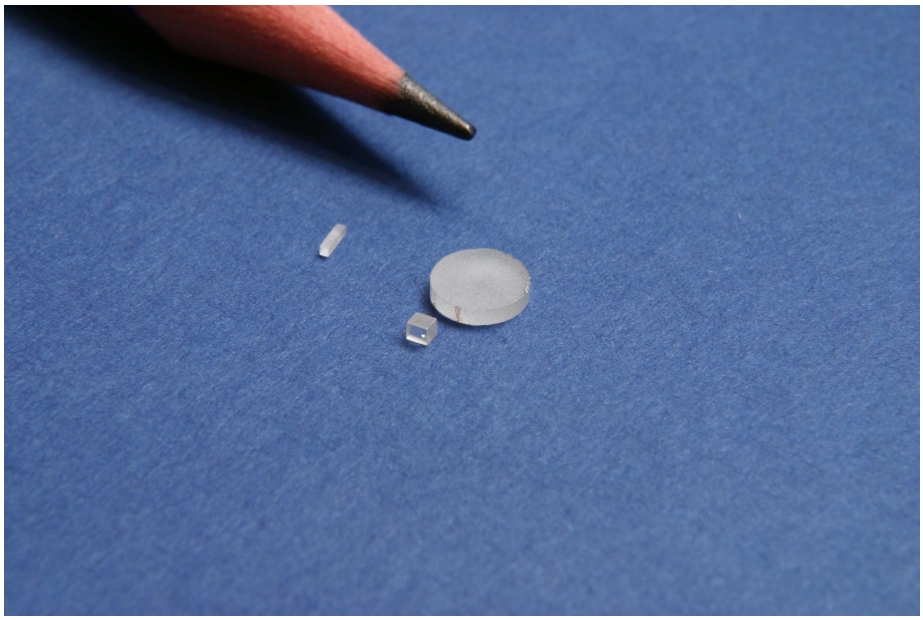

Figure 3.5: The two types of Al_2O_3:C crystals named TLD-500 (right) and CZ#60 (left). The TLD-500 crystal is cut from a standard pellet as the one shown in the figure.

The crystals are attached to optical fiber cables as shown in figure 3.6. In order to protect the crystals against light, i.e. bleaching, and the harsh hospital environment (tight bends in catheters and humid environment), a jacket made from araldite is cast around the exposed crystal and fiber area. The fiber cables used are plastic fibers with a polymethyl methacrylate (PMMA) core that transport the light. Two different types of fiber cables depending on the size of the crystal were used. In the case of the TLD-500 crystal cut, a Super Eska SK-40 (Mitsubishi Rayon Co., LTD., Japan) optical fiber with a 1 mm PMMA core and a total diameter of 2.2 mm including cladding and a jacket was used. In the case of the smaller CZ#60 crystal, a GH-2001-P

fiber (also from Mitsubishi Rayon Co., LTD.) was used resulting in a total diameter of 1 mm.

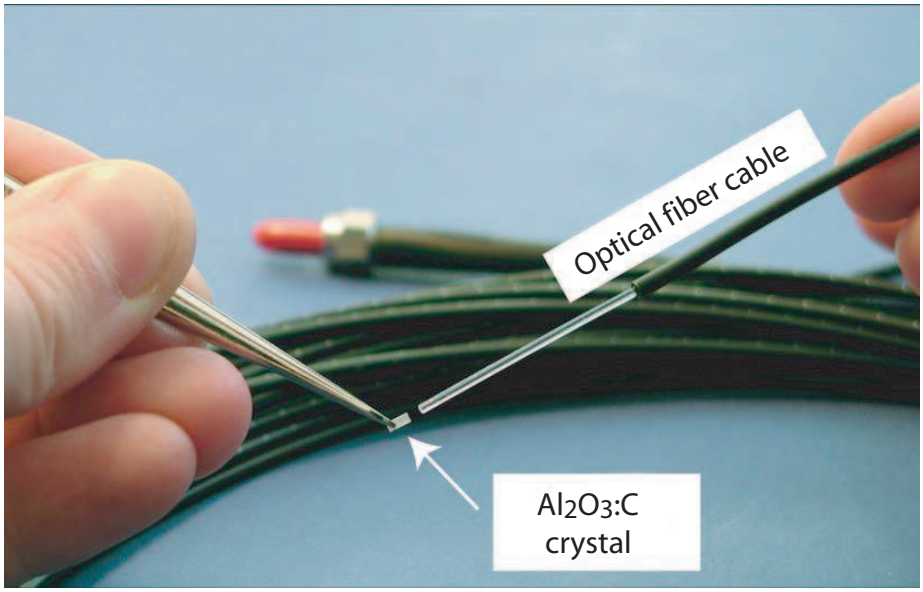

Figure 3.6: The figure shows the coupling between the optical fiber and the attached Al_2O_3:C crystal.

3.4 OSL Protocol

It is mentioned, both in the introduction and overall conclusion, that different protocols can be applied to read out the luminescence signal. To clearly emphasize the luminescence protocol applied in all the experiments presented in this thesis, we therefore describe it in more detail.

The lower diagram in figure 3.2 illustrates the so–called continues wave OSL (cw-OSL) protocol that has be used to read out the OSL signal in all experiments. During irradiation, a RL signal is passively recorded by the PMT of the system (either the RL/OSL fiber system or the modified Risø reader). After irradiation, a light source with constant intensity (either a laser or LEDs) is illuminating the irradiated crystal and an OSL decay curve is obtained which can then be used for OSL dosimetry.

It is important to note, that the crystals used in this thesis are re–used for new irradiations and measurements after the OSL signal has been read out. This is in sharp contrast to other cw-OSL protocols where the irradiated

samples, e.g. Luxel^{TM} dosimeters, are only irradiated once and then thrown away after the OSL signal has been read out.

As described in the theory section, electrons and holes are being captured by crystal traps during irradiation. During stimulation, these charge carries are stimulated into the delocalised energy bands and recombine which ideally resets the crystal to its initial state. Depending on the wavelength and intensity of the stimulation light, however, electrons and holes captured by deep traps in the crystal are not necessarily released during the stimulation process. This transfer the crystal into a state which is different from the one it had before irradiation. If the crystal is thrown out after one irradiation, this change in state does not matter but if the crystal is used for multiple irradiation and OSL readouts it is an important issue.

Usually, new crystals that are intended for re-use need to be irradiated and read out repeatedly until the deep traps that are not reached by the stimulation light are completely filled. Hereafter, an equilibrium state is reached to which the crystal is reset after irradiation and subsequent stimulation has been carried out. Although the crystals used in this study are believed to be in such an equilibrium state, differences between OSL results obtained with re-used samples and one-time samples could be ascribed to differences in state of the crystals before irradiation begins.

4 Temperature effects

The objective of this chapter is to quantify temperature effects on the RL and OSL output in the room-to-body temperature range. Results from laboratory experiments using both crystals unattached to fiber cables and fiber-coupled crystals are analyzed and possible explanations for the temperature effects are discussed on the basis of model calculations as given by equations (2.11) through (2.15).

The mechanisms causing a temperature dependence of the OSL response from Al_2O_3:C have been studied before but usually at high temperatures (> 100 °C) or short stimulation times [58, 65]. The prime study is from Markey et al. and the main result is shown in figure 4.1. From this experiment, it is clear that the OSL is increasing with temperature when only the initial part of the OSL signal is being monitored [58]. This chapter will, however, present data that shows that the OSL increase depends on both the stimulation and irradiation temperature and on which part of the OSL signal that is used.

Several physical mechanisms have been proposed to cause the temperature dependence of the OSL signal. Although the effects have been ascribed to localized recombination through donor-acceptor hopping via intermediate states [75] and band tail hopping [74] attention is here given to charge transitions through the conduction band as described by the energy band model in section 2.3.3. When delocalised recombination is dominating, shallow traps and thermal excitation from optically excited states are the most probable mechanisms to explain temperature effects on the OSL signal [58, 65, 44]. Other important mechanisms are thermal quenching and changes in the charge competition conditions. In section 4.3, the thermal mechanisms will be explained in more detail and it will be demonstrated that thermal quenching is not relevant in this study.

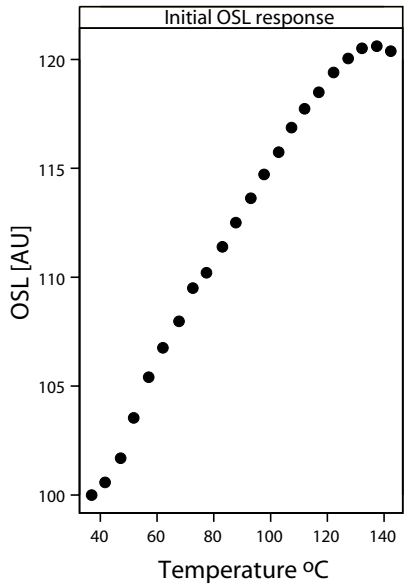

Figure 4.1: The initial OSL signal versus temperature as published by Markey et al. [58]. The sample was irradiated with 1.5 Gy at room temperature whereafter it was heated at a linear rate of 2 °C per sec from room temperature to 550 °C. During the heating, the sample was exposed to periodic green light stimulations of 0.1 s duration. In this way, the initial OSL signal is monitored with increasing stimulation temperature. The decrease in signal starting around 130 °C is believed to be partially due to the emptying of the main dosimetry trap and partially due to thermal quenching.

4.1 Samples and experimental details

4.1.1 Samples

Two types of carbon doped aluminum oxide were used: An Al_2O_3:C single crystal commonly known as TLD-500 [6] and CZ#60. The CZ#60 crystals were grown by Landauer Inc. using the Czochralksi method [22]. A total of seven crystals were used for the experiments. As listed in table 4.1, four of these were attached to optical fiber cables (further details are available in section 3.3).

4.1.2 Experiments

The luminescence measurements with fiber-coupled crystals were carried out using the RL/OSL fiber reader which includes a photomultiplier tube (395-440 nm detection window) and a 20 mW 532 nm laser [10] (see section 3.1). Due to the specific transmission properties of each fiber cable, the laser inten-

ID	Material	Size	Crystal	Experiment
TLD-500	TLD-500	Ø 5 mm, 0.7 mm	bare	Reader
CZ#60-A	CZ#60	Ø 0.48 mm, 4 mm	bare	Reader
CZ#60-B	CZ#60	Ø 0.48 mm, 4 mm	bare	Reader
fiber40B	TLD-500	2.59x0.94x0.85 mm^3	fiber coupled	Block
fiber43	TLD-500	1.99x1.03x0.83 mm^3	fiber coupled	Room/Body, Stim
fiber53	CZ#60	Ø 0.48 mm, 4 mm	fiber coupled	Room/Body, Stim, Peltier
fiber59	CZ#60	Ø 0.48 mm, 4 mm	fiber coupled	Peltier

Table 4.1: Bare and fiber-coupled crystals used in the experiments. The ID column shows the names used to identify the crystals and the experiment column shows in which experiments the crystals were used.

sity reaching the crystal at the end of the fiber is only a fraction of the initial intensity ($\sim 50\%$). Measurements on crystals not attached to fiber cables, in the following refereed to as "bare crystals", were made with a modified version of an automated Risø TL/OSL reader (TL/OSL-DA-15, Denmark) having a Hoya U340 detection filter and blue light-emitting diodes (40 mW/cm^2) (see section 3.2) [76]. The OSL readouts were made at constant stimulation intensity (i.e. as cw-OSL) and the stimulation was maintained until the crystals were considered "fully bleached". This was either 600 or 900 seconds for the fiber experiments and 300 seconds for the Risø reader experiments. All experiments consisted of a series of repeated irradiations and OSL-readouts where only the temperature was changed. In the absence of any temperature effects, the luminescence output within each experiment was expected to be constant.

Five experiments were carried out covering various extended intervals around the room/body temperature region. In the first experiment named "Stim", only the stimulation temperature was varied whereas the irradiation temperature was kept constant. In all other experiments, both irradiation and stimulation temperatures were varied - either independently of each other (as in the experiment named "Room/body") or non-independently of each other as in the last three experiments named "Reader", "Block" and "Peltier". For the latter experiments, stimulation was always carried out at the same temperature as the preceding irradiation.

In the "Stim" experiment, fiber43 and fiber53 were placed on a 50 W Peltier cooling/heating element and irradiated at a dose-rate of 1 mGy/s using a Varian VF-50J X-ray tube (50 kV, 1 mA) [11]. Temperature effects were investigated in the range from 10 to 50 °C using a test dose of 100 mGy. In all other experiments, a $^{90}Sr/^{90}Y$ β–source were used for irradiations. In the "Room/Body" experiment, fiber43 and fiber53 were placed on a 7.5 W Peltier heating element and irradiated at a dose-rate of 1.5 mGy/s. The tem-

perature was changed between 25 °C (room) and 41 °C (∼ body) depending on whether irradiation or stimulation was performed. In this experiment a test dose of 450 mGy was used. In the "Reader" experiment, bare crystals were placed on a low-mass heater strip and irradiated at a dose-rate of 24 mGy/s. The temperature dependence was investigated in the range from 30–100 °C using a 2.4 Gy test dose. In the "Block" experiment, fiber40B was placed on a heated/cooled brass block and the temperature was monitored during irradiation and stimulation. The fiber was irradiated at a dose-rate of 0.4 mGy/s in the range from 0–45 °C using a test dose of 32 mGy. In the "Peltier" experiment, fiber53 and fiber59 were placed on the 7.5 W Peltier heating element. The crystals were irradiated at a dose-rate of 1.5 mGy/s in the range from 20–50 °C using a test dose of 0.9 Gy. The experiments are summarized in table 4.2 and figure 4.2 illustrates the principle of how the measurements using a Peltier element (experiments "Stim", "room/body" and "Peltier") were carried out.

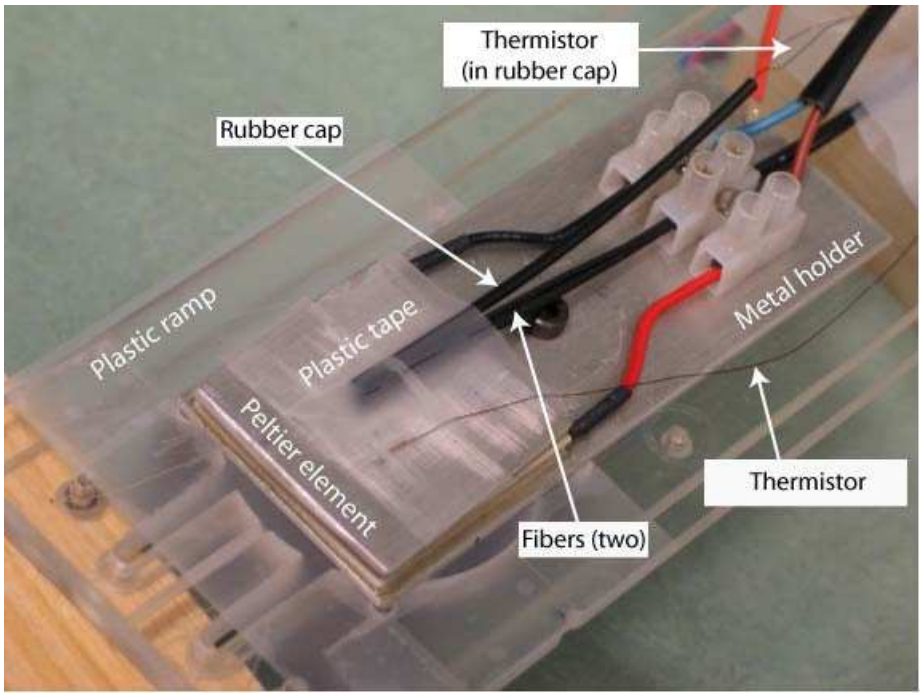

Figure 4.2: Two fibers are mounted on a metal holder with a Peltier element at the end where the crystals are located. The holder is then attached on a plastic ramp which is mounted under a radiation source. The picture is taken from the "Peltier" experiment with fiber53 and fiber59 mounted on the 7.5 W Peltier element.

Experiment	Irr. temp.	Stim. temp.	Test dose [Gy]	Temp. [^{o}C]
Stim	const	varies	0.1	10–50
Room/Body	varies	varies	0.45	25–41
Reader	varies	varies as irr.	2.4	30–100
Block	varies	varies as irr.	0.032	0–45
Peltier	varies	varies as irr.	0.9	20–50

Table 4.2: The temperatures and test doses provided in the different experiments. The columns "irr. temp." "stim. temp." indicate whether the irradiation and stimulation temperature were constant (const), varied (varies) or changed as the irradiation temperature (varies as irr.).

4.2 Results

4.2.1 Constant irradiation temperature

In the "Stim" experiment, fiber43 and fiber53 were placed on the Peltier element together with a small temperature sensor inside a piece of rubber cap to most ideally imitate and monitor the temperature conditions the crystal inside the fibers are facing (as in figure 4.2). Irradiation was made at 25 °C (room temperature). The temperature was then changed and stimulation was carried out. After the stimulation, irradiation was again made at 25 °C whereafter the temperature was changed for stimulation etc. The stimulations were carried out at 25, 25, 10, 50, 20, 50, 15, 45, 35, and 40 °C. This "randomly" selected sequence was then repeated five times. The OSL responses for different integration times are plotted in figure 4.3. The values shown are means of all repetitions at the given temperatures and the OSL value at 25 °C was chosen as reference.

For short integration times, the OSL is increasing with stimulation temperature and for long integration times it is decreasing. This indicates that an intermediate integration time exists where the OSL signal is (nearly) independent of stimulation temperature when the irradiation temperature is constant. This integration time is shown in the middle panel and given explicitly for the two fibers in the figure caption. The OSL signal increased about 0.1 and 0.16% per °C at short integration times and decreased 0.08 and 0.06% per °C at long integration times for fiber43 and fiber53, respectively. The integrated RL signal is plotted in figure 4.4. For both crystals, the RL response is independent of the temperature of the preceding OSL.

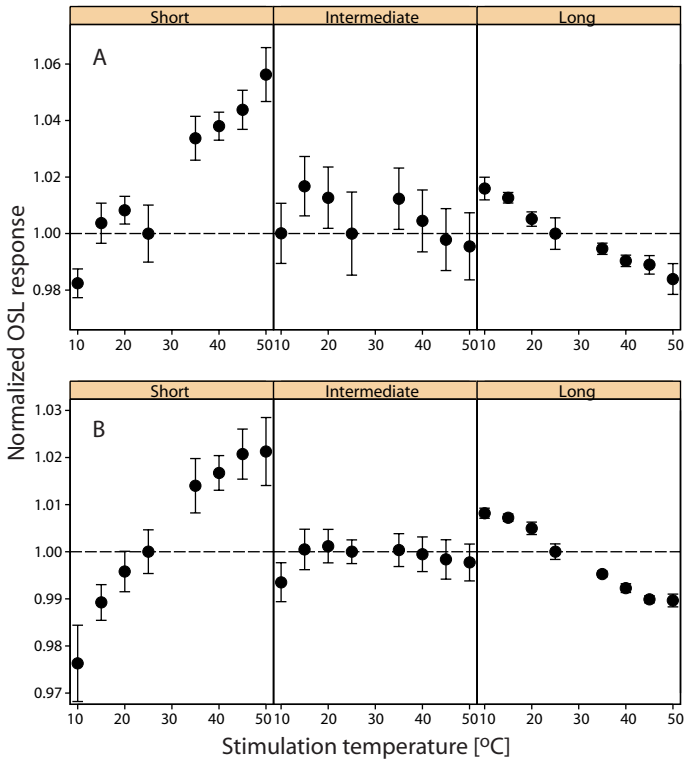

Figure 4.3: Integrated OSL response from **A** fiber53 (CZ#60 crystal) and **B** fiber43 (TLD-500 crystal). The panels show the OSL responses for short (left), intermediate (middle) and long (right) integration times. In **A** short=0.15 seconds, intermediate=6.6 seconds and long=600 seconds. In **B** short=0.7 seconds, intermediate= 7.6 seconds and long=600 seconds. The OSL response at 25 ^{o}C was used as a reference.

4.2.2 Variable irradiation temperature

In the "Room/Body" experiment, fiber43 and fiber53 were mounted on another Peltier element and subjected to the following measurement protocol:

Temperature combination	1	2	3	4
Irradiation (RL) temperature [°C]	25	25	41	41
Stimulation (OSL) temperature [°C]	25	41	41	25

A sequence of irradiation and stimulation temperatures consists of combination 1 to 4 (as indicated above) and this sequence was then repeated 27 times. The data presented in figure 4.5 are therefore average values of 27 repetitions. Figure 4.5 shows the integrated RL and OSL values for long integration times. For a constant irradiation temperature (combination 1+2 and 3+4, respectively) the OSL signal decreased with increasing stimulation

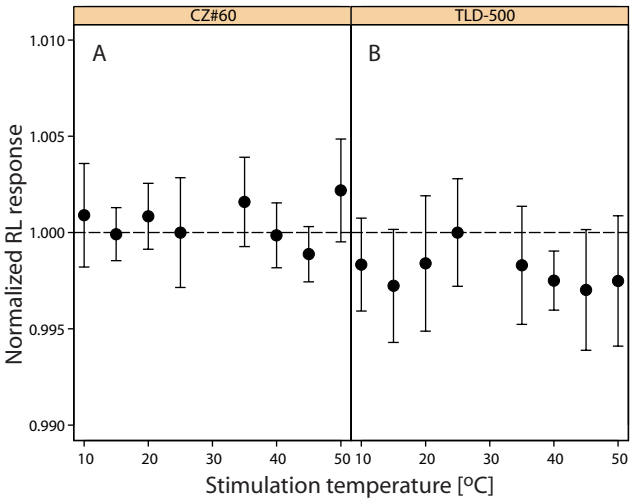

Figure 4.4: Integrated RL response from **A** fiber53 (CZ#60 crystal) and **B** fiber43 (TLD-500 crystal). The RL response following the OSL readout at 25 ^{o}C was used as a reference.

temperature. For short integration times ($\sim$ 1 s) the OSL signal increases (data not shown). This is consistent with figure 4.3. The integrated RL signal from both fibers display an underresponse when irradiation takes place around body temperature (41 °C) compared to irradiation at room temperature (25 °C).

The combined results in figures 4.4 and 4.5 show that the RL response depends only on irradiation temperature and not on the temperature of the preceding OSL. In contrast, the OSL response depends on both irradiation and stimulation temperature. The integrated OSL decreases or increases about 2% and the integrated RL decreases about 3% when changing the irradiation and/or stimulation temperature 16 °C (from room to body and visa versa). This covers an overall variability in RL and OSL of at most 0.2% per °C. No thermoluminescence signal was observed between irradiation and stimulation when either heating or cooling the crystals.

4.2.3 The same irradiation and stimulation temperature

In the "Reader" experiment, the TLD-500, CZ#60-A and CZ#60-B crystals were measured in a modified Risø reader and irradiation and stimulation were carried out at the same elevated temperatures. The RL response and the first 2 seconds of the OSL response from the CZ#60-A crystal at different temperatures (30, 60 and 100 °C) are shown in figures 4.6A and 4.7A. Here,

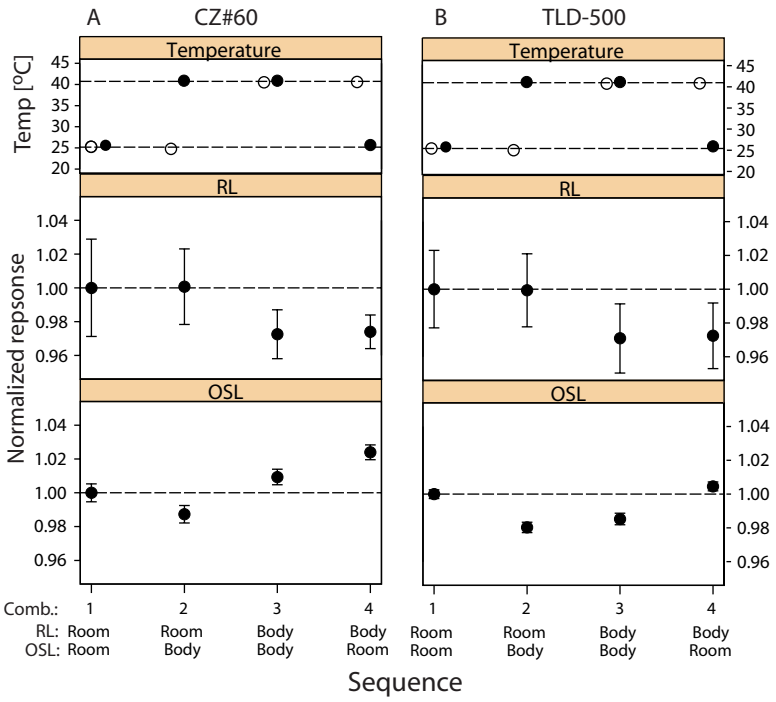

Figure 4.5: Integrated RL and OSL response in the "Body/Room" experiment for **A** fiber53 (CZ#60 crystal) and **B** fiber43 (TLD-500 crystal). Top panel: Closed circle=stimulation (OSL) temperature and open circle=irradiation (RL) temperature. Middle panel: Average integrated RL response (over irradiation time) with standard deviation from 27 repetitions. Low panel: Average integrated OSL response (900 seconds) with standard deviation from 27 repetitions.

the RL and OSL signals both increase systematically with temperature. The overall change in RL and OSL response with temperature was the same for all the crystals in the "Reader" experiment. The magnitude did, however, change from crystal to crystal.

In the "Peltier" experiment, fiber53 and fiber59 were placed on a Peltier element and both RL and OSL were recorded at 20 ^{o}C, 30 ^{o}C and 50 ^{o}C. The RL signals of fiber59 from this experiment are shown in figure 4.6B. Here, the RL slopes (i.e. the change in RL count rate pr. dose unit) did not

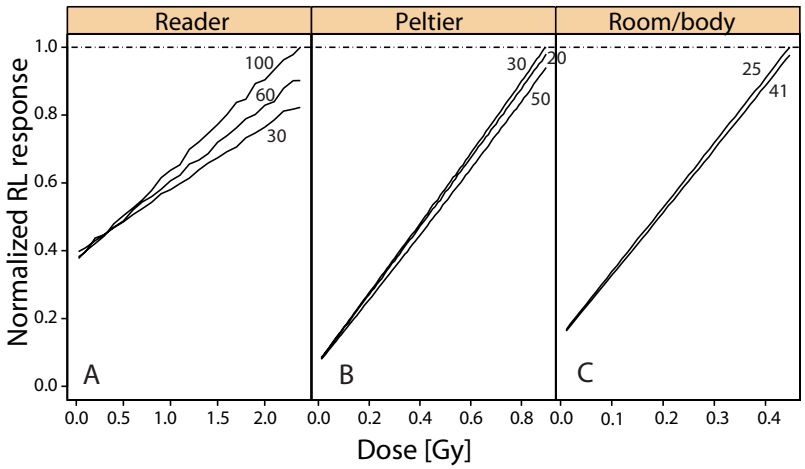

Figure 4.6: Normalized RL behavior for three different crystals in three different experiments. **A**: Crystal CZ#60-A in the "Reader" experiment. **B**: Fiber59 in the "Peltier" experiment. **C** Fiber53 response from combination 1 and 3 in the "Room/body" experiment. The numbers indicate irradiation temperature in ^{o}C.

vary systematically with temperature although the OSL peak increased with temperature in figure 4.7B.

The RL and OSL responses from the "Room/body" experiment are shown in figures 4.6C and 4.7C for fiber53. A lower RL sensitivity is identified at body temperature (41 °C) compared to room temperature (25 °C). The OSL peak is again seen to increase with temperature.

Although the development in the RL behavior as seen in figures 4.6A, B and C is quite different for the different experiments, the samples display the same change in OSL response with temperature (fig. 4.7A, B and C). To quantify this systematic OSL variation with temperature when the irradiation and stimulation is carried out at the same temperature, a temperature coefficient, ν, is defined as

$$\nu_{temp}^{int} = \frac{OSL_{temp}^{int} - OSL_{temp1}^{int}}{OSL_{temp1}^{int} \cdot (temp - temp1)} \tag{4.1}$$

where OSL_{temp}^{int} is the integrated OSL signal at a given integration time, int and a given temperature, $temp$. $temp1$ is the reference temperature specific for each experiment. The reference temperatures are 30, 22 and 20 °C for "Reader", "Block" and "Peltier" experiment, respectively. Table 4.3 gives the relative change in OSL with temperature. For a given experiment and sample, the OSL_{temp}^{int} value is the mean of all OSL measurement performed at that temperature. The total number of OSL measurements at all temperatures is

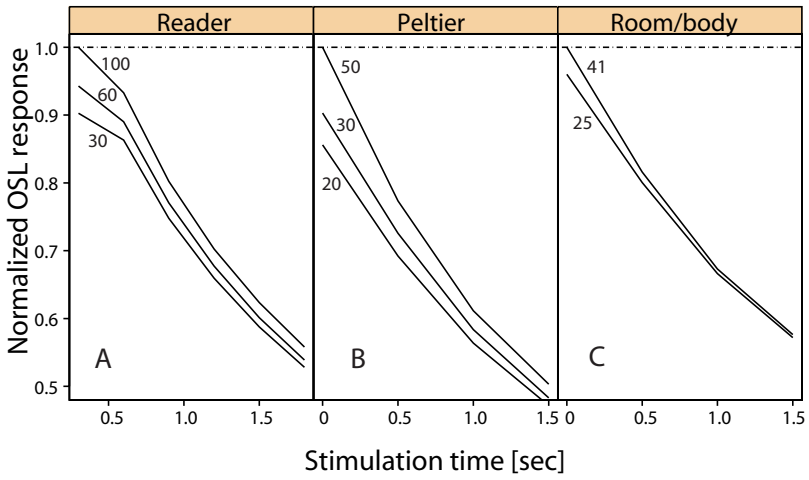

Figure 4.7: Normalized OSL behavior for three different crystals in three different experiments. **A**: Crystal CZ#60-A in the "Reader" experiment. **B**: Fiber59 in the "Peltier" experiment. **C** Fiber53 response from combination 1 and 3 in the "Room/body" experiment. The numbers indicate stimulation temperature in ^{o}C. The OSL behavior demonstrated in **A**, **B** and **C** was the same for all crystals involved in the above experiments.

given by the number N. The tabulated v is the mean of v-values calculated at a different temperatures. The number of temperatures involved in the mean different from the reference temperature is given by n. For example, we have for fiber53 in the "Peltier" experiment $n = 2$ (30 and 50 °C) and $N = 50$ repetitions at all temperatures. 50 seconds of integration time gives $v^{50}_{mean} = (v^{50}_{30} + v^{50}_{50})/2 = 0.66\%$ per °C. Using this approach of calculating v, we implicitly assume that the OSL is changing linearly with temperature. ν is generally decreasing with integration time (most pronounced going from 5 to 50 seconds) and overall, the OSL signal is increasing between 0.1-0.6 % per °C. At long integration times ν is increasing for fiber40B and the TLD-500 crystal.

OSL shape

To quantify the change in OSL decay rate with temperature, an OSL shape parameter was introduced. This specifies the time at which half of the total integrated OSL signal, $OSL^{int}(t_{total})$, is read out. The OSL shape, t_{shape}, is defined as

$$OSL^{int}(t_{shape}) = \frac{OSL^{int}(t_{total})}{2} \tag{4.2}$$

The average values of the OSL shape at different temperatures are given in table 4.4. Except for the TLD-500 crystal, t_{shape} is decreasing with tempe-

Experiment	Peltier				Block			Reader				
Test dose	0.9 Gy				32 mGy			2.4 Gy				
Integration time	fiber53	fiber59	n	N	fiber40B	n	N	TLD-500	CZ#60-A	CZ#60-B	n	N
[sec]	[%/°C]				[%/°C]			[%/°C]				
5	0.91±0.35	0.33±0.04	2	50	0.49±0.25	4	9	0.0003±0.0002	0.10±0.001	0.10±0.016	2	8
50	0.66±0.31	0.21±0.08	2	50	0.23±0.15	4	9	0.050±0.008	0.087±0.004	0.094±0.019	2	8
100	0.63±0.30	0.20±0.08	2	50	0.17±0.16	4	9	0.058±0.011	0.091±0.005	0.097±0.019	2	8
200	0.62±0.30	0.20±0.08	2	50	0.21±0.16	4	9	0.061±0.013	0.093±0.005	0.098±0.019	2	8
300	0.62±0.30	0.19±0.08	2	50	0.26±0.16	4	9	0.061±0.013	0.093±0.005	0.099±0.019	2	8
600	0.62±0.30	0.19±0.08	2	50	0.46±0.19	4	9	–	–	–		

Table 4.3: The OSL temperature coefficient v for the different crystals in the different experiments. N is the total number of measurements at all temperatures while n is the number of temperatures besides the reference temperature used to calculate the average of v. See also text for details.

Temperature	Peltier [s]		Block [s]	Reader [s]		
[°C]	fiber53	fiber59	fiber40B	TLD-500	CZ#60-A	CZ#60-A
0	-	-	8.32	-	-	-
20	4.34	5.10	7.71	-	-	-
30	4.02	4.99	7.98	20.65	2.29	2.62
40	-	-	7.60	-	-	-
50	3.66	4.56	7.50	-	-	-
60	-	-	-	21.10	2.22	2.53
100	-	-	-	21.57	2.12	2.40

Table 4.4: The average OSL shape parameters t_{shape} for the different crystals, experiments, and temperatures. The integration time, t_{total}, is 300 seconds in the "Reader" experiment and 600 seconds in the "Block" and "Peltier" experiments.

rature, i.e. the OSL signal is decaying faster with increasing temperature.

4.3 Numerical simulations

A generalized model describing the OSL signal from Al_2O_3:C was introduced in section 2.3 together with the rate equations describing the charge transitions in the crystal (eq. (2.11)-(2.15)). Temperature effects on the OSL signal in the room to body temperature region was investigated by considering two possible thermal mechanisms. The first is shallow traps characterized by the temperature relevant parameters s_1 and E_1 in equation (2.11). The second mechanisms is thermal excitation from an optically excited state of the main dosimetry trap. This mechanism is characterized by the asterix parameters in figure 2.5 and is just referred to as "thermal excitation" in the following.

Thermal quenching is understood as the loss of luminescence efficiency with increasing temperature and can be understood from a Mott-Seitz mechanism [59]. The radiative luminescence intensity, L, can be written as

$$L = \frac{L_0}{1 + \tau_0 \nu \exp(-W/kT)} \tag{4.3}$$

where L_0 is the unquenched intensity at low temperatures, τ_0 is the lifetime for radiative transitions, W is the activation energy and ν is a constant frequency factor. W is the thermal energy needed for an electron in the excited state of a luminescence center (F^* in Al_2O_3:C) to make a non-radiative transition to the ground state [1]. Akselrod et et al. found the values of the activation energy and frequency factor for Al_2O_3:C to be about 1.06 eV and 10^{14} s^{-1} respectively [8, 5]. With τ_0 =35 ms the dimensionless constant $\tau_0\nu$ is equal to $3.6{\cdot}10^{12}$. Here, we are mainly concerned with temperatures around

body temperature. The reduction in luminescence efficiency at say 40 °C using the above values is of the order 10^{-6} and therefore not relevant for the temperature study.

A program using a 4th order Runge–Kutta procedure together with an adaptive stepsize control was developed to solve the rate equations and simulate the effect of changing the temperature in the room to body temperature region (see appendix B.1). Thermal excitation was simulated with the program "RATE" previously used to solve the rate equations [62, 1]. The model is not an attempt to accurately reproduce the detailed quantitative behavior of the crystal. It is rather a tool to test whether the suggested thermal mechanisms can qualitatively reproduce some mean characteristics of crystal behavior. All simulations were subject to the following protocol at a given temperature: irradiation (100 seconds) → relaxation (100 seconds) → optical stimulation (600 seconds). An example of such a protocol is shown in appendix B.1.2.

4.3.1 Afterglow simulation

A clear indication of the presence of shallow traps in a crystal can be seen immediately after the irradiation ends. At this point, no electron–hole pairs are produced and the shallow traps empty the trapped charge into the conduction band because of their thermal instability. This results in a decaying luminescence signal termed afterglow (phosphorescence) as shown in figure 4.8A. When the temperature increases charge is released faster from the shallow traps and the afterglow decays faster. Since focus is on thermal mechanisms, model parameters were adjusted to imitate the shallow trap behavior most accurately and figure 4.8B shows the afterglow (relaxation) simulated at different temperatures. Parameter values for the charge transitions are given in the figure caption.

4.3.2 OSL simulation

Figure 4.9 shows the simulated OSL responses. The data displayed in the left panels are obtained on the basis of a shallow trap model with no thermal excitation. The curves in the right panels were produced using a thermal excitation model containing no shallow traps. The difference in input parameters using the two models are given in the figure caption.

Figure 4.9A displays OSL curves at different temperatures using the shallow trap and thermal excitation model. Both phenomena can explain the initial increase of the OSL curve with increasing irradiation and stimulation

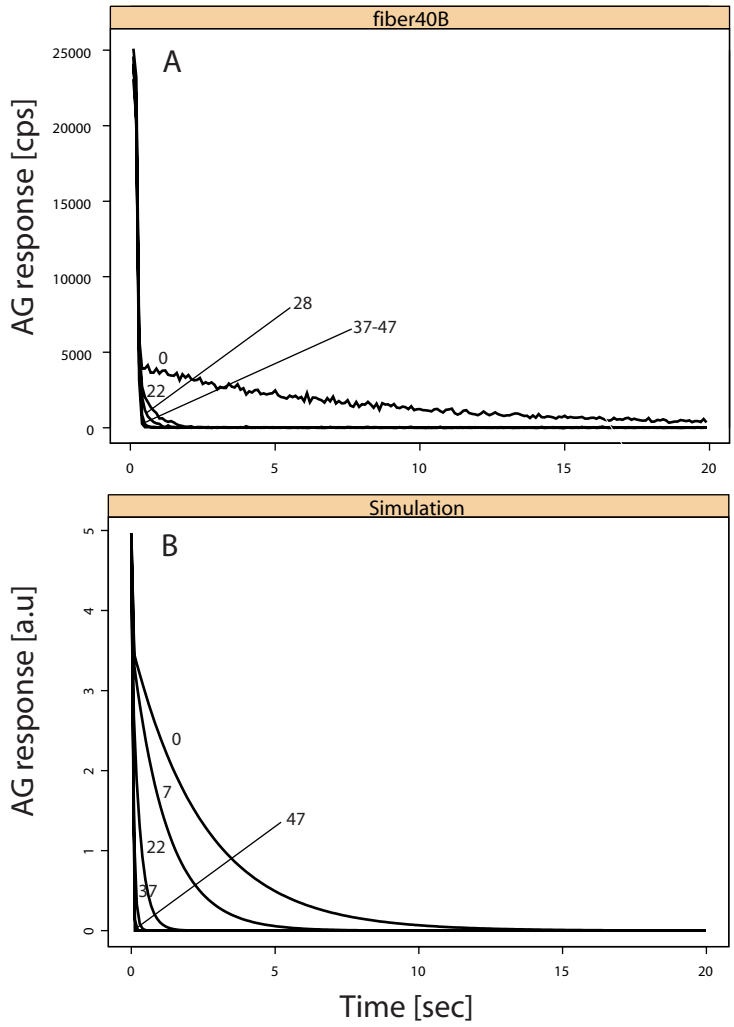

Figure 4.8: Afterglow (AG) vs. time at different temperatures for **A** fiber40B (TLD-500) and **B** the model. The numbers in the figure indicate temperatures in ^{o}C. The model parameters as shown in figure 2.5 were $N_1 = 5.5 \cdot 10^{12}$ cm^{-3}; $N_2 = N_3 = 10^{12}$ cm^{-3}; $M_4 = M_5 = 5 \cdot 10^{12}$ cm^{-3}; $m_0 = 10^{10}$ cm^{-3}; $E_1 = 0.7$ eV; $E_2 = 1.5$ eV; $E_3 = 3$ eV; $s_1 = 10^{13}$ s^{-1}; $s_2 = s_3 = 10^{12}$ s^{-1}; $A_1 = A_2 = A_3 = A_4 = A_5 = A_{m5} = 10^{-10}$ cm^{-3}s^{-1}; $A_{m4} = 10^{-9}$ cm^{-3}s^{-1}; $R = 10^{7}$ cm^{-3}s^{-1} and $f_2 = 0.1$ s^{-1}.

temperature. For the shallow trap model a delayed peak is seen at intermediate temperatures which is absent in the thermal excitation model. As the temperature increases the charge captured either by shallow traps or the intermediate energy level of the main dosimetry trap is immediately released into the conduction band and both phenomena loose their influence on the

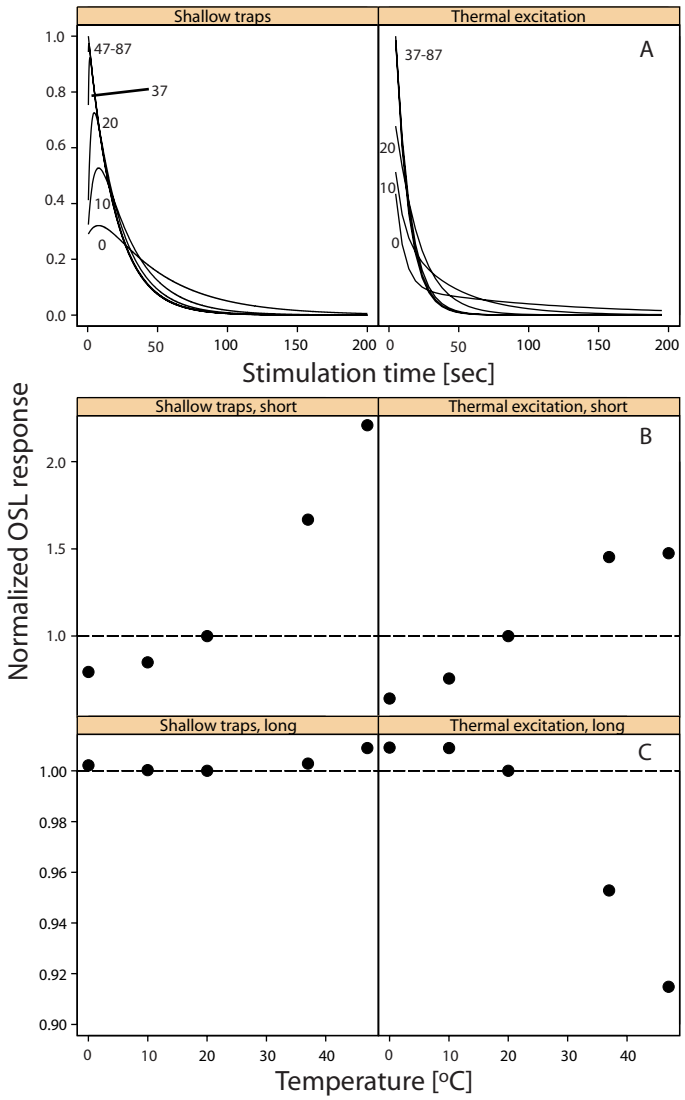

Figure 4.9: Simulated OSL response from the two models. **A** OSL curves at different temperatures for the shallow trap (left) and thermal excitation (right) model. The numbers in the figure indicate temperature in ^{o}C. **B** Integrated values for short and **C** long integration times. Shallow traps: short=0.5 seconds and long=600 seconds. Thermal excitation: short=0.1 seconds and long=600 seconds. Shallow trap parameters are the same as in fig. 4.8. Thermal excitation parameters are indicated by asterisk in figure 2.5. Here N_1=0, $s_2^* = 10^{12}$ s^{-1}, $f_2^* = f_2^{**} = 0.1$ s^{-1} and $E_2^* = 0.75$ eV and all other parameters are the same as in figure 4.8.

OSL signal. At high temperatures shallow traps and thermal excitation can be totally disregarded.

Figures 4.9B and C show the integrated values of the simulated OSL curves at short (upper panel) and long integration times (lower panel), respectively. The specific integration times for the two models are given in the figure caption. At short integration times, the OSL signal is increasing with temperature for both models. This should come as no surprise considering the initial increase in the OSL behavior in figure 4.9A. At long integration times, the OSL signal is decreasing with temperature for the thermal excitation model while an increase, although highly reduced, can still be detected in the shallow trap model.

4.4 Discussion of temperature effects

Previously published data [58, 65, 22] on the temperature effects of Al_2O_3:C have focused on short OSL stimulation times (<1 second) or read out during increasing temperatures (TL glow curves, i.e. non-isothermal stimulation). From these data, the OSL response always increases with stimulation temperature. The presented temperature data quantify the temperature effect on both RL and OSL for conditions more relevant for the general application of Al_2O_3:C in medical dosimetry. The OSL response does not always increase with stimulation temperature.

According to figures 4.3 and 4.5 and table 4.3, the integrated OSL and RL signals are changing between -0.2 to 0.6 % per ^{o}C for the samples investigated. This interval indicates the correction factor one must take into account when performing luminescence dosimetry at different temperatures. Figures 4.3, 4.4 and 4.5 show that the OSL response depends on both irradiation and stimulation temperature whereas the RL response only depends on irradiation temperature.

For constant irradiation temperature, we found that the influence of any variation in stimulation temperature on the OSL signal can be eliminated by choosing an appropriate OSL integration time. Changing the stimulation temperature has no effect on the subsequent RL response which is clear from figure 4.4. When the irradiation temperature is varied it is not possible to eliminate the temperature effect on the OSL signal by adjusting the integration time. The effect can, however, be reduced for most crystals by increasing the integration time. This is apparent from table 4.3. On the basis of these observations we recommend that the calibration and the measuring process are carried out at the same irradiation temperature (i.e. at body temperature for *in-vivo* measurements) whereas the stimulation temperature is less critical since this effect can be eliminated by integration. This means that the OSL readout could be carried out outside the patient after irradiation.

The mechanisms causing the temperature dependence in the simulations were shallow traps and thermal excitation. The simulation protocol in figure 4.9 is identical to the protocol used in the "Reader", "Block" and "Peltier" experiments (table 4.3), i.e. irradiation and stimulation at the same temperature. The variation in OSL with integration time and temperature (see figure 4.9) is consistent with a shallow trap model but not with the thermal excitation model. In our model, thermal excitation has no influence on the irradiation part since the intermediate energy level has no trapping probability. In figure 4.3, only the stimulation temperature is varied. Therefore, one might expect that the effect of thermal excitation would be more pronounced in this experiment than the experiments contained in table 4.3. The key feature of thermal excitation as modeled in figure 4.9 is the ability to reverse the temperature effect on OSL from an increase at short integration times to a decrease at long integration times. As this is in fact the observation in figure 4.3, we suggest that thermal excitation dominates the temperature effect of the stimulation process. When irradiation temperature is constant and stimulation temperature is varied, it seems that the influence of shallow traps is reduced while the influence of thermal excitation is enhanced.

All OSL decay curves obtained showed initial increase with temperature. Both shallow traps and thermal excitation could explain this behavior up to a temperature where they loose their influence. Since the energy depths in real crystals are distributions rather than discrete levels, this could explain the increase in OSL peak values at all temperatures. When one shallow trap level is emptied at a given temperature, traps in the higher energy part of the distribution takes over. Similar, several thermal excitation levels could be present in different traps.

Figure 4.10 shows some key features associated with temperature effects. In figure 4.10A, the initial OSL signal is increasing with temperature. Moreover, at intermediate temperatures a delayed peak (at $\sim$ 1 second) is present which vanishes at low and high temperatures. This behavior has been suggested to be caused by shallow traps and this was demonstrated theoretically in figure 4.9A. Figure 4.10B shows a normalized OSL response and here the decay rate is changing significantly with temperature. This change is usually ascribed to thermal excitation [22]. Figure 4.10C shows the tail of the OSL curve in the "Room/Body" experiment. The crystal is harder to bleach at 41 ^{o}C than at 25 ^{o}C. This effect is probably due to changes in retrapping probability with temperature.

Shallow traps and thermal excitation can coexist and one or the other process may be dominating depending on the concentration of shallow traps and the degree of thermal excitation. If the stimulation rate during cw-OSL is strong compared to the concentration of shallow traps, the characteristics

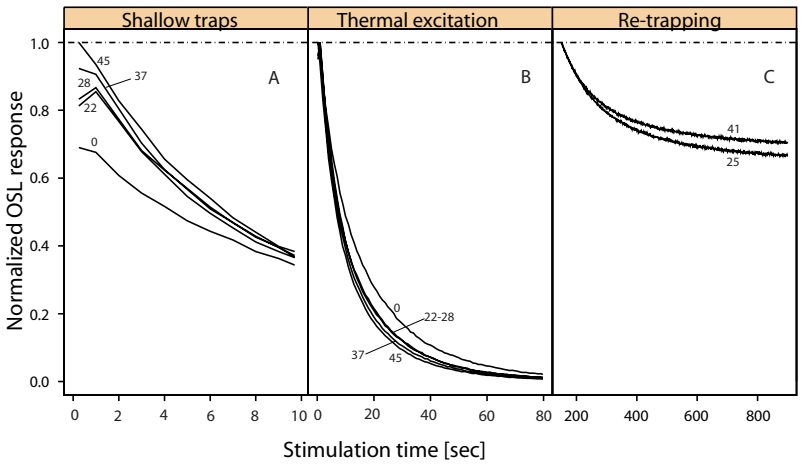

Figure 4.10: Key features associated with temperature effects. Numbers indicate temperature in ^{o}C. **A** First 10 seconds of the OSL curve for fiber40B in the "Block" experiment. A delayed peak is observed around 1 second for intermediate temperatures. **B** First 80 seconds of normalized OSL response for fiber40B. **C** Last 600 seconds of the OSL curve (tail) from fiber43 in combination 1 and 3 in the "Room/body" experiment.

of shallow traps can not be observed as demonstrated by McKeever et al. [65]. The decay rate is expected to be unaffected by temperature when shallow traps are present. On the other hand, thermal excitation processes are expected to affect the OSL decay rate, τ, significantly with temperature as

$$\tau(T) = \tau_0 \exp(-\frac{\Delta E}{kT}) \tag{4.4}$$

where ΔE is the thermal activation energy [22]. ΔE is the energy difference between the excited trap state and the conduction band (E_2^* in fig. 2.5). Thus, fiber40B in figure 4.10B seems to be under the influence of thermal excitation. Since fiber40B also showed behavior of shallow traps in figure 4.10A, this crystal must include both mechanisms.

4.5 Conclusions on temperature effects

Several aspects of temperature influence on the luminescence output from Al_2O_3:C were investigated. We have shown that the OSL response changes with both irradiation and stimulation temperature as well as OSL integration time. The RL response only depends on irradiation temperature.

We conclude that temperature effects on the OSL response can be eliminated by integration if irradiation temperature is not varied. In this sense,

variations with stimulation temperature are less critical than the irradiation temperature, and we recommend that calibration and measurement are carried out at the same irradiation temperature (i.e. at body temperature for *in-vivo* measurements).

The overall change in the integrated OSL and RL signal with irradiation and stimulation temperature lies between -0.2 to 0.6% per ^{o}C. This interval indicates the correction factor one must apply when performing luminescence dosimetry at different temperatures.

The OSL peak increases with increasing temperature. Also, the OSL signal decays faster at higher temperatures and values for this feature are presented in table 4.4. Numerical simulations suggest that the qualitative behavior of OSL with temperature is a result of the combined effects of shallow traps and thermal excitation. The effects of shallow traps can be reduced by choosing a constant irradiation temperature.

Although different crystal growths, test doses, stimulation light and detection windows were used, the same overall effects were observed. Therefore, the reported temperature dependence seems to be a general property of Al_2O_3:C.

5 Proton energy effects

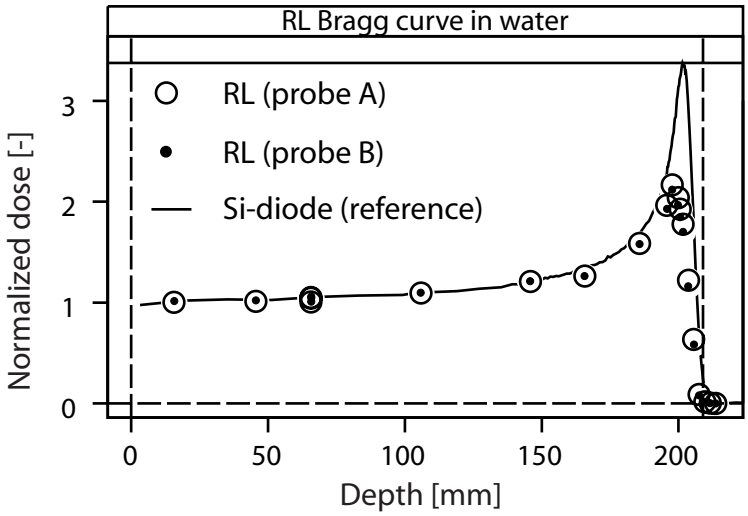

Figure 5.1: Two Al_2O_3:C probes (CZ#60 growths) named probe A and B irradiated with 175 MeV protons in a water tank. The probes were positioned at different depths and the integrated RL signals are shown together with a reference Si-diode known to give the correct dose-response. It should be noted that the RL data are corrected for sensitivity changes. The maximum of the RL profiles is about 60% of the maximum obtained by the reference diode. The data are taken from [12].

The energy of protons can be adjusted such that most dose is deposited in a tumor deep inside the body while the dose to the surrounding healthy tissue is reduced compared to radiotherapy with high-energy X-rays. This possibility provides an advantage for proton radiotherapy over conventional radiotherapy. Figure 5.1 shows how protons deposit dose at different depths in water. This is the so–called Bragg curve with a maximum of energy being deposited in the Bragg peak. Figure 5.1 is equivalent to a clinical situation

where the energy is selected such that the Bragg peak coincide with a tumor at about 20 cm depth[1].

The origin of the Bragg curve is that the linear energy transfer (LET) of heavy charged particles (HCPs) changes with energy of the HCPs as seen in figure 5.2. As the energy of the protons decreases, i.e. the protons are slowed down at greater depths, the LET of the protons increases, i.e. more energy is being deposited in the material. The change in LET depends on the type of HCP, here protons, the energy of the HCP and the target material.

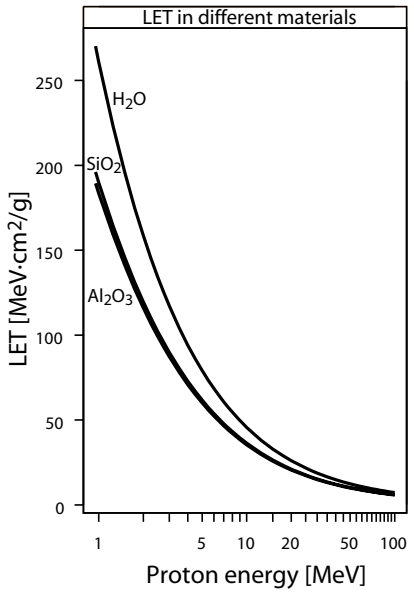

Figure 5.2: LET vs. energy for protons in the three different materials indicated in the figure. The LET increases with decreasing energy, i.e. more energy is depoisted in the material with low energy protons compared to high energy protons, and depends on the target material. The data are taken from the national institute of standards and technology in USA (NIST) [47].

Like most luminescence detectors, the integrated RL response from Al_2O_3:C in figure 5.1 underestimates the dose in the Bragg peak, where the LET of the protons is high, compared to the Si-diode reference and a similar under-response in the OSL signal is also observed. In order to use Al_2O_3:C as a proton dosimeter, an important issue is therefore to characterize both the RL and OSL response with respect to LET for correct dosimetry. In this chapter, attention is given to the LET dependence of the OSL signal.

[1] A treatment depth of 20 cm is rather unrealistic given the dimensions of a human why patients are treated with lower proton energies.

Yukihara et al. studied the change in OSL decay rate with increasing β-dose and increasing ionization density (LET) at a low dose (see fig. 5.3) [95]. It was proposed that the dependence of the OSL decay rate on dose is

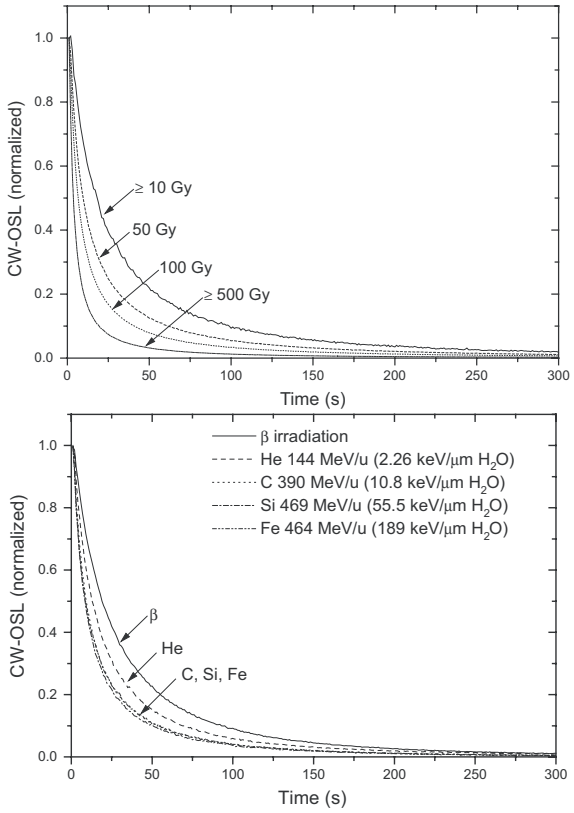

Figure 5.3: Normalized cw-OSL decay curves from Luxel^{TM} Al_2O_3:C dosimeters given by Yukihara et al. [95]. Upper: Dosimeters exposed to β-irradiation with a ^{90}Sr source. Numbers indicate the dose given in Gy. Lower: Dosimeters given a dose of 0.1 Gy with different ionization densities (LET) as indicated in the figure.

connected to the dependence of the OSL decay rate on ionization density. We explore this connection in more detail since this is basically the idea of track structure theory (TST) where saturation doses around the track of the HCP is responsible for the decrease in response with increasing ionization density. Figure 5.4 shows the dose dependence on the OSL decay rate of two Al_2O_3:C probes at two different ionization densities. The OSL decay curves follow the trends from fig. 5.3 but the increase in OSL decay rate (faster decay) is more pronounced at 60 MeV compared to 10 MeV, i.e. is more pronounced at lower ionization densities than higher. Figure 5.5 shows the OSL decay rate for different ionization densities at three different doses. At low doses,

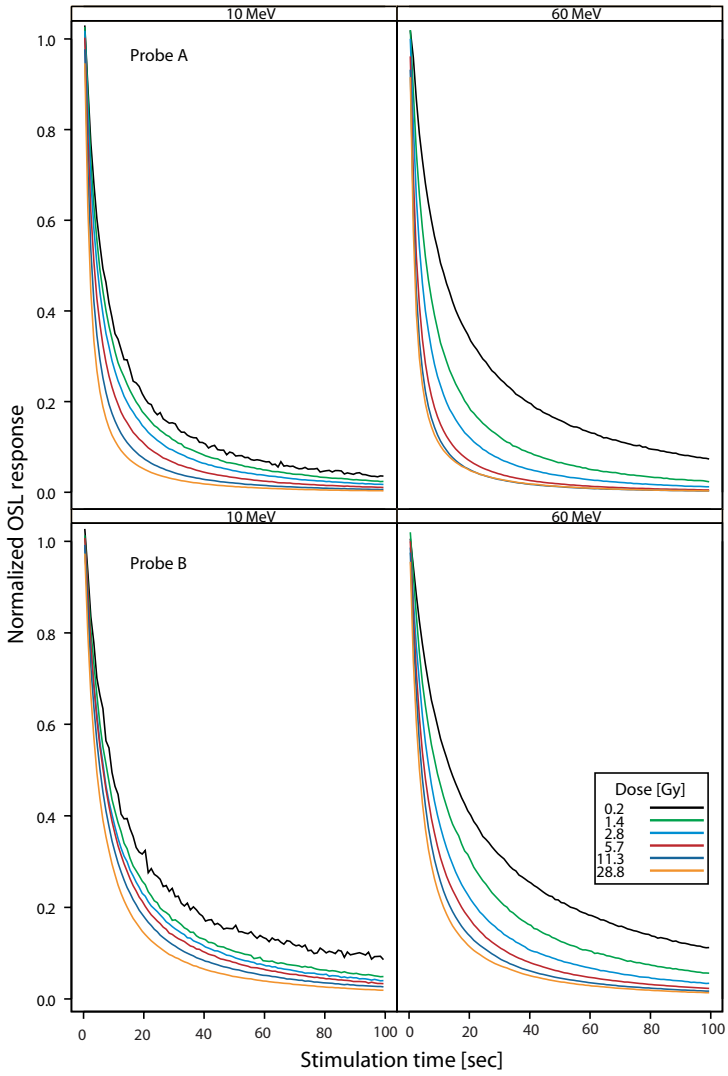

Figure 5.4: Normalized cw-OSL decay curves from probe A and B (see section 5.1). OSL decay at different doses for 10 MeV protons (left) and 60 MeV protons (right).

we see the same behavior in the OSL decay as in fig. 5.3. Since the decay rate is the result of the combined effects of both dose and ionization density, however, the OSL signals decay differently as the dose is increased.

An UV–luminescence center in Al_2O_3:C was recently reported to depend differently on LET compared to the normally reported F-center when the total integrated OSL signal is used [97]. Here, we focus on the F-center luminescence and look at both the initial OSL signal and the total OSL signal. This approach is taken due to the behaviour of the OSL decay rate

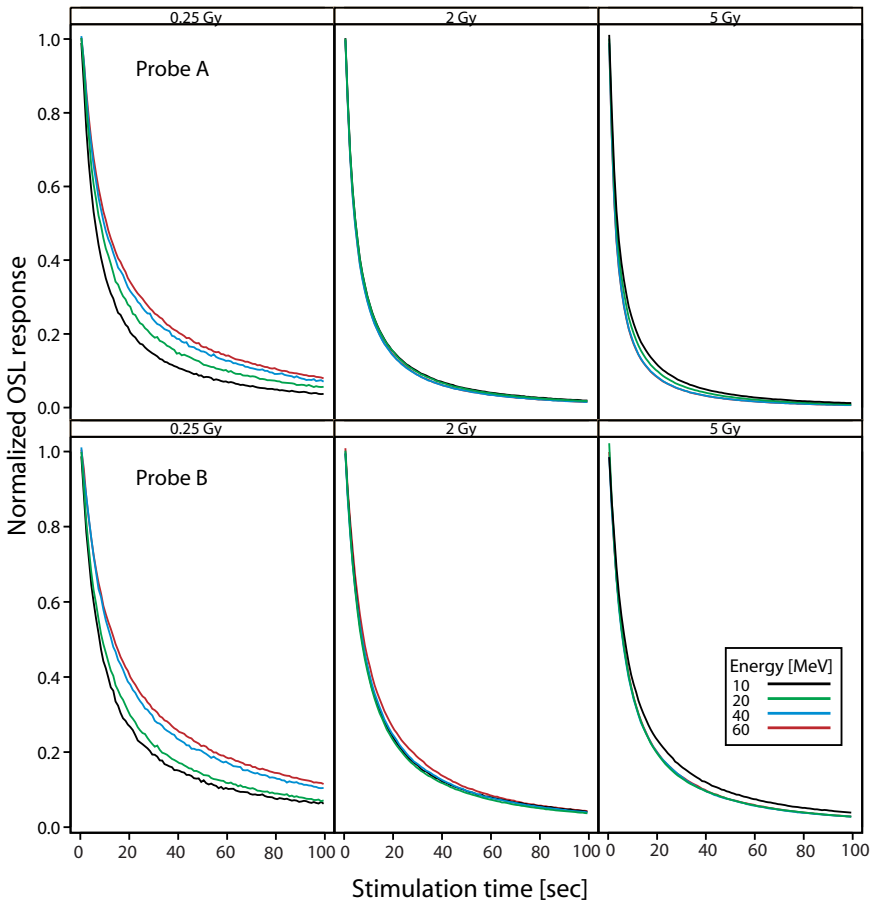

Figure 5.5: Normalized cw-OSL decay curves from probe A and B at different proton energies for three different doses: 0.25 Gy (left), 2 Gy (center) and 5 Gy (right).

with dose and ionization energy. The OSL decay curve is known to consist of a number of components (see eq. (2.20)) [8] but the initial OSL signal captures a single (fast) decay component whereas the total OSL signal captures the sum of all decay components. In this way, we investigate two extreme cases of the OSL signal similar to the approach chosen in the temperature study.

The objective of this chapter is to use the multi-hit target and track structure theory introduced in sections 2.4 and 2.5 to gain insight into the physics underlying the OSL proton response and investigate the change in response with LET. On this basis, we can better assess the general applicability of Al_2O_3:C as a potential dosimeter for proton dosimetry. We will follow an approach which is similar to the one used to describe the TL response of peak 5 and 6 in LiF to HCP-irradiation [90].

5.1 Materials and methods

We used a prototype system in which the Al_2O_3:C crystal is attached to an optical PMMA fiber cable [10]. Stimulation was performed using a green (532 nm, 20 mW) laser and the OSL and RL signal were detected with a bialkali photomultiplier tube (PMT) and a band–pass filter (395 to 440 nm). After irradiation, the laser was switched on and a continuous wave OSL (cw-OSL) decay curve was recorded as a function of stimulation time. The "peak OSL signal" is found by extrapolating the OSL decay curve to 0 s, and the "total OSL signal" is obtained by integrating the OSL decay curve from 0 to 500 s.

Two fibres attached Al_2O_3:C crystals, referred to as probe A and B, were used. Probe A is a $2\times0.5\times0.5$ mm^3 Al_2O_3:C crystal grown by Landauer Inc. using the Czochralksi technique (growth CZ#60). Probe B is a $2\times1\times0.8$ mm^3 cut from a Al_2O_3:C single crystal commonly known as TLD-500 [6].

Proton irradiations of probe A and B were performed at the Paul Scherrer institute (PSI)in Switzerland with energies in the interval 10-60 MeV (LET between 4.57-1.08 keV/μm in water). The probes were positioned in the beam such that the crystal thickness in the beam direction was 0.5 mm for probe A and 1 mm for probe B. The different proton energies were obtained by inserting aluminum degraders of varying thickness in the beam line (see figures 5.6 and 5.7). The quoted energies represent the peak values of the energy spectra generated by the degraders (see figure 5.7). The γ-irradiations were carried out for probe A and B with a ^{137}Cs source at the Risø National Laboratory in Denmark. The proton- and γ-doses are given in Al_2O_3 whereas the LET-values of the proton beam are given in water to ease comparison with existing literature. For the track structure calculations, the LET-values of the beam were transferred to Al_2O_3 as tabulated by NIST to obtain target estimates in this material [47].

Here, we define the relative efficiency, η, as the detector response at a given proton energy normalized by the response for 60 MeV protons (LET = 1.08 keV/μm in water). For practical reasons, it was necessary to detach the fiber probes between the γ and proton experiments. The exact coupling efficiency between fiber and instrument (i.e. how much luminescence that reach the photomultiplier tube) can change by more than 10% each time a fiber cable is detached and reattached. Hence, the benefit of calculating the efficiencies relative to the 60 MeV proton response (and not the γ-response) is therefore that all proton results were acquired with exactly the same set-up. Since the response to 60 MeV protons and γ-rays are expected to the

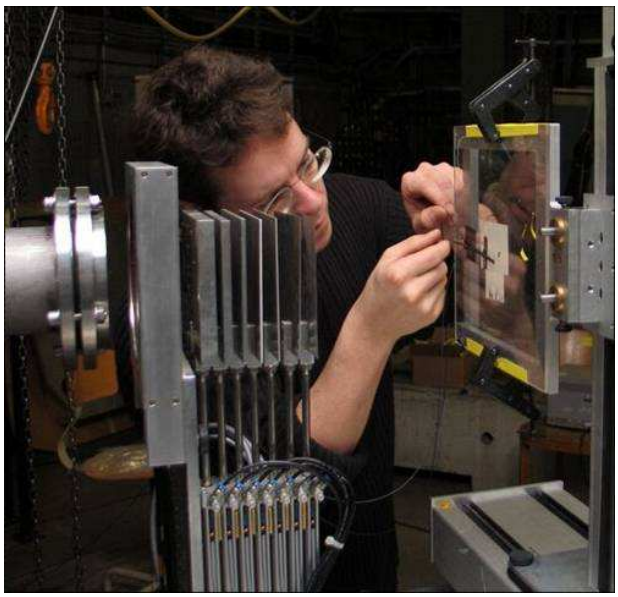

Figure 5.6: Photo of the experimental setup at PSI. The proton beam enters from left through a collimator and an ionization chamber with an initial homogeneous energy around 65 MeV. As the beam passes through the degraders, the proton energy is reduced and broadened. In the picture, the author is monitoring fibers A and B on a plastic holder such that the beam hits the crystal probes as shown in the cross-sectional view of figure 5.13.

same at low doses [85, 97], the η-values reported here can be compared with values given in the literature[2].

5.1.1 Track structure calculations

Figure 5.8 shows the dose–response curves obtained with γ-irradiation for probes A and B. For each probe, a dose–response curve is obtained for both the peak and total OSL signal. Fitting eq. (2.30) to the dose-response curves of the Al_2O_3:C probes for the γ-irradiation provides us with the parameters R, E_1, E_2 and OSL_γ^{max}. Using E_2 in equation (2.36) with $c = 2$ for a range of energies and target radius values in Al_2O_3 provides us with the parameters κ and σ_0 (see appendix A.2). From these parameters, R, E_1, E_2, OSL_γ^{max}, κ and σ_0, we can calculate the dosimeter response, OSL_p, to proton irradiation at dose D with eq. (2.43) for a given target radius, a_0, which is here considered a free parameter chosen to fit data most accurately.

[2]We found the relative OSL response, i.e. the response unaffected by the absolute luminescence output, to γ-rays and 60 MeV protons to be identical.

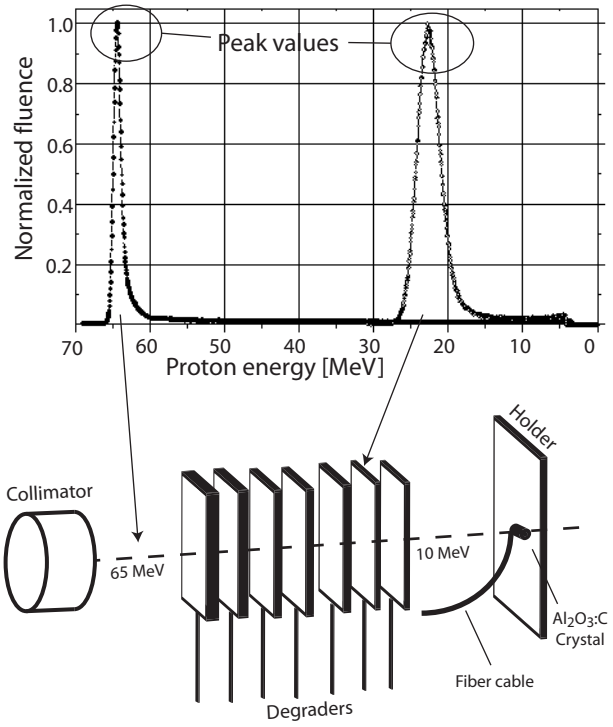

Figure 5.7: Schematics of the experimental setup at PSI as shown in figure 5.6. The energy spectra show the broadening of the energies as the protons are slowed down by the degraders. The energy spectra are shown at 65 and 23 MeV and the peak values indicated are used to represent the whole spectrum by one (average) energy.

Applying TST to experiments

The key equation for the TST calculations is eq. (2.43). Calculations based on this equation, however, only apply to an infinitively thin dosimeter where the energy of the penetrating protons do not change. When the calculations are compared to experimental data, we have to take the finite dosimeter thickness into account. Therefore, we subdivide the dosimeter into slabs where the energy of the proton is approximatively constant and eq. (2.43) can be applied with reasonable justification. We have chosen "approximatively constant" to mean that the energy does not vary more than 5% within each slab (see fig. 5.9 and function "`Ez.account.1`" in appendix B.2.2).

The proton fluence ϕ is considered constant through the detector until the protons stops and we ignore the production of secondary protons and energy straggling such that the protons in slab i have the same energy E_i. We then calculate the response $OSL_{p,i}(D_i)$ for slab i receiving the dose $D_i = \phi LET_i$ where LET_i is the LET corresponding to the energy E_i in the detector

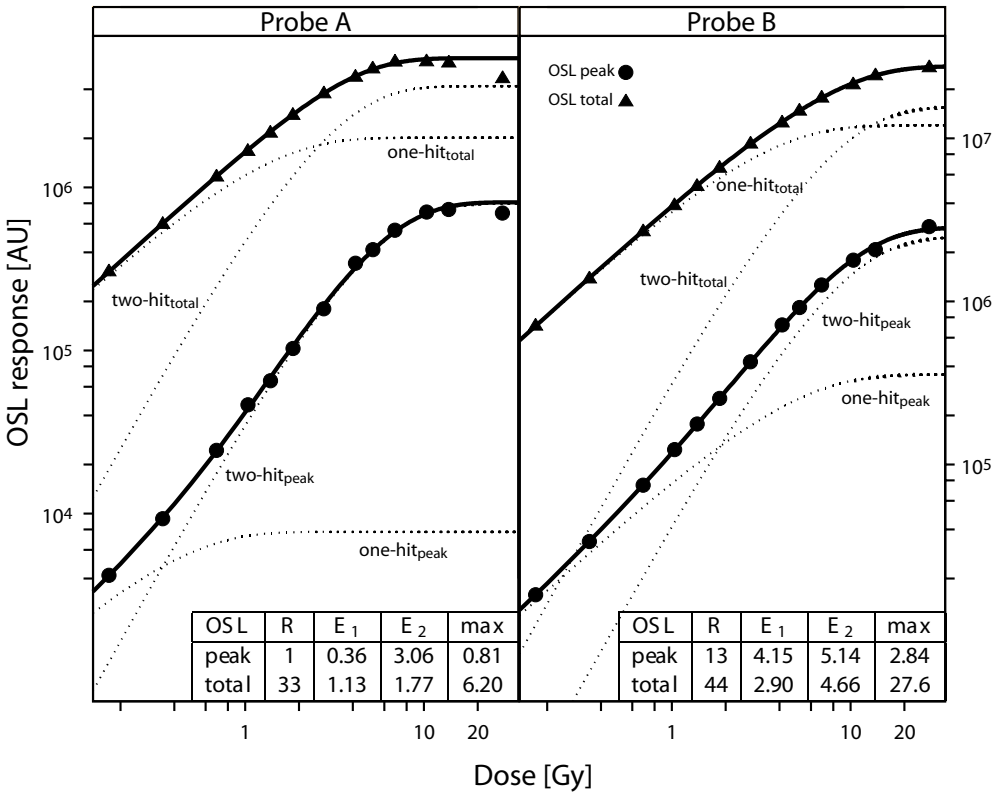

Figure 5.8: Parameterizations of the peak and total OSL dose-response from γ-irradiation of probes A and B. Each component in eq. (2.30) is indicated by dotted lines for the two OSL signals used. R is the relative contribution of the one-hit component in % and E_1 and E_2 are the characteristic dose in Al_2O_3 for each component in Gy. max is the maximum value OSL_γ^{max} in 10^6 counts. Declining points after saturation are not included in the fit for probe A.

material (Al_2O_3) . The sum of the responses from all slabs then gives the total proton response from the probe. If the probe has a mass of M and slab i has the mass m_i, $OSL_{p,i}(D_i)$ has to be scaled with m_i/M. The calculated proton response from a probe with mass M is then

$$OSL_{exp} = \sum_{i=1}^{N} \frac{m_i}{M} OSL_{p,i}(D_i) \tag{5.1}$$

The principle of the calculation is illustrated in fig. 5.9.

As described in section 5.1, the experimentally obtained relative efficiency, η, is given as the detector response at a specific proton energy, normalized by the response for 60 MeV protons (LET = 1.08 keV/μm in water). Hence, the calculated efficiency to be compared with the experimental ones is given

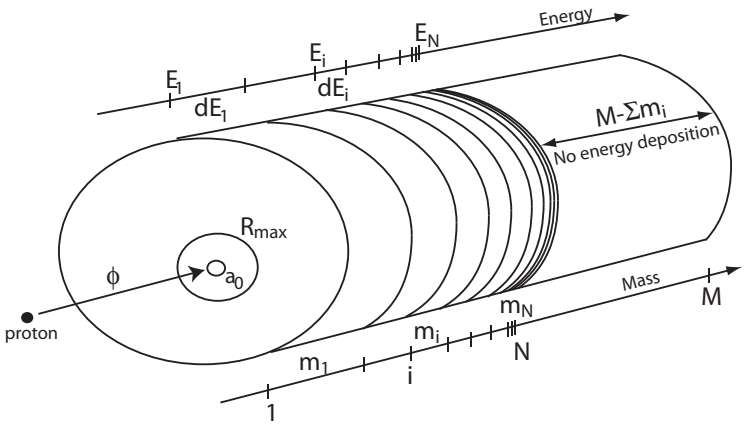

Figure 5.9: Principle of the calculations in eq. (5.1). Subscripts on the energy and mass axis indicate slab number. The energy varies 5% in a slab, i.e. $E_{i+1} = 0.95E_i$. The dose given to the dosimeter is characterized by the fluence ϕ and the response for each slab is calculated from a radial dose distribution with a centrally placed target. The target is characterized by the radius a_0 and the δ-rays in the track have a maximum distance of R_{max} (see function in "`delta.max`" appendix B.2.2). The response from slab i is scaled with m_i/M. The figure shows a situation where the protons come to a complete stop inside the dosimeter.

by

$$\eta = \frac{OSL_{exp}(x \text{ MeV})}{OSL_{exp}(60 \text{ MeV})} \tag{5.2}$$

where x is a proton energy equal to or less than 60 MeV and η is obtained at a given dose $D_{init} = \phi LET_{init}$. ϕ is the fluence and LET_{init} is the LET in Al_2O_3 of the incoming protons before they hit the probe and $D^x_{init} = D^{60}_{init}$.

5.2 Results

5.2.1 Estimating a_0

Varying a_0 will change the two dose distributions D_{LEM} and D_{Site} shown in figure 2.9 in order to keep the area under the curves constant, i.e. to keep the total energy deposition equal to the LET. This change will enter in eq. (2.36) and therefore effect the OSL response in eq. (2.43) and consequently eq. (5.1). Figure 5.10 shows a model calculation of $f(D)$ (see eq. (2.34)) and η for a_0=50, 95 and 150 nm. Increasing a_0 will systematically increase both $f(D)$ and η and by inspection we select a_0 such that the calculated responses mimic the experimental behavior of both quantities most accurately. This

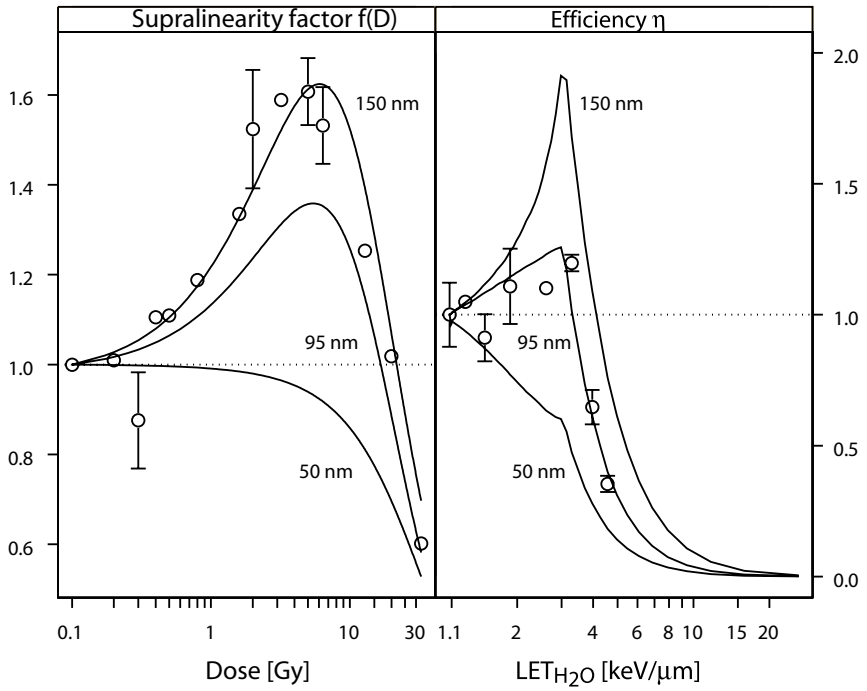

Figure 5.10: Illustration of the procedure by which a_0 is determined. Open circles are the experimental peak OSL signal from probe B for $f(D)$ at 60 MeV (left) and η at 0.3 Gy (right). The model calculations are made with D_{Site} and shown by full lines. The values of a_0 is indicated by numbers in the figure.

illustrates the uncertainty by which a_0 was estimated. We can narrow down the interval of a_0 but not determine it exactly. From both $f(D)$ and η in figure 5.10, we found that $a_0 = 95$ nm although 150 nm is a better choice if $f(D)$ is considered alone.

5.2.2 Supralinearity

Figure 5.11 shows the supralinearity factor $f(D)$ for experimental and calculated values using D_{LEM}. $f(D)$ is plotted versus dose for the two probes A and B using the peak and total OSL signal. Figure 5.12 is identical with figure 5.11 but here D_{Site} is used in the model calculations. In both figures, a systematic decrease with increasing LET is seen in the experimental data for the peak OSL signal (upper panels). The total OSL signal shows a sigmoid sublinear behavior with the 10 MeV response crossing that of the 60 MeV and γ-response at about 5 Gy (lower panels).

The model calculations are shown for 10 and 60 MeV protons with dashed and full lines, respectively. The systematic decrease in supralinearity with

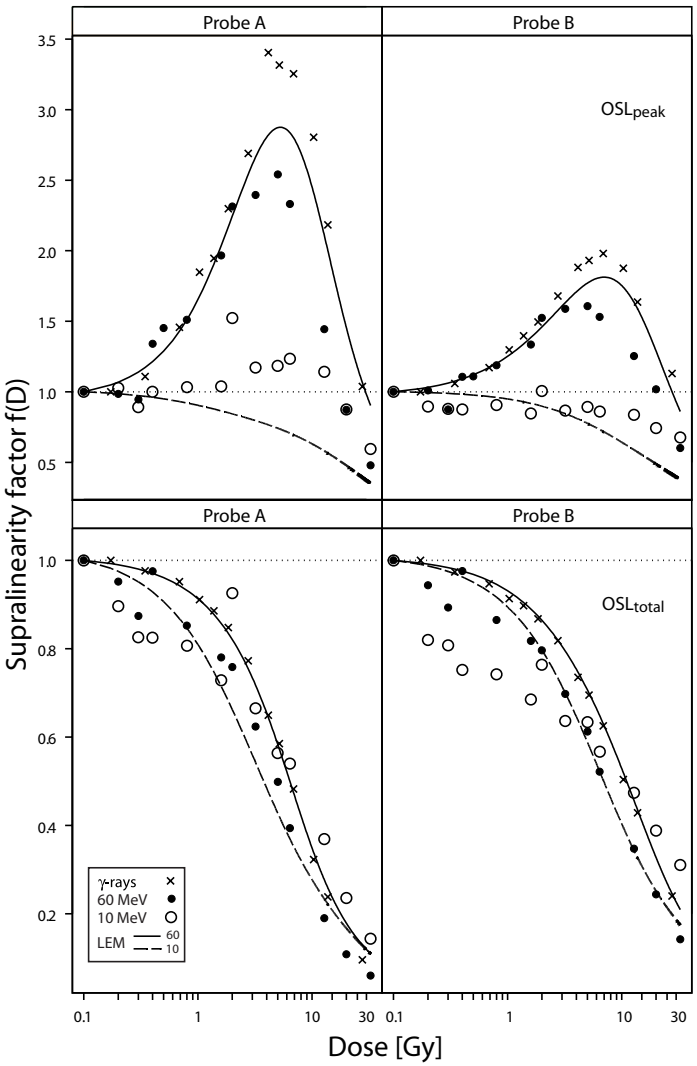

Figure 5.11: The supralinearity factor $f(D)$ defined in eq. (2.34). The model calculations are shown with full and dashed lines and made with D_{LEM} in eq. (5.1) for 10 and 60 MeV protons in Al_2O_3. Experimental data are shown for γ-rays and 60 and 10 MeV protons. The upper panels show the peak OSL signal and the lower panels show the total OSL signal.

increasing LET of the peak OSL signal is captured by the model for both D_{LEM} and D_{Site}. In figure 5.11, D_{LEM} overestimates the 60 MeV reponse and underestimate the 10 MeV response for probe A while a better fit is made with probe B. In figure 5.12, D_{Site} underestimates the peak OSL signal for both 60 and 10 MeV protons for probe A while a better fit is also made for probe B. D_{LEM} seems to fit the data best for low doses while D_{Site} fits

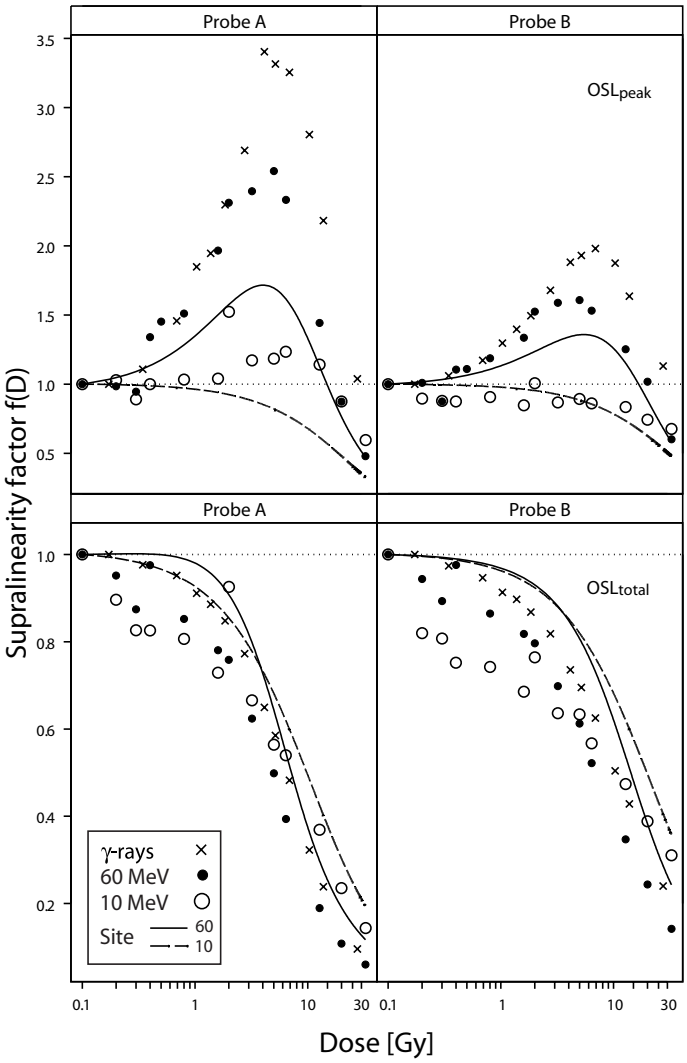

Figure 5.12: Identical with figure 5.11 using D_{Site} in the model calculations. The notation in all panels is the same as in figure 5.11.

data best for higher doses. The difference between model and experimental data for the OSL peak signal from probe A could be due to an insufficient parameterization of the γ-response in fig. 5.8. After saturation, the signal starts declining at larger doses and this feature is not included in the model. This decline in the OSL response from Al_2O_3:C is well known and decreases further with increasing dose [98].

The sublinear sigmoid behaviour of the total OSL signal is also predicted by the model. Using D_{LEM} in the model calculations in figure 5.11, both the

10 and 60 MeV calculated response reproduce the behavior of the experimental data reasonably well although an initial decline at low doses is not well fitted. The 10 MeV curve is at all times on the left side of the 60 MeV curve so calculations with D_{LEM} do not capture the crossing of the 10 and 60 MeV response. For the D_{site} distribution in figure 5.12, the model calculations of the total OSL signal do not fit data as well as D_{LEM}. However, using D_{Site} in the model calculations capture the crossing of the 10 and 60 MeV response.

5.2.3 Relative efficiency

Figures 5.14 and 5.15 show the relative efficiency for probe A and B. The calculations are made with D_{LEM} for the peak and total OSL signal in fig. 5.14 and D_{Site} in fig. 5.15. The experimentally obtained efficiency of the peak OSL signal of probe A displays an almost flat behavior independent of LET for the 0.3 Gy panel whereafter it decreases with LET as the dose increases. Probe B shows the same behavior as probe A although the efficiency decreases at lower LET-values in all panels even when the dose is 0.3 Gy. This is because of the larger dosimeter thickness (1 mm) causing protons with lower LET to come to a complete stop within the probe compared to probe A (0.5 mm) as demonstrated by the GEANT4 simulation in figure 5.13.

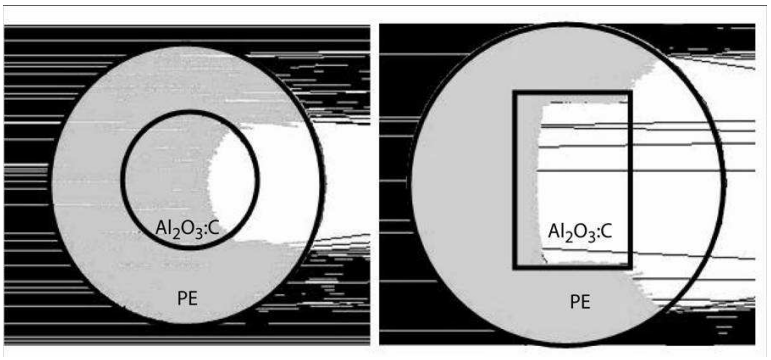

Figure 5.13: A cross-sectional view of a GEANT4 simulation of 10 MeV protons in probe A and B. The protons enters the geometries of probe A (left) and probe B (right) from the left. In the simulation, the Al_2O_3:C crystals are covered with polyethylene (PE). Black areas: protons, dark gray areas: energy deposition, light gray areas: no energy deposition. The simulation was kindly provided by Gabriel Sawakuchi, Oklahoma State University (USA), 2006.

The model calculations accounts for the main features of the experimental data. For the peak OSL signal, efficiency decreases with dose whereas it is unchanged or increases slightly for the total OSL signal. Overall, the

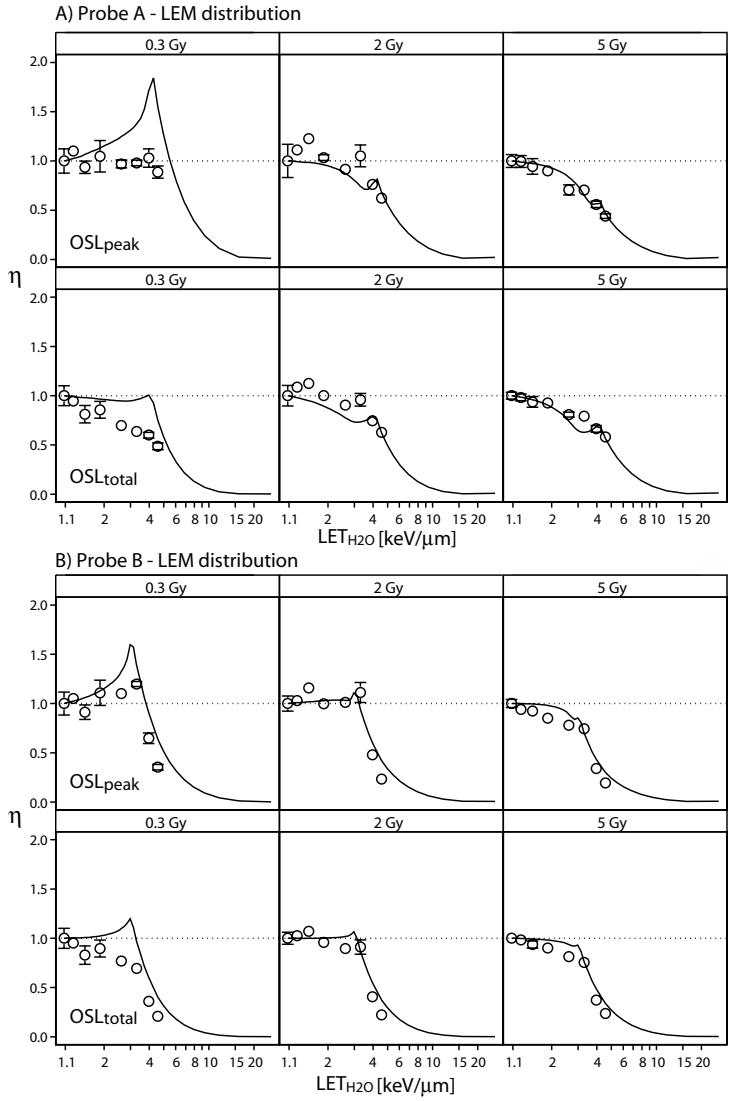

Figure 5.14: The relative efficiency η using D_{LEM}. Experimental data are shown by open circles and model calculations are indicated by the full line and for **A** probe A and **B** and probe B. Upper panels in **A** and **B** show the peak OSL signal while the lower panels show the total OSL signal.

calculations made with D_{Site} (fig. 5.15) fits the efficiencies better than calculations made with D_{LEM} (fig. 5.14) and both distributions fits probe B better than probe A. For probe A, the calculated efficiency for the peak OSL signal is not in good agreement with experimental data for neither D_{LEM} nor D_{site} in the 0.3 Gy panel. As with $f(D)$, the overestimate of η could be due to the decline in γ-response after saturation which is not captured by

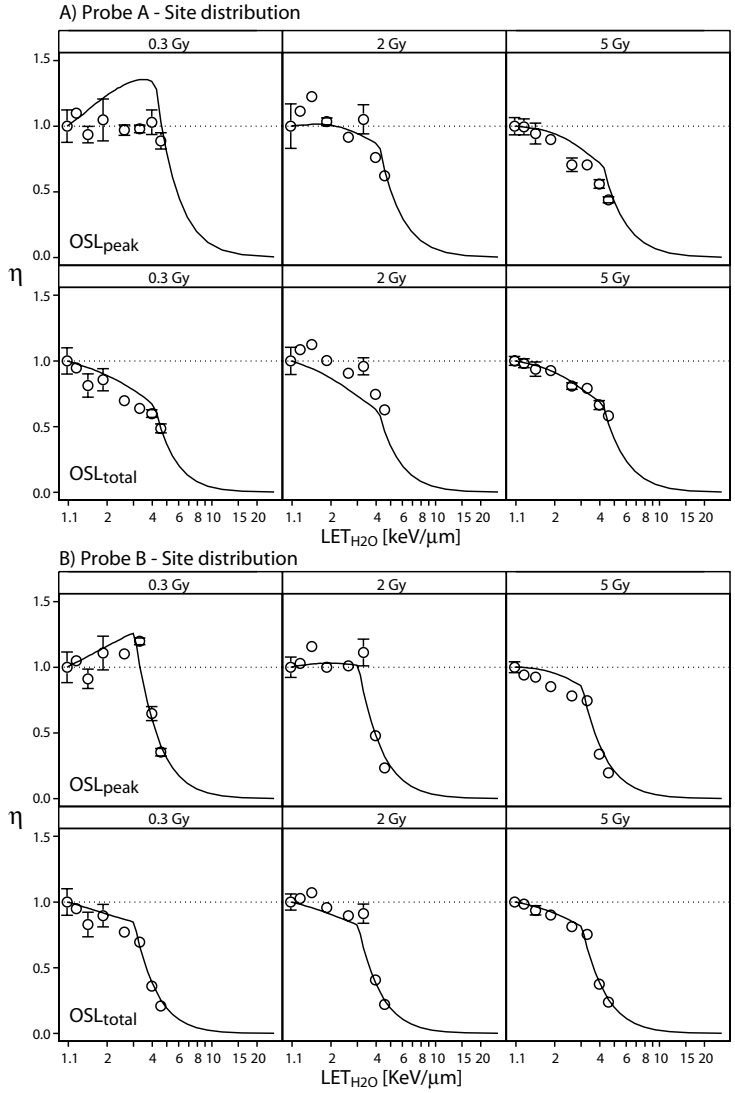

Figure 5.15: Identical with figure 5.14 for the experimental data while model calculations in this figure are made with D_{Site}.

the model (see fig. 5.8). At larger doses, the agreement between calculated and experimental values gets better for both the peak and total OSL signal. D_{LEM} in figure 5.14 shows an intermediate peak that looks somewhat artificial although a similar behavior of calculated efficiencies have been observed previously [90]. This peak is not found in D_{Site}. The model calculations predict that the efficiency will eventually decrease when the LET becomes large enough regardless of the dose.

The estimated values of a_0 in Al_2O_3:C for the peak and total OSL signal for the two probes are collected in table 5.1. The estimates of a_0 is about 3–4 times lower using D_{LEM} instead of D_{site} for probe A and B. a_0 is found to be between 30 and 150 nm depending on the dose distribution used in the calculations. Based on the total integrated thermoluminescence response, a recently reported value of a_0 was found to be around 40 nm in Al_2O_3:C which is within the interval of the a_0 values found here [68].

Dose dist	OSL signal	Probe A: a_0 [nm]	Probe B: a_0 [nm]
LEM	peak	40	30
	total	40	30
Site	peak	130	95
	total	150	100

Table 5.1: Estimates of the target radius a_0 in Al_2O_3:C for probe A and B using the two dose distributions D_{LEM} and D_{site} in the model calculations.

5.3 Discussion

5.3.1 Assumptions and limitations

A simplification made in the model is that all protons are considered as average mono-energetic particles which ignores the characteristics of the beam line (fig. 5.7), energy straggling (fig. 5.13) and the production of secondary protons. The Al_2O_3:C crystals are covered with a colored araldite jacket of 0.25 mm (probe A) and 0.5 mm (probe B) [57] which means that the energy and direction of the protons reaching the Al_2O_3:C crystals will be different from the initial one and this gets more pronounced as the energy gets lower. Some spread in the experimental data is also observed and based on the radioluminescence (RL) response from the probes we believe that this is due to fluence fluctuations in the accelerator (data not shown but consult article 3 in the introduction).

The assumed target in the center of the proton track is probably a rather crude representation of the protons interaction with the luminescence system. Also, the difference in the estimate of a_0 shows that the model is quite sensitive to the dose distribution used and from the results presented, we found that the best fit to data was made with D_{Site}. We used a range-energy relationship for the δ-rays found experimentally in water by Waligórski et al. [89]. Although a density scaling factor was introduced, this might not

be sufficient to apply the relation in Al_2O_3. Horowitz et al. suggested with the modified track structure theory that the δ-ray energy spectrum created from γ-irradiation does not mimic that created by HCPs. Instead, the γ-response should be replaced by a low-LET response which creates a δ-ray energy spectrum that more closely resembles that created by the HCP in question [39].

5.3.2 Interpretation of a_0

What is a target with radius a_0? This question is more easy to answer when the dosimeter response is a direct measure of a quantity being ionized. For example, in nuclear emulsion the target is a darkened grain and a_0 is the physical size of that grain. In luminescence dosimeters, electron-hole pairs are created during irradiation which are subsequently captured by electron and hole traps. After irradiation, these traps are emptied for charge carriers by stimulating with either heat or light and the released charge then annihilates at a recombination center which finally emits the luminescence signal. So is a_0 the size of a trap, a recombination center, the distance between them or something else? The most reasonable thing to do is to look at some characteristic distances in Al_2O_3:C. Obviously, a distance of the order of 10-100 nm is too large to represent atomic defects thereby excluding trap size estimates. The lattice constant in Al_2O_3 is 0.2 nm [22] and the carbon dopant concentration for the probes used is about 100 ppm [4]. This leads to an average distance between carbon defects of about 4 nm.

The concentration of luminescence centers (F^+-centers) in Al_2O_3:C is reported to be around 10^{17} cm^{-3} which gives an average distance of about 50 nm between F^+-centers [63]. This distance corresponds well with the estimates obtained and therefore we follow the present interpretation of a_0 as representing the average distance of charge migration in the probe before it is trapped [68]. Large concentrations of pre-existing (radiation-independent) holes in the F^+-centers of Al_2O_3:C are known to exist [24] and this was for example implemented in the temperature simulations (by the m_0 parameter in fig. 4.8). A one-hit trap could then be interpreted as an electron recombining with a pre-existing hole at an F^+-center while a two-hit target requires the migration of both an electron and a radiation induced hole to an F^+-center in order to produce light (i.e. for activation to occur). This interpretation of a_0 as a charge migration distance finds its root in the unified interaction model (UNIM).

One can obtain an independent estimate of the radius from target theory. If we use 2.7 times the energy band-gap (see section 2.3.5) [20], E_{gap}, of Al_2O_3 as the ionization energy there is 1 Gy/$2.7E_{gap}$ ionizations per kg Al_2O_3

irradiated with 1 Gy. When $D = E_c$ the number of ionizations equals the number of targets if we take an ionization as one hit and one target then weights $(E_c/2.7E_{gap})^{-1}$. If we assume that a target has the form of a sphere an estimate of the target radius can then be found as

$$a_0 = \left(\frac{2.7E_{gap}}{\frac{4}{3}\pi\rho E_c}\right)^{1/3} \tag{5.3}$$

were ρ is the density of Al_2O_3. If we take $E_{gap} = 8.7$ eV and the reported values for E_c in figure 5.8 we obtain an estimate of a_0 between 35-86 nm.

5.3.3 Luminescence properties and geometry

Even for a material with perfect LET-independent response, the relative efficiency of the bulk signal from such a detector would eventually become LET-dependent at low enough energies due to the geometry of the detector. A smaller and smaller mass of the detector would simply experience energy deposition which will limit the response as illustrated in figures 5.9 and 5.13.

We use the model to investigate the LET-dependence of Al_2O_3:C for an infinitively thin detector with eq. (2.43) thereby removing the influence of geometry. Figure 5.16 shows the relative efficiency for the peak OSL signal of probe B using D_{Site}. The efficiency, η_{mix}, is composed of a one-hit

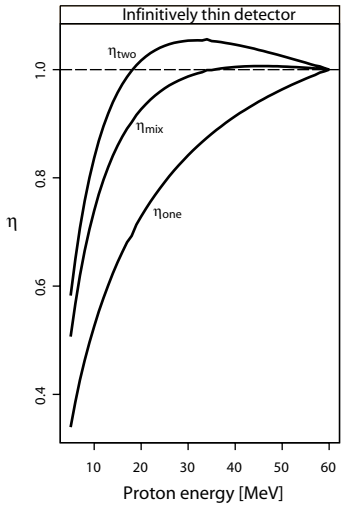

Figure 5.16: The figure shows the relative efficiency for an infinitively thin detector at 1.7 Gy for the peak OSL signal of probe B using D_{Site}. The relative efficiencies for a pure one-hit and two-hit detector and a mixture is indicated by η_{one}, η_{two} and η_{mix}.

and two-hit component that under- and over-responds respectively. For the

calculation, the efficiency is LET-independent in the energy interval 30-60 MeV. For a given mixture of one- and two-hit components and a specific detector geometry, the OSL response can then be LET-independent in a given interval at a certain dose as observed for the peak OSL signal of probe A in the 0.3 Gy panel of figures 5.14 and 5.15. However, this would not be the case for other doses and geometries which is also apparent from those two figures. Since the presence of one- and two-hit components in the peak and total OSL signal differ (see fig. 5.8), one could obtain an LET independent OSL response over a certain LET and dose interval by mixing an under and over-response of the two OSL signals. This approach has for example been applied for scintillators [79].

5.4 Conclusions on proton energy effects

We investigated the cw-OSL response from Al_2O_3:C irradiated with 10-60 MeV protons monitoring the F-center. The experimental data showed an LET independent response at 0.3 Gy and energies larger than 10 MeV for the initial OSL signal while this signal and the total OSL signal showed LET dependence for all other doses investigated. We analyzed the data using target and track structure theory to gain insight into the physics underlying the OSL response and estimate the applicability of this material for proton dosimetry.

Although several simplifications were made to ease calculations, the classic track structure theory can qualitatively account for all the main features of the experimental data. We estimate a target radius to be between 30 and 150 nm and associate this radius with a charge migration distance in the crystal. The model calculations suggest that the dose and LET dependence of the OSL response is a result of an unique mixture of one- and two-hits components. This implies that the initial OSL response from Al_2O_3:C in general is not LET independent at 0.3 Gy or lower doses. A mixture of the peak and total OSL signal could, however, provide a LET independent response in a given LET and dose interval or Al_2O_3:C could be combined with other materials having different LET-characteristics to determine the total absorbed dose of complex radiation fields.

6 Overall conclusions and outlook

An all optical system using the radioluminescence (RL) and optically stimulated luminescence (OSL) signal from small fiber–attached crystals of carbon doped aluminum oxide (Al_2O_3:C) was recently introduced as a tool for medical dosimetry [10]. It was demonstrated that this RL/OSL system has a considerable potential for applications in both radiotherapy and mammography [14]. To further improve the performance of the RL/OSL system within the field of medical dosimetry, this PhD study investigated some of the fundamental dosimetric properties of the OSL signal from Al_2O_3:C in greater detail.

The need to perform measurements at different temperatures has always existed in luminescence dosimetry along with corresponding requirements and desires to correct and understand the impact of temperature on the luminescence output. This general interest combined with the increasing demands to provide *in–vivo* dose verifications of radiotherapy treatments in medical dosimetry [46] made the choice to systematically study some fundamental effects and mechanisms of temperature on the OSL and RL signals an obvious one. A less obvious choice was to investigate the impact of ionization density on the OSL signal. Such investigations have, however, recently been initiated in space dosimetry [96, 97] and therefore the effects of irradiating OSL dosimeters with heavy charged particles (HCPs) at different energies, from a general point of view, represents one of the recent frontiers within the research of OSL and RL dosimetry. Furthermore, the number of medical facilities that offer particle therapy to cancer patients, hereunder first and foremost proton therapy, is rapidly increasing worldwide [81]. From this point of view, therefore, the role of dosimetry based on the OSL output from Al_2O_3:C needs to be clarified when discussing the different options available to provide the best possible quality assurance in connection with particle therapy.

This chapter summarizes the conclusions from chapter 4 and 5 and highlights the major finding and how they relate to existing works. At the end of the chapter, an outlook on the future research with temperature and ionization effects on the luminescence signal from Al_2O_3:C is given.

6.1 New findings

A key problem in OSL dosimetry using Al_2O_3:C is that the OSL signal from this material decays faster with increasing dose, temperature and ionization density (proton LET). As a result, the investigations primarily focused on how changes in temperature and ionization density affect the OSL signal at different integration times and doses.

Effects of temperature

One significant contributor to uncertainties in most OSL materials is their temperature dependence. The integrated OSL and RL signals investigated here quantify the temperature effect for conditions directly relevant in medical dosimetry (20 to 40 °C). Both signals are changing between -0.2 to 0.6 % per ^{o}C which gives the overall order of changes in the optical luminescence response from Al_2O_3:C with temperature. One can then determine whether it is necessary to correct for the effects of temperature depending on the uncertainty requirement and temperature fluctuations involved in a given application.

The prime study previously made on the temperature dependence of the OSL response from Al_2O_3:C indicated that the OSL response increases with stimulation temperature [58]. We showed, however, that the OSL response changes with both irradiation and stimulation temperature as well as OSL integration time and concluded that the OSL signal can both increase and decrease with stimulation temperature whereas the RL response only depends on irradiation temperature. The initial part of the OSL signal increases while the total OSL signal decreases with temperature. If a calibration curve at room temperature is based on the initial OSL signal, the use of the initial OSL signal will overestimate the dose at elevated temperatures while the opposite is true for the total OSL signal. Therefore, an intermediate integrated OSL signal can be found that will provide the same dose estimate independent of stimulation temperature.

We conclude that temperature effects on the OSL response can be eliminated by integration if the irradiation temperature is not varied and recommend that the calibration and the measuring process are carried out at the

same irradiation temperature (i.e. at body temperature for *in-vivo* measurements).

On the basis of a band structure model, two possible thermal mechanisms, termed shallow traps and thermal excitation, were simulated to offer possible explanations for the temperature effects. Both phenomena could explain the initial increase of the OSL decay curve with increasing irradiation and stimulation temperature and overall the numerical simulations suggested that the qualitative behavior of the OSL signal with temperature is a result of the combined effects of shallow traps and thermal excitation. This was also the conclusion reached by Markey et al. but on the basis of fewer experimental data [58]. Also, the band structure model simulations indicated that the effects of shallow traps could be reduced by choosing a constant irradiation temperature since thermal excitation seems to dominate the temperature effects of the stimulation process.

Effects of ionization density

The LET of protons is changing as they slow down inside a patient and therefore an important issue is to characterize the change in dosimeter response with LET for correct dosimetry. The LET dependence of the OSL response from Al_2O_3:C was characterized for protons with initial energies between 10 to 60 MeV. To our knowledge, this is the first fiber–coupled Al_2O_3:C crystals, i.e. crystals that are repeatedly re–used for dosimetry measurements, that have been irradiated with protons.

For a given proton dose, both the initial and total OSL signal decrease with increasing LET of the protons leading to an underestimate of the dose compared to a calibration curve obtained with γ-radiation. For the probes investigated, this is always true for the total OSL signal at all doses while the initial OSL signal can provide a LET independent dose estimate at a given dose and LET interval, here found to be in the interval 1.08 to 4.57 keV/μm for the LET in water at 0.3 Gy.

Yukihara et al. was the first to establish the connection between the dose and energy dependence of the OSL decay rate from Al_2O_3:C [95]. In that study, the energy dependence was reported for a test dose of 100 mGy. Here, we described the energy dependence of the OSL decay rate for a wider range of conditions for protons with LET values in the interval 1.08 to 4.57 keV/μm in water over a spectrum of test doses between 0.1 and 30 Gy. On this basis, we confirmed the energy dependence of the OSL decay rate (faster rate with increasing LET) as reported by Yukihara et al. and furthermore concluded that this energy dependence changes with the test dose given.

Yukihara et al. could explain the dose dependence of the OSL decay rate with a band structure model similar to the one used to simulate temperature effects in this thesis [98]. Since this model only accounts for delocalized phenomena, i.e. a uniform ionization density, it can not account for the energy dependence of the OSL decay shape since this relates to local changes in the ionization density. Here, we applied track structure theory (TST) to explain the energy dependence of the OSL response. Although several simplifications were made to ease calculations, we found that TST could qualitatively account for all the main features of the experimental proton data.

TST model calculations, independent of detector geometry, were made to see if the LET independence of the initial OSL signal at 0.3 Gy was a general property of Al_2O_3:C. The calculations showed that the initial and total OSL response arise from different concentrations of so–called one- and two-hit components. The LET independence of the initial OSL signal is a result of the unique mixture of the geometry of the probe and the concentration of one- and two-hit components.. This implies that the initial OSL signal from Al_2O_3:C in general is not LET independent at 0.3 Gy or lower doses. Therefore, we conclude that Al_2O_3:C is not a very suitable material for proton OSL dosimetry if one wishes a signal that in general is independent of LET effects.

However, the model calculations also indicated that for other dosimeter geometries than the ones used here, it would be possible to use a weighted sum of the initial and total OSL signal to provide an LET independent dose-response for a given LET and dose interval. Therefore, under certain specified conditions, the OSL signal from Al_2O_3:C could provide an LET independent signal.

Using TST, we estimated the so-called target radius to be between 30 and 150 nm and, based on the concentration of luminescence centers (F^+-centers) in Al_2O_3:C, associated this radius with a charge migration distance in the crystal. This migration distance can then be used to formulate a hypothesis for the one- and two-hit processes that result in the production of luminescence as shown in figure 6.1. This interpretation of a_0 as a migration distance finds its root in the framework of the unified interaction model (UNIM) where the distance between luminescence centers and electron traps determine the degree of supralinearity of the dose-response [41].

6.2 An optimal OSL protocol?

What are the desired features one wishes an optimal OSL protocol to contain in order to handle the requirements encountered in medical dosimetry?

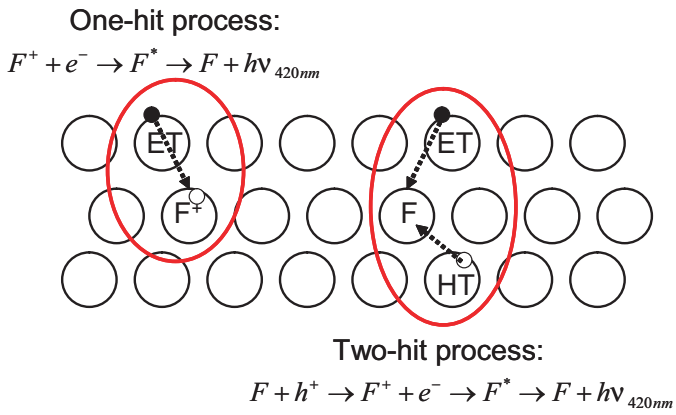

Figure 6.1: A possible interpretation of the one- and two-hit processes resulting in the production of luminescence. A one-hit process requires the migration of an election from an electron trap (ET) to a luminescence center containing a hole (F^+)-center. A two-hit process requires the migration of both an electron from an ET and a hole from a hole trap (HT) to a luminescence center (F-center) before recombination can occur.

In order to answer that question, several important issues are necessary to consider to obtain a high credibility of quality assurance. Here, we try to list some of those issues:

- A high reproducibility of the protocol, i.e. the ability to repeatedly provide the same dose estimate for identical irradiations which in turn means the ability to reset or bleach the dosimeter crystals back to a known initial sensitivity after irradiation. This is especially important if the crystals are being re–used as described in section 3.4.

- For practical purposes, an important issue in medical dosimetry is to keep the time spent on a dose verification procedure to a minimum which for a OSL protocol means a fast readout time of the OSL signal.

- A high sensitivity of the signal to reduce uncertainties from background noise and statistical fluctuations in the signal. This is, for example, important for the total OSL signal and less critical for the initial OSL signal when a cw-OSL protocol is used.

- A protocol which is independent of temperature and LET effects and other effects like photon energy and dose–rate. Overall the protocol should only vary with dose.

- A protocol which is simple to carry out.

As mentioned in the introduction, several readout protocols of the OSL signal are available which all depend on when and how the stimulation light is provided. They all posses a potential to fulfill some of the requirements mentioned above. The most applied protocols in OSL dosimetry are:

- The pulsed OSL (POSL) protocol.
- The linearly modulated OSL (lm-OSL) protocol.
- The real-time OSL protocol.
- The continuous wave OSL (cw-OSL) protocol.

In the POSL protocol, the stimulation light is turned on and off periodically and the OSL afterglow between pulses is monitored. In this way, the OSL signal is collected within a very short period of time which reduces the influence of background and improves the sensitivity. Also, one separates the stimulation and emission light by time discrimination and consequently the amount of optical light filtration can be reduced [64, 9, 63].

In the lm-OSL protocol, the intensity of the stimulation light is increased linearly and the luminescence monitored during stimulation similar to the cw-OSL protocol [94]. In this way, different crystal trap components with different photoionization cross-sections can (ideally) be read out separately and consequently be available for a mixed OSL signal.

In the real-time OSL protocol, it is possible to monitor the cw-OSL signal during irradiation [73]. The advantage of this protocol is that it provides real-time dose estimates based on the OSL signal.

Preferably, an optimal OSL protocol should incorporate procedures that take all of the above requirements met in medical dosiemtry into account. However, when one goes through the possibilities that are available with the different OSL readout protocols it becomes apparent that the wish for a single OSL protocol that can satisfy all requirements is hard to accomplish. Rather, one should aim for the simplest protocol that can account for the most desired features. Although the protocols mentioned above could be excellent candidates as optimal OSL protocols in medical dosimetry, this study has been concerned with the effects of temperature and ionization density on the cw-OSL protocol and we can therefore only make qualified statements about these issues.

With the cw-OSL protocol, the ability to change the dose-response with integration time or by mixing different parts of the OSL signal is available in a straight forward way. In some cases, the change in OSL decay rate is an advantage one wishes to utilize. For example, one can use the change in

OSL decay shape to determine the energy of a monoenergetic proton irradiation or identify single components in mixed radiation fields or determine the temperature at which a certain irradiated dose was obtained. In most cases, however, one wishes to obtain dose estimates which are not effected by neither the LET of the radiation nor the stimulation and irradiation temperature. It is clear from section 6.1 that the integration time is a strong tool for elimination of undesired effects on the OSL signal. Also, a mixture of the different parts of the OSL signal, for example the initial and total OSL signal, can be used to eliminate effects.

An outlook with cw-OSL based dosimetry

The integration time of the OSL signal can be chosen to eliminate the effects of temperature and proton energy on the OSL signal when applying a cw-OSL protocol. This can either be done by varying the integration time directly or by mixing different integrated parts of the OSL signal in a weighted average. One obvious problem with this strategy is that the integration time depends on the intensity of the stimulation source, the optical couplings between the reader, fiber cable and the crystal, and the geometry of the crystal. In other words, the integration times or weighting factors would have to be obtained explicitly for every combination of reader, fiber cable and crystal used.

Another strategy is to keep the integration time constant and apply correction factors to the OSL signal in order to correct for temperature and LET changes. Such correction factors could for example be the temperature coefficients shown in table 4.3 or the supralinearity factors or relative efficiency shown in figures 5.11, 5.12 and 5.14 and 5.15. Since most of these factors are relative quantities, they would be independent of the optical specifications for a given reader system and only depend on stimulation intensity, dosimeter material and geometry.

Given the overall uncertainty connected to radiation therapy such correction factors must be determined with high accuracy. If the coefficients are obtained experimentally, the experiments should be well controlled and of high precision. If the coefficients are obtained on the basis of a model, this model must very accurately represent the real physical processes that takes place in the dosimeter. As mentioned in the introduction, approaches towards obtaining such coefficients are presently being taken as indicated by two of the abstracts (abstracts 1 and 2 in the introduction) submitted to the 15th Solid State Dosimetry Conference 2007. In abstract 2, a precisely controlled experiment has been conducted which contains all the presented temperature and dose combinations in one experiment monitoring both the RL and OSL signal. On the basis of this experiment, temperature correction

coefficients will be presented for both the RL and OSL signals. In abstract 1, the OSL γ-response is folded with the Monte Carlo transport code GEANT4 which mimic the loss of energy of protons through the dosimeter crystal much more accurately than the model presented here. On the basis of these model simulations, correction factors can be obtained that can correct for the LET sensitivity of the RL and OSL signals.

A Calculations

A.1 Dose-distribution

The δ-ray theory of track structure was first described by Katz et al. in the 1960s [23, 52, 51]. We will use his approach together with a power-law range-energy relation for the delta-rays as described by Hansen et al. [33, 35] to deduce the point-target dose distribution. The cross-section for ejecting an electron[1] with energy between ω and $\omega + d\omega$ along the path of a heavy charged particle (HCP) is given by

$$d\sigma_\omega = \frac{2\pi e^4}{mc^2}\frac{z^2}{\beta^2}\frac{d\omega}{\omega^2} \tag{A.1}$$

where m and e are the mass and charge of the electron, c is the speed of light and z and β are the effective charge and velocity relative to that of light for the HCP [19]. The number of electrons ejected per unit path length of the HCP is obtained by multiplying this cross-section with the electronic density, N, of the dosimeter

$$dn = C\frac{z^2}{\beta^2}\frac{d\omega}{\omega^2} \tag{A.2}$$

where $C = 2\pi Ne^4/mc^2$ has the unit of energy per length. The relation between the energy of the ejected electron and its range usually takes a power-law form

$$r = k\omega^\alpha \tag{A.3}$$

where r is the range of the electron with energy ω and k and α are constants obtained experimentally or by Monte Carlo simulation. The units of r and k are g/cm^2 and g/cm^{2}keV$^\alpha$, respectively. Since the dose alone varies with distance from the path of the HCP only the perpendicular range is of interest.

[1] Here, the consideration is restricted to electrons with high energy compared to the ionization potential of the material atoms. Neglecting the binding energy of the electrons means that their collision with the heavy ions can be described by Rutherford scattering.

If we assume that all electrons are ejected perpendicularly to the path of the HCP, the range in eq. (A.3) can be used as the integration limit which simplify calculations [53]. This assumption is reasonably justified when considering the angular distribution of the electrons of energy ω

$$\cos^2\theta = \frac{\omega}{\omega_{max}} \tag{A.4}$$

where θ is the angle between the path of the HCP and the ejected electron and $\omega_{max} = 2mc^2\beta^2(1-\beta^2)^{-1}$ is the maximal energy transferred to the ejected electron from the HCP in a head-on collision [52]. From eq. (A.2) it is seen that the majority of the delta-rays have small energies due to the $1/\omega^2$ dependence. Therefore $\omega/\omega_{max} \ll 1$ for most electrons making $\theta \sim 90°$. The energy delivered by an electron to the dosimeter a distance r from the HCP track can be found by use of eq. (A.3). After traveling a distance r, an electron with initial energy ω and corresponding range R will have a remaining kinetic energy, ε, of

$$\varepsilon = (\frac{R-r}{k})^{\alpha^{-1}} = (\frac{R}{k})^{\alpha^{-1}}(1-\frac{r}{R})^{\alpha^{-1}} = \omega(1-\frac{r}{R})^{\alpha^{-1}} \tag{A.5}$$

After a distance $r+dr$, the electron will have the energy $\varepsilon - d\varepsilon$. The energy loss per unit length by the electron in the interval dr at distance r from the track is then the differential quotient

$$\frac{d\varepsilon}{dr} = -\frac{\omega}{\alpha R}(1-\frac{r}{R})^{\alpha^{-1}-1} \tag{A.6}$$

The total energy deposited in the interval dr a distance r from the track of the HCP is given by multiplying the number of electron of energy ω (eq. (A.2)) with their corresponding energy loss (eq. (A.6)) and integrating over all energies having a corresponding range of r or larger

$$E(z,\beta,r) = \int_{\omega_r}^{\omega_{max}} \frac{dn}{d\omega}\frac{d\varepsilon}{dr} dr d\omega \tag{A.7}$$

$E(z,\beta,r)$ is the energy per unit length delivered by the δ-rays a distance r from the HCP with effective charge z and relative velocity β. Substituting the energy of the delta-rays by the corresponding range (eq. (A.3)), performing the integration and dividing with the area of the shell and the density of the dosimeter gives the radial dose distribution in Gy as

$$D(z,\beta,r) = \frac{E}{2\pi\rho r dr} = \frac{C}{2\pi}\frac{z^2}{\beta^2}\frac{1}{\alpha\rho}\frac{1}{r^2}(1-\frac{r}{R_{max}})^{\alpha^{-1}} \tag{A.8}$$

To get the right units, r and R_{max} must be in units of length which means that eq. (A.3) must be divided by the density, ρ, of the material. Eq. (A.8) is the basic radial dose formula known as the point target dose distribution. It contains a constant term dictated by the HCP and the dosimeter material, an inverse square dependence on the radial distance and two restricting parameters, namely the maximum range of the most energetic delta-rays R_{max} and the power α. Figure A.1 shows the radial dose distribution using eq. (A.8) for protons.

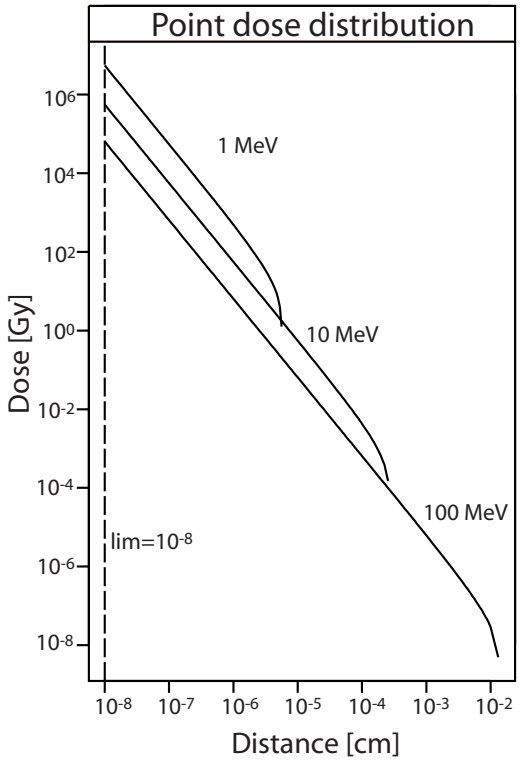

Figure A.1: Radial dose distribution calculated from eq. (A.8) for protons in Al_3O_2 with $lim = 0.1$ nm. The numbers indicate the energy of the protons. R_{max} is calculated from eq. (A.3) using values for k and α by Waligórski et al. scaled with a density factor for Al_2O_3 [89].

A.1.1 Extended target calculation

Let us consider the target as a cylinder of unit length and radius a_0 having its axis parallel to the path of the HCP. Although different parts of the cylinder experience different doses in the strongly varying field surrounding the path

of the HCP, the model assumes that the target responds according to the average dose $\overline{D}$ delivered to it. If the center of the target is placed a distance r_0 from the path of the HCP, the average dose delivered to the target can be written as

$$\overline{D}(z,\beta,r_0,a_0) = \frac{1}{A}\int_{r_0-a_0}^{r_0+a_0} D(z,\beta,r)2\phi r dr \tag{A.9}$$

where A is the area πa_0^2 of the target, r is the free variable to be integrated and ϕ is a geometry function. The geometry function is determined by the shape of the target volume and for a cylinder it is given by

$$\phi = 2\arctan\sqrt{\frac{a_0^2-(r_0-r)^2}{(r+r_0)^2-a_0^2}} \qquad \text{for} \quad r > |r_0-a_0| \tag{A.10a}$$

$$\phi = \pi \qquad \text{for} \quad r \leq |r_0-a_0| \tag{A.10b}$$

The center of the targets, r_0, lies close together and therefore the targets overlap. When $r > |r_0 - a_0|$, eq. (A.10a) describes the part of the circular shell, i.e. the arclength, that deposit energy within the target cylinder. When $r \leq |a_0 - r_0|$, all the energy in the shell $2\phi r dr$ is deposited inside the target. Another way of writing eq. (A.9) is

$$\overline{D}(z,\beta,r_0,a_0) = \frac{1}{A}\int_{lim}^{|r_0-a_0|} D(z,\beta,r)2\pi r dr + \frac{1}{A}\int_{|r_0-a_0|}^{r_0+a_0} D(z,\beta,r)2\phi r dr \tag{A.11}$$

where ϕ is given by (A.10a) and lim is the minimum integration distance. At distances where $r_0 \leq lim$, the HCP path is assumed to penetrate the target at its center, i.e. $r_0 = 0$. At distances where $r_0 > 3a_0$, eq. (A.11) approaches the point target distribution (eq. (A.8)) why this formula is usually used here.

A.2 Saturation cross-section

When a dosimeter is described by multi-target or multi-hit activation a distinction between an "ion-kill" mode and a "gamma-kill (γ-kill)" mode is necessary. The concepts were developed from irradiated cell cultures and nuclear emulsion dosimeters and the terminology used to describe the saturation cross section origins from this work [51]. Here, the term that needs determination of a saturation cross-section is the two-hit component

$$P_2 = 1-(1+A)e^{-A} \tag{A.12}$$

where A usually is D/E_2 (see section 2.4).

Let us imagine our detector as a nuclear emulsion detector. At low LET or unsensitive emulsion materials, developed grains are aligned linearly like beads on a string and this situation is denoted as the "grain-count" regime and dominated by γ-kills. At high LET or sensitive emulsion materials, the developed grains are densely packed like a hairy rope and this situation is denoted as the "track-width" regime and dominated by ion-kills. For the same detector material, we move from one regime to the other with increasing LET. In the grain-count regime, the linear density of activated elements (grain-counts) can be described by eq. (A.12) with the substitution

$$A = \frac{z^2}{\kappa\beta^2} \tag{A.13}$$

where z is the effective charge of the irradiated HCP, β is the speed of the HCP relative to that of light and κ is a constant that will be introduced shortly. The density of activated elements (emulsion response) are not properly described by this substitution in the track-width regime. Since the detector response from the passage of a single HCP can be represented by the cross-section of activation, we introduce a saturation cross-section, σ_0, to discriminate between the two regimes such that

$$\frac{\sigma_2}{\sigma_0} = 1 - (1 + \frac{z^2}{\kappa\beta^2})e^{-\frac{z^2}{\kappa\beta^2}} \tag{A.14}$$

When σ_2 is small, γ-kills are dominating and the linear density of grain counts are well described by eq. (A.14).

We then turn to the determination of the material specific constant κ and apply the concepts introduced from nuclear emulsion to our detection system. The value of the plateau for $r/a_0 < 1$ of the radial dose distribution changes with different choices of LET and a_0 (see fig. 2.9). However, if we normalize the dose with the parameter $z^2/\beta^2 a_0^2$ and plot this versus distance from the track, we note that an almost constant value is reached (see fig. A.2). Using the two radial dose distributions presented in section 2.5.2, we get

$$D_{Site}: \quad \frac{D\beta^2 a_0^2}{z^2} = 30 \cdot 10^{-16} \quad \text{Gy·m}^2 \tag{A.15a}$$

$$D_{LEM}: \quad \frac{D\beta^2 a_0^2}{z^2} = 50 \cdot 10^{-17} \quad \text{Gy·m}^2 \tag{A.15b}$$

When $D = E_2$ all targets on average experience one hit and we have that $z^2/\kappa\beta^2 = 1$ in eq. (A.14) which is true when $\kappa = z^2/\beta^2$. Substituting this

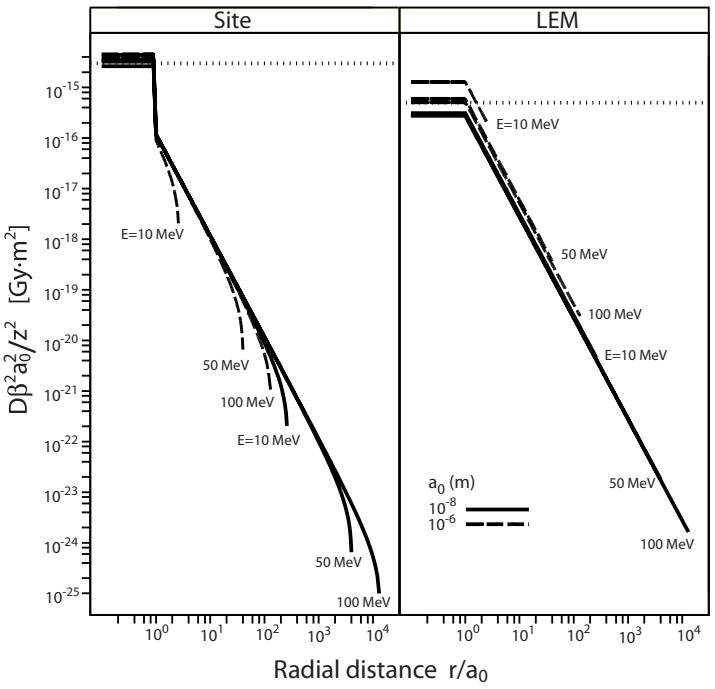

Figure A.2: The parameter $D\beta^2 a_0^2/z^2$ vs. distance from the track in units of a_0 for the two radial dose distributions D_{Site} (left) and D_{LEM} (right). The calculation is shown for two different values of a_0 (10^{-8} and 10^{-6} m) and three different proton energies for each a_0 (10, 50 and 100 MeV). The mean value of the plateau is indicated by the dotted lines and is the result of calculations for proton energies in the interval 1-100 MeV and a_0 in the interval $5{\cdot}10^{-6}$-10^{-11} m.

into eq. (A.15), we obtain the values for κ

$$\kappa_{Site} = \frac{E_2 a_0^2}{30 \cdot 10^{-16}} \quad \mathrm{Gy}^{-1}\mathrm{m}^{-2} \tag{A.16a}$$

$$\kappa_{LEM} = \frac{E_2 a_0^2}{50 \cdot 10^{-17}} \quad \mathrm{Gy}^{-1}\mathrm{m}^{-2} \tag{A.16b}$$

In figure A.3, we plot σ_2/a_0^2 vs. $z^2/\kappa\beta^2$ for a range of proton energies ($z^2 = 1$) and a_0 values. Each curve is for a specific a_0 at energies between 1-100 MeV using eq. (2.36) with $c = 2$ and E_2=3.7 Gy. As a_0 increases the slope of the curves goes from a high values through a plateau to a lower value. At the lower part of the curve (large β and small LET values), we are in the grain-count regime and the curve is well approximated by eq. (A.14) which is shown by the dotted line in fig. A.3. At high LET values, we are in the track-width regime and the detector acts according to one-hit statistics. The plateau of the figure marks the transition between the two regimes and there

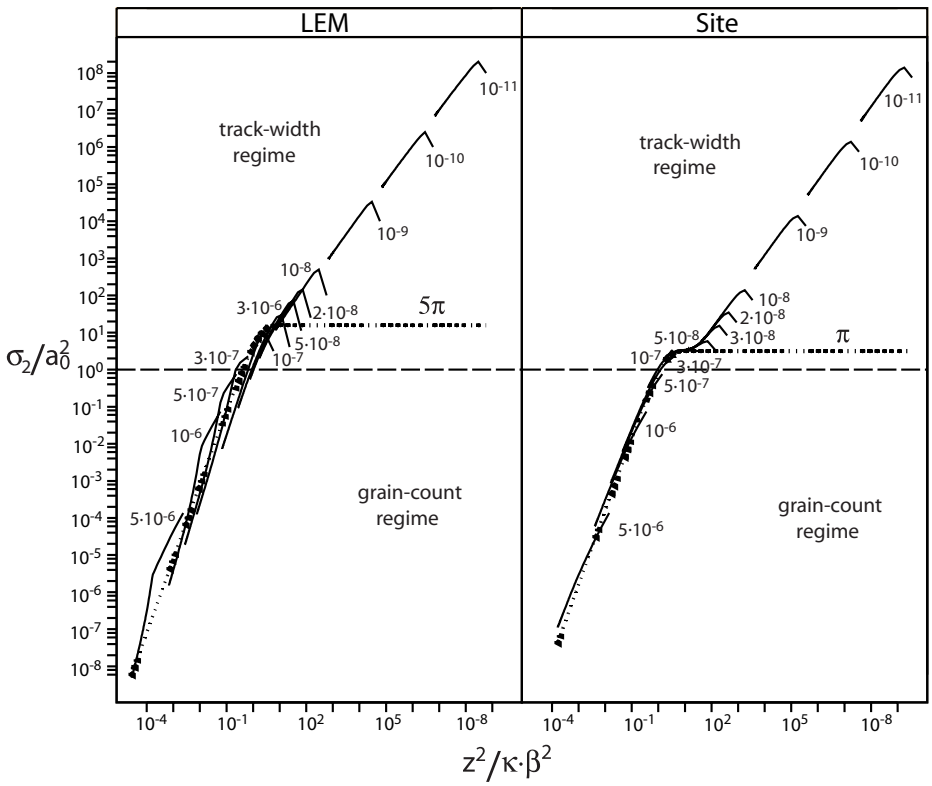

Figure A.3: The cross-section ratio σ_2/a_0^2 vs. the parameter $z^2/\kappa\beta^2$ using D_{LEM} (left) and D_{Site} (right). Different a_0 values in m are indicated by numbers in the figure and each graphs is plotted for 1-100 MeV protons using eq. (2.36) with $c = 2$ and $E_2 = 3.7$ Gy which is the average of the E_2-values in figure 5.8. The dotted line is eq. (A.14) and gives the value of σ_0 in units of a_0^2 at the transition between the grain-count and track-width regime.

we define the saturation cross-section as value of the ratio σ_2/a_0^2. For the two distributions, we find

$$\sigma_0(Site) = \pi a_0^2 \tag{A.17a}$$

$$\sigma_0(LEM) = 5\pi a_0^2 \tag{A.17b}$$

B Computer programs

This chapter presents the different computer codes used to model the temperature and ionization density effects on the OSL response. In the former case, this is done by solving the rate equations in section 2.3.3 at different temperatures according to the protocol indicated in section 4.3 and in the latter by folding radial dose distributions with the γ-response of the crystals resulting in the calculated responses according to eq. (2.43). The essential functions and subroutines necessary to perform the computations are presented to help the interested reader to do his or hers own calculations and to help clarify how the calculations were done explicitly.

B.1 Temperature coding

This section gives the computer programming used to produce the results in section 4.3. The code is written in `Fortran 90`. First, a parameter input file is given to describe the physics of the system together with the sequence file to simulate a given temperature sequence. Then the main program is shown together with the subroutines it uses. The subroutines can be found in Press et al. [77]. The specific equations that are solved to simulate the thermal excitation mechanism with the program "RATE" by Niels Agersnap can be found on page 98 in [1].

B.1.1 Parameter input file

```
! Energy Band Model input file.
! Values for parameters in order:
! nc,n1,n2,n3,h1,h2,nv

0. ,  1e-10, 1e-10, 1e-10,     0.,     0., 0. ! aT, electron trapping probability
0. ,     0.,    0.,    0.,  1e-10,  1e-10, 0. ! aH, hole trapping probability
0. ,     0.,    0.,    0.,   1e-9,  1e-10, 0. ! aR, recombination probability
0. , 5.5e12,  1e12,  1e12,   5e12,   5e12, 0. !  N, number of traps
0. ,    0.7,   1.5,    3.,     0.,     0., 0. !  E, energy depth of electron traps
0. ,   1e13,  1e12,  1e12,     0.,     0., 0. !  s, frequency factor, electron traps
```

B.1.2 Temperature sequence file

```
! This is the sequence file associated with the program "rate_solver.exe"
! Fill in the values on the lines as described at the end of each line.
! IMPORTANT: do not change space separation between lines

yes                     ! New model yes/no
Al_smdrh.txt            ! model filename
test.dat                ! output datafile
0.,0.,0.,0.,1e10,0.,0.  ! initial pop. (nc,n1,n2,n3,h1,h2,nv)
1e-3                    ! initial step size
1e-6                    ! uncertainty (error condition)
0.1                     ! sample rate in datafile
1e7                     ! Irradiation rate, works with 1e10
0.,0.,0.1,0.,0.,0.,0.   ! Stimulation rate

! Sequence start

18                          ! Number of runs, max=100
"RL" ,   1, 100   , 273, 1  ! lum,loop,time,temp,run
"AG" ,   1, 100   , 273, 1
"OSL" ,  1, 600   , 273, 1
"RL" ,   1, 100   , 283, 2  ! lum,loop,time,temp,run
"AG" ,   1, 100   , 283, 2
"OSL" ,  1, 600   , 283, 2
"RL" ,   1, 100   , 293, 3  ! lum,loop,time,temp,run
"AG" ,   1, 100   , 293, 3
"OSL" ,  1, 600   , 293, 3
"RL" ,   1, 100   , 310, 4  ! lum,loop,time,temp,run
"AG" ,   1, 100   , 310, 4
"OSL" ,  1, 600   , 310, 4
"RL" ,   1, 100   , 320, 5  ! lum,loop,time,temp,run
"AG" ,   1, 100   , 320, 5
"OSL" ,  1, 600   , 320, 5
"RL" ,   1, 100   , 360, 6  ! lum,loop,time,temp,run
"AG" ,   1, 100   , 360, 6
"OSL" ,  1, 600   , 360, 6
```

B.1.3 Rate equation solver

```
! Program rate_solver
! This program solves rate equations for crystal system.
! It uses a Runge-Kutta driver with adaptive stepsize control.
! Driver: subroutine Odeint calls both rkqs, rkck and derivs
! Step-controller: subroutine rkqs. calls rkck and derivs
! Algorithm with error-estimate (y(n) -> y(n+1)+ err): rkck. calls derivs
! Rate equations to be solved: derivs.
! Integrate values ystart(1:nvar) from x1 to x2.
! h1 should be the guessed first stepsize, hmin is minimum allowed size.
! Output: ystart is replaced with final y values.
! No memory effects from previous sequences are considered with the introduction
! of y_initial.

  implicit none

  integer,parameter :: nvar=7,Nmax=100
  integer :: nok,nbad,j,i,loop(Nmax),run(Nmax)
  real :: y(nvar),eps,h1,hmin,dydx(nvar),dxsav,y_initial(nvar)
  real :: x1,x_mode,h,dydt(nvar),hdid,hnext,L
  real :: R,R_temp,f(nvar),f_temp(nvar),T_temp
  real :: time(Nmax),temp(Nmax)
```

```
character(len=20) :: filename,newm,modelname,datafile,lum(Nmax)
external derivs,rkck,rkqs,odeint

!!!!!!!!!!!!!!!!!!!!!!!!!!!!!!!!!!!!!!!!!!!!!!!!!!!
! Initial parameters not read from file
!!!!!!!!!!!!!!!!!!!!!!!!!!!!!!!!!!!!!!!!!!!!!!!!!!!
L = 0.    ! Start luminescence
x1 = 0.   ! Start time
x_mode=0. ! Start mode time
dydx=0.   ! Start differential
hmin = 0. ! minimum step size

!!!!!!!!!!!!!!!!!!!!!!!!!!!!!!!!!!!!!!!!!!!!!!!!!!!
! Parameters read from files
!!!!!!!!!!!!!!!!!!!!!!!!!!!!!!!!!!!!!!!!!!!!!!!!!!!

!print *, "Write name of sequence file"
!read *, filename
filename="sequence.dat"
open(10,file=filename,status="old")
read(10,*);read(10,*);read(10,*);read(10,*) ! skip lines
read(10,*) newm ! new model yes/no ?
read(10,*) modelname ! model datafile
read(10,*) datafile ! output datafile
read(10,*) y(1),y(2),y(3),y(4),y(5),y(6),y(7) ! initial pop.
read(10,*) h ! initial step size
read(10,*) eps ! error condition
read(10,*) dxsav ! sample rate in datafile
read(10,*) R ! irradiation rate
read(10,*) f(1),f(2),f(3),f(4),f(5),f(6),f(7) ! stimulation rate
read(10,*);read(10,*);read(10,*) ! skip lines
read(10,*) j
do i=1,j
   read(10,*) lum(i),loop(i),time(i),temp(i),run(i)
enddo
close(10)
R_temp=0.; f_temp=0.; T_temp=temp(1)
y_initial = y
!print *, "Write name of data file"; read *, datafile
open(30,file=datafile,status="unknown")

write(30,'(10(a12),3(a5),a8)') "time","time.mode","n.cond","n.trap.1","n.trap.2"
  ,"n.trap.3","h.trap.1","h.trap.2","h.valence","Lumin","loop","run","temp","L.type"

write(30,'(10(es12.4),2(i4),f10.2,2x,a6)')
  x_mode,x1,y,L,loop(1),run(1),temp(1),lum(1) ! Initial values in data file

do i=1,j
   if (mod(i,3).eq.1) y = y_initial ! no crystal memory
   if (i.gt.1)time(i)=time(i)+x1
   nok=0;nbad=0
   T_temp = temp(i)
   if (lum(i)=="BG".or.lum(i)=="AG") then
      R_temp=0.; f_temp=0.
   else if (lum(i)=="RL") then
      R_temp=R; f_temp=0.
   else if (lum(i)=="OSL") then
      R_temp=0.; f_temp=f
   else
      print *, "no correct lum in ",filename," program aborted"
      stop
   endif
```

```
     call odeint(y,nvar,x1,time(i),eps,h,hmin,nok,nbad,derivs,rkqs,rkck,L,newm,modelname,
        R_temp,f_temp,T_temp,loop(i),run(i),lum(i),x_mode,dxsav)
     print *,lum(i),nok,nbad
  enddo
  close(30)

  !call derivs(x,y,dydx)
  !call RKCK(Y,Dydx,nvar,X,h1,Yout,Yerr,DERIVS)
  !call rkqs(y,dydx,nvar,x,h1,eps,y,hdid,hnext,derivs,rkck)
  !call odeint(y,nvar,x1,x2,eps,h,hmin,nok,nbad,derivs,rkqs,rkck)

end program rate_solver

!!!!!!!!!!!!!!!!!!!!!!!!!!!!!!!!!!!!!!!!!!!!!!!!!!!
! SUBROUTINES
!!!!!!!!!!!!!!!!!!!!!!!!!!!!!!!!!!!!!!!!!!!!!!!!!!!

SUBROUTINE derivs (x,y,dydt,L,newm,modelname,R_temp,f_temp,T_temp)
  implicit none
  integer,parameter   :: nn=7
  integer             :: i
  real                :: T,T_temp,k,ee,h,h1,R,R_temp,L,x
  real,dimension(nn)  :: E,y,dydt,dyt,aT,aH,aR,N,f,f_temp,s,value
  character(len=20)   :: newm,modelname

  ! reading of parameters from modelname
  if (newm=="yes")then
    open(20,file=modelname,status="old")
    read(20,*);read(20,*);read(20,*);read(20,*) ! skip lines
    read(20,*) aT(1),aT(2),aT(3),aT(4),aT(5),aT(6),aT(7)!  e-trap prob.
    read(20,*) aH(1),aH(2),aH(3),aH(4),aH(5),aH(6),aH(7)!  h-trap prob.
    read(20,*) aR(1),aR(2),aR(3),aR(4),aR(5),aR(6),aR(7)!  r-trap prob.
    read(20,*) N(1),N(2),N(3),N(4),N(5),N(6),N(7) ! number of traps
    read(20,*) E(1),E(2),E(3),E(4),E(5),E(6),E(7) ! energy depth
    read(20,*) s(1),s(2),s(3),s(4),s(5),s(6),s(7) ! frequency factor
    close(20)
    newm = "no"
  endif
  T=T_temp;k = 8.671e-5;R=R_temp;f=f_temp
  !!  Rate equations
  ! Electron traps
  ee = 0
  do i=2,4
     dydt(i) = y(1)*aT(i)*(N(i)-y(i))-y(i)*(f(i)+s(i)*exp(-E(i)/(k*T)))
     ee = ee + dydt(i)
  enddo
  ! hole traps
  h =0; h1=0
  do i =5,6
     dydt(i) = y(7)*aH(i)*(N(i)-y(i))-y(1)*y(i)*aR(i)
     h1 = h1 + y(7)*aH(i)*(N(i)-y(i))
     h = h + dydt(i)
  enddo
  ! Delocalized charge
  dydt(7) = R - h1
  dydt(1) = dydt(7) - ee + h
  ! Luminescence
  L = y(1)*y(5)*aR(5)
END SUBROUTINE derivs

SUBROUTINE
RKCK(Y,Dydx,N,X,H,Yout,Yerr,DERIVS,L,newm,modelname,R_temp,f_temp,T_temp)
```

```
! PARAMETER definitions
  INTEGER , PARAMETER  :: NMAX = 50
  REAL , PARAMETER     :: A2=.2,A3=.3,A4=.6,A5=1.,A6=.875,B21=.2,B31=3./40.,B32=9./40.,
                          B41=.3,B42=-.9,B43=1.2,B51=-11./54.,B52=2.5,B53 = -70./27.,
                          B54=35./27.,B61=1631./55296.,B62=175./512.,B63=575./13824.,
                          B64=44275./110592.,B65=253./4096.,C1=37./378.,C3=250./621.,
                          C4=125./594.,C6=512./1771.,DC1=C1-2825./27648.,DC3=C3-18575./48384.,
                          DC4=C4-13525./55296.,DC5=-277./14336.,DC6=C6-.25
  ! Dummy arguments
  REAL                      :: H,X,R_temp,T_temp,L
  character (len=20)        :: newm,modelname
  INTEGER                   :: N
  REAL , DIMENSION(N)       :: Dydx,Y,Yerr,Yout,f_temp
  ! Local variables
  REAL , DIMENSION(NMAX)    :: ak2 , ak3 , ak4 , ak5 , ak6 , ytemp
  INTEGER :: i
  External DERIVS

  DO i = 1 , N
     ytemp(i) = Y(i) + B21*H*Dydx(i)
  END DO
  CALL DERIVS(X+A2*H,ytemp,ak2,L,newm,modelname,R_temp,f_temp,T_temp)
  DO i = 1 , N
     ytemp(i) = Y(i) + H*(B31*Dydx(i)+B32*ak2(i))
  END DO
  CALL DERIVS(X+A3*H,ytemp,ak3,L,newm,modelname,R_temp,f_temp,T_temp)
  DO i = 1 , N
     ytemp(i) = Y(i) + H*(B41*Dydx(i)+B42*ak2(i)+B43*ak3(i))
  END DO
  CALL DERIVS(X+A4*H,ytemp,ak4,L,newm,modelname,R_temp,f_temp,T_temp)
  DO i = 1 , N
     ytemp(i) = Y(i) + H*(B51*Dydx(i)+B52*ak2(i)+B53*ak3(i)+B54*ak4(i))
  END DO
  CALL DERIVS(X+A5*H,ytemp,ak5,L,newm,modelname,R_temp,f_temp,T_temp)
  DO i = 1 , N
     ytemp(i) = Y(i) + H*(B61*Dydx(i)+B62*ak2(i)+B63*ak3(i)+B64*ak4(i)+B65*ak5(i))
  END DO
  CALL DERIVS(X+A6*H,ytemp,ak6,L,newm,modelname,R_temp,f_temp,T_temp)
  DO i = 1 , N
     Yout(i) = Y(i) + H*(C1*Dydx(i)+C3*ak3(i)+C4*ak4(i)+C6*ak6(i))
  END DO
  DO i = 1 , N
     Yerr(i) = H*(DC1*Dydx(i)+DC3*ak3(i)+DC4*ak4(i)+DC5*ak5(i)+DC6*ak6(i))
  END DO
END SUBROUTINE RKCK

SUBROUTINE
rkqs(y,dydx,n,x,htry,eps,yscal,hdid,hnext,derivs,rkck,L,newm,modelname,R_temp,f_temp,T_temp)

  INTEGER n,i
  REAL eps,hdid,hnext,htry,x,dydx(n),y(n),yscal(n),L,R_temp,f_temp(n),T_temp
  character(len=20) :: newm,modelname
  EXTERNAL derivs,rkck
  integer, PARAMETER :: NMAX=50
  REAL errmax,h,xnew,yerr(NMAX),ytemp(NMAX)
  real,PARAMETER :: SAFETY=0.9,PGROW=-.2,PSHRNK=-.25,ERRCON=1.89e-4

  h=htry
1 call
rkck(y,dydx,n,x,h,ytemp,yerr,derivs,L,newm,modelname,R_temp,f_temp,T_temp)
  errmax=0.
  do 11 i=1,n
```

```
     if (yscal(i) .ne. 0.)then
        errmax=max(errmax,abs(yerr(i)/yscal(i)))
     endif
11 enddo
  errmax=errmax/eps
  if(errmax.gt.1.)then
     h=SAFETY*h*(errmax**PSHRNK)
     if(h.lt.0.1*h)then
        h=.1*h
     endif
     xnew=x+h
     if(xnew.eq.x) print*,'stepsize underflow in rkqs'
     goto 1
  else
     if(errmax.gt.ERRCON)then
        hnext=SAFETY*h*(errmax**PGROW)
     else
        hnext=5.*h
     endif
     hdid=h
     x=x+h
     do 12 i=1,n
          y(i)=ytemp(i)
12   enddo
     return
  endif
END SUBROUTINE rkqs

SUBROUTINE
odeint(ystart,nvar,x1,x2,eps,h1,hmin,nok,nbad,derivs,rkqs,rkck,L,
       newm,modelname,R_temp,f_temp,T_temp,loop_t,run_t,lum_t,t_mode,dxsav)

  INTEGER               :: nbad,nok,nvar,run_t,loop_t
  REAL                  :: eps,h1,hmin,x1,x2,ystart(nvar),L,
                           R_temp,f_temp(nvar),T_temp,t_mode
  character(len=20)     :: newm,modelname,lum_t
  EXTERNAL              :: derivs,rkqs,rkck
  integer, PARAMETER    :: MAXSTP=1e6,NMAX=50,KMAXX=1e6,TINY=1.e-30
  INTEGER               :: i,kmax,kount,nstp
  REAL                  :: dxsav,h,hdid,hnext,x,xsav,dydx(NMAX),xp(KMAXX),
                           y(NMAX),yp(NMAX,KMAXX),yscal(NMAX)
  !COMMON /path/ kmax,kount,dxsav,xp,yp
  x=x1
  h=sign(h1,x2-x1)
  nok=0
  nbad=0
  kount=0
  kmax=KMAXX ! number of stored times
  do 11 i=1,nvar
     y(i)=ystart(i)
11 enddo
  if (kmax.gt.0) xsav=x-2.*dxsav
  do 16 nstp=1,MAXSTP
     call derivs(x,y,dydx,L,newm,modelname,R_temp,f_temp,T_temp)
     do 12 i=1,nvar
        yscal(i)=abs(y(i))+abs(h*dydx(i))+TINY ! changed scale
12   enddo
     if(kmax.gt.0)then
        if(abs(x-xsav).gt.abs(dxsav)) then
           if(kount.lt.kmax-1)then
              kount=kount+1
              xp(kount)=x
```

```
              do 13 i=1,nvar
                 yp(i,kount)=y(i)
13            enddo
              write(30,'(10(es12.4),2(i4),f10.2,2x,a6)') t_mode,x,y(1:nvar),
                L,loop_t,run_t,T_temp,lum_t
              xsav=x
           endif
        endif
     endif
     if((x+h-x2)*(x+h-x1).gt.0.) h=x2-x
     call rkqs(y,dydx,nvar,x,h,eps,yscal,hdid,hnext,derivs,
        rkck,L,newm,modelname,R_temp,f_temp,T_temp)
     if(hdid.eq.h)then
        nok=nok+1
     else
        nbad=nbad+1
     endif
     if((x-x2)*(x2-x1).ge.0.)then
        do 14 i=1,nvar
           ystart(i)=y(i)
14      enddo
        if(kmax.ne.0)then
           kount=kount+1
           xp(kount)=x
           do 15 i=1,nvar
              yp(i,kount)=y(i)
15         enddo
        endif
        t_mode=t_mode+hdid
        write(30,'(10(es12.4),2(i4),f10.2,2x,a6)') t_mode,x,y(1:nvar),L,
            loop_t,run_t,T_temp,lum_t
        return
     endif
     if(abs(hnext).lt.hmin)print *, 'stepsize smaller than minimum in odeint'
     t_mode=t_mode+hdid
     h=hnext
16 enddo
  print *,"time reached = ", x
  print *, 'too many steps in odeint'
  x2=x
  return
END SUBROUTINE odeint
```

B.2 Track structure coding

The computer code to perform the track structure theory calculations was written in `S-PLUS` which is a commercial equivalent to the open source language `R` [88, 27]. The radial dose distributions D_{point} (`point.dose.dist`), D_{site} (`sub.dose.dist.02`) and D_{LEM} (`geiss.dose.dist`) are shown together with some usefull functions for the proton energy account through a dosimeter, the maximal δ-ray range and energy deposition outside a_0.

B.2.1 Radial dose distributions

```
####### Point dose distribution (Katz)

point.dose.dist <- function(r.el,N.el=1.2e24,E.p=10,
    k.el=6.13e-6,z.ch=1,alp=1.67,alp.low=1.079,dens=3.97){

    # Calculate the dose doposited by delta-rays in distance
    # r.el from HCP with charge z.ch and energy E.p in material
    # with electron density N.el and density dens using the dose
    # distribution formula by Katz togher with a power form energy-range
    # relation by Waligorski (parameters alp and k.el)
    # INUPUT PARAMETERS:
    # N.el              =   electron density of target material     [cm^(-3)]
    # E.p               =   proton energy                           [MeV]
    # z                 =   charge of HCP                           [dimless]
    # r.el              =   radial distance from core               [cm]
    # alp               =   r=k*E.el^(alp)                          [dimless]
    # alp.low           =   r=k*E.el^(alp.low) for electrons with E.el<1 KeV
    # dens              =   density of material                     [g/cm^(-3)]
    # k.el              =  range constant (Waligorski)              [g*cm^(-2)*keV^(-alp)]


    # Created 12.04.06 by JE (in OK,USA)
    # Revised 25.05.06 by JE

    # CONSTANTS
    m.e     <- 9.1093836e-28    # mass electron                     [g]
    c.l     <- 2.99792458e10    # speed of light                    [cm/s]
    e       <- 4.806529593e-10  # charge of electron                [g^(1/2)*cm^(3/2)*s^(-1)]
    m.p     <- 1.6726217e-24    # mass of proton                    [g]

    # CALCULATION ENERGY CONSTANT
    E0      <- m.p*c.l^2*(1.602e-13)^(-1)*1e-7  # mass -> energy    [MeV]
    b       <- (1-(E0/(E.p+E0))^2)^(0.5)        # rel. speed of HCP [dimless]
    Je      <- 6.242e5                          # J -> MeV          [MeV]
    E.el    <- 2*m.e*Je*c.l^2*b^2/(1-b^2)       # max. elec. energy [MeV]
    if(E.el<1e-3){alp<-alp.low}                 # different alp for low-energy electrons
    R.max   <- k.el*(1/dens)*(1e3*E.el)^(alp)   # max. elec. range  [cm]
    K       <- 2*pi*N.el*e^4/(m.e*c.l^2)*1e-7   # energy constant   [J/cm]

    # EFFECTIVE CHARGE (FROM HANSENS THESIS for protons)
    E.p <- E.p*1e3                              # [MeV]->[KeV]
    z.ch <- 1-exp(-0.2*E.p^(1/2)-1.2e-3*E.p-1.443e-5*E.p)

    # POINT DOSE (in r.el)
    D <- K/(2*pi)*(z.ch/b)^2*(1/alp)*(1/dens)*1e3*1/(r.el^2)*(1-r.el/R.max)^(1/alp) # [Gy]
}

####### Subtraction procedure (Hansen/Olsen)

sub.dose.dist.02 <-
function(r,energy=10,dens=3.97,prot.dat=tab.LET,
E.integrand=E.delta,point.dose=point.dose.dist,R.e=delta.max,
core=1e-8,err=1e-16,N.el=1.2e24){

    # Function calculates the dose distribution using the subtraction method.
    # The total energy deposited by the proton according to LET in prot.dat
    # is subtracted from the energy deposited by delta-rays outside a0
    # using point.dose.dist and E.delta.

    # Created 06.07.06 by JE (in OK, USA)
```

```
    # Modified 10.04.06 by JE
    # Modified 10.09.06 by JE
    # Modified 10.22.06 by JE

    E.p     <- energy       # energy proton         [cm]
    R.max   <- R.e(E.p)     # max. elec. range      [cm]
    a0      <- core         # core radius           [cm]

    # Total energy deposited by 1 proton
    D.total.LET <- approx(prot.dat$MeV,prot.dat$LET,E.p)$y*1.602e-13*dens # J/cm

    # Total energy deposited in track
    E.track <- E.integrand # J/cm

    # Energy deposited in core
    D.core <- (D.total.LET-E.track)/(pi*a0^2*dens*1e-3) # Gy in "volume" pi*low.1^2
    if (D.core < 0){D.core <- 0}
    if(R.max <= a0) {
        R.max <- a0
        D <- r
        ii <- r>R.max
        D[ii] <- NA
        D[!ii] <- D.core
        return(D)
        break
    }
    # Energy deposited outside core
    ii <- r>R.max; r[ii]<- R.max # modification
    D <- r;
    ii <- r > a0
    D[ii] <- point.dose(r[ii],N.el=N.el,E.p=E.p,dens=dens)
    D[!ii] <- D.core
    return(D)
}

####### LEM model (Scholz/Geiss)

geiss.dose.dist <-
function(r.el,energy=10,core=1e-8,density=3.97,prot.dat=tab.LET,
    k.el=6.13e-6,alp=1.67,alp.low=1.079){

    # Function calculates dose at r.el in core for r.el<=r0 and in
    # penumbra for r.el>r0 in material with density "density" using the dose
    # distribution formula by Geiss togher with a power form energy-range
    # relation by Waligorski (parameters alp and k.el)
    # r.el              = radial distance from HCP core         [cm]
    # energy            = proton energy                         [MeV]
    # core              = core radius of track                  [cm]
    # prot.dat          = data.frame proton energy, LET and range from p-star
    #                     names should be "MeV","LET",""R.max"
    # alp               =   r=k*E.el^(alp)                      [dimless]
    # alp.low           =   r=k*E.el^(alp.low) for electrons with E.el<1 KeV
    # dens              =   density of material                 [g/cm^(-3)]
    # k.exp             =  range constant (Waligorski)          [g*cm^(-2)*keV^(-alp)]

    # Created 04.12.06 by JE (in OK,USA) as geiss.dist
    # Revised 05.25.06 by JE as geiss.dose.dist
    # Revised 05.26.06 by JE
    # Revised 08.24.06 by JE
    # Revised 10.22.06 by JE

    # electron energy calculation
```

```
    m       <- 1.6726217e-27                    # mass of HCP           [kg/u]
    m.e     <- 9.1093836e-31                    # mass of electron      [kg]
    c       <- 299792458.                       # speed of light        [m/s]
    E0      <- m*c^2*(1.602e-19)^(-1)*1e-6      # mass ->   energy      [MeV]
    b       <- (1-(E0/(energy+E0))^2)^(0.5)     # rel.speed of HCP      dimless
    Je      <- 6.242e12                         # J -> MeV              [MeV]
    E.el    <- 2*c^2*m.e*Je*b^2/(1-b^2)         # max energy electron   [MeV]
    if(E.el<1e-3){alp<-alp.low}                 # different alp for low-energy electrons
    R.e     <- k.el*(1e3*E.el)^(alp)            # max. elec. range      [cm]
    r0      <- core                             # variable change

    # Get stopping power from p-star table
    LET     <- approx(prot.dat$MeV,prot.dat$LET,energy)$y

    # Same units: energy J, mass kg, length cm
    LET     <- LET*1.602e-13*density        # [MeVcm^2/g] -> [J/cm] (density not yet converted)
    R.e     <-  R.e*density^(-1)            # [g/cm^2]    -> [cm] (density not yet converted)
    g       <-  density*1e-3                # [g/cm^3]    -> [kg/cm^3]

    if(R.e < r0) {
        R.e <- r0
        bb <- (1+2*log(R.e/r0))*pi*g*r0^2
        k  <- LET/bb    # J/kg=Gy
        D <- r.el
        ii <- r.el>R.e
        D[ii] <- NA
        D[!ii] <- k
        return(D)
        break
    }

    # Normalization constant, i.e. total dose deposited
    bb <- (1+2*log(R.e/r0))*pi*g*r0^2
    k  <- LET/bb    # J/kg=Gy
    D  <- r.el
    ii <- r.el <= r0; D[ii] <- k
    ii <- r.el > r0; D[ii] <- k * (r0/r.el[ii])^2
    ii <- r.el > R.e; D[ii] <- NA
    return(D)
}
```

B.2.2 Useful functions

```
####### Dosimeter energy account Ez.account.1 <-
function(E.start=10,p.tol=5,LET.tab=tab.LET,z.thick=0.05,
                          N.max=1e3,dens=3.97,E.min=1e-2){

    # This function keeps track of the energy account
    # as the proton penetrats the crystal of thickness z.thick.
    # E.start       = entrance proton energy        [MeV]
    # p.tol         = energy tolerance              [%]
    # LET.tab       = table to look up LET values   [MeV*cm^2/g]
    # names should be "MeV","LET",""R.max"
    # z.thick       = thickness of crystal          [cm]
    # N.max         = maximum number of iterations  [dimless]
    # dens          = material density              [g/cm^3]
    # E.min         = minimum proton energy         [MeV]

    # Created 08.27.06 by JE
```

```
# change LET units
dd <- LET.tab
dd$LET <- dd$LET*dens       #   [MeV/cm]
dd$R.max <-dd$R.max/dens    #   [cm]

# Start slab, initial values
LET <- approx(dd$MeV,dd$LET,xout=E.start)$y
dE <- E.start*p.tol/100
dz <- dE*LET^(-1)           # Approximation: LET constant in dE
E <- E.start
z <- 0
E.dep <- dE
i <- 1

# Vectors
E.vec <- E.start; dE.vec <- dE; z.vec <-0; dz.vec <- dz
LET.vec <- LET; E.dep.vec <- E.dep; i.vec <- i

# Iteration
repeat{
    # dz>>z.thick (large energies or small crystals)
    if (dz>=z.thick){
        dz <- z.thick-z
        dE <- dz*LET
        E.dep <- dE
        # Update vectors
        dz.vec <- dz
        dE.vec <- dE
        E.dep.vec <- E.dep
        print("Only one energy deposition (large energy/small crystal)")
        break
    }
    # dE<<E.min (large crystals or small energies)
    if (E-dE <= E.min){
        dE <- E-E.min
        dz <- dE*LET^(-1)
        E.dep <- dE
        # Update vectors
        dz.vec <- dz
        dE.vec <- dE
        E.dep.vec <- E.dep
        print("Only one energy deposition (small energy/large crystal)")
        break
    }
    # Maximum number of iterations
    if (i>N.max){
        print ("Max number of iterations reached")
        break
    }
    # Normal iteration
    E <- E-dE                           # E for next slap
    z <- z+dz                           # start depth of next slap
    LET <- approx(dd$MeV,dd$LET,xout=E)$y # LET for next slap
    dE <- E*p.tol/100                   # dE next slap
    dz <- dE*LET^(-1)                   # size next slap
    i <- i+1                            # number of iterations
    # Last slap
    if (z+dz>=z.thick){
        dz <- z.thick-z
        dE <- dz*LET
        E.dep <- E.dep+dE
        # Update vectors
```

```
            E.vec <- c(E.vec,E); dE.vec <- c(dE.vec,dE);
            z.vec <-c(z.vec,z); dz.vec <- c(dz.vec,dz);
            LET.vec <- c(LET.vec,LET); E.dep.vec <- c(E.dep.vec,E.dep)
            i.vec <- c(i.vec,i)
            print("crystal thickness reached")
            break
        }
        # protons thermalized
        if (E-dE<=E.min){
            dE <- E-E.min
            dz <- dE*LET^(-1)
            z <- z+dz
            E.dep <- E.dep+dE
            # Update vectors
            E.vec <- c(E.vec,E); dE.vec <- c(dE.vec,dE);
            z.vec <-c(z.vec,z); dz.vec <- c(dz.vec,dz);
            LET.vec <- c(LET.vec,LET); E.dep.vec <- c(E.dep.vec,E.dep)
            i.vec <- c(i.vec,i)
            print("minimum energy reached")
            break
        }
        # Update vectors
        E.dep <- E.dep+dE                    # accumulated energy
        E.vec <- c(E.vec,E); dE.vec <- c(dE.vec,dE);
        z.vec <-c(z.vec,z); dz.vec <- c(dz.vec,dz);
        LET.vec <- c(LET.vec,LET); E.dep.vec <- c(E.dep.vec,E.dep)
        i.vec <- c(i.vec,i)
    }
    dat <- data.frame("E"=E.vec,"dE"=dE.vec,"z"=z.vec,"dz"=dz.vec,
    "LET"=LET.vec,"E.dep"=E.dep.vec,"i"=i.vec)
}

####### Maximum delta-ray range

delta.max <-
function(E.p,k.el=6.13e-6,z.ch=1,alp=1.67,alp.low=1.079,dens=3.97){

    # Electron energy calculation for protons
    # CONSTANTS
    m.e     <- 9.1093836e-28    # mass electron                    [g]
    c.l     <- 2.99792458e10    # speed of light                   [cm/s]
    e       <- 4.806529593e-10  # charge of electron               [g^(1/2)*cm^(3/2)*s^(-1)]
    m.p     <- 1.6726217e-24    # mass of proton                   [g]
    # CALCULATION ENERGY CONSTANT
    E0      <- m.p*c.l^2*(1.602e-13)^(-1)*1e-7  # mass -> energy    [MeV]
    b       <- (1-(E0/(E.p+E0))^2)^(0.5)        # rel. speed of HCP [dimless]
    Je      <- 6.242e5                          # J -> MeV          [MeV]
    E.el    <- 2*m.e*Je*c.l^2*b^2/(1-b^2)       # max. elec. energy [MeV]
    if(E.el<1e-3){alp<-alp.low}                 # different alp for low-energy electrons
    R.max   <- k.el*(1/dens)*(1e3*E.el)^(alp)   # max. elec. range  [cm]
    }

####### Energi deposition by delta-rays

E.delta <-
function(E,R.e=delta.max,a0=1e-8,point.integrand=point.dose.int,
         dens=3.97,err=1e-16,N.el=1.2e24,log=F){
    # This function calculates the integral energy deposition
    # from delta-rays by the the Katz formula from a0 to R.max in
    # an infinitisimal thin slab of the dosimeter.
    # The output is given in J/cm.
    # The function is meant as input for the Hansen model.
```

```
    # E         = proton energy                 [MeV]
    # R.max     = maximum electorn range        [cm]
    # a0        = core radius (start point)     [cm]
    # dens      = density of material           [g/cm^3]

    # Created 10.09.2006 by JE
    # Revised 25.10.2006 by JE (log transform)

    R.max <- R.e(E)

    # Total energy deposited in track
    if (!log){
    if(R.max < a0) {a0 <- R.max;E.track <- 0;return(E.track);break}
    E.track <- 1e-3*dens*2*pi*integrate(point.integrand,lower=a0,upper=R.max,rel.tol=err,
                N.el=N.el,E.p=E,dens=dens,log=F,rel.tol=1e-20)$integral # J/cm
    return(E.track)
    }
    # INTEGRATE IN LOG SPACE
    if (log){
    if(R.max < a0) {a0 <- R.max;;E.track <- 0;return(E.track);break}
    E.track <- 1e-3*dens*2*pi*integrate(point.integrand,lower=log(a0),upper=log(R.max),rel.tol=err,
                 N.el=N.el,E.p=E,dens=dens,log=log)$integral # J/cm
    return(E.track)
    }
}
```

Acknowledgements

Scientific insight is usually acquired as the result of the input, help and discussion from many different researchers who, in addition to dissecting and clearing up a complicated physical problem, can add new aspects that you would not have thought about otherwise. This thesis is no exception, and my work as well as my development as a scientist benefited tremendously from the people I encountered and worked with throughout my PhD study.

In the beginning of 2004, I started as a PhD student at Risø National Laboratory. In this period, I shared an office with Kristina Thomsen and Marianne Aznar. They both helped me get started and suggested literature that introduced the subject of optically stimulated luminescence (OSL). I would like to thank Kristina who helped me with various LaTeX problems and ended up saving me a lot of time. Like me, Marianne was a part of the "Risø fiber group" working with medical luminescence dosimetry. I was fortunate enough to experience one of Marianne's clinical *in vivo* experiments and I am grateful for the constructive discussions we had. Towards the end of my PhD study, I again benefited from reading Marianne's thesis.

In July 2004, I attended the 14th Solid State Dosimetry conference to present my first paper in the USA. It was a hectic period both prior to and during the conference. Here, I greatly appreciated the skilled experience, input, criticism and help I got from two "heavy weighters" within the field of OSL, namely Andrew Murray and Lars Bøtter-Jensen.

The first part of 2005 evolved around the temperature aspects of the thesis. I would like to thank Flemming Kjær-Kristoffersen for providing a clinical experimental facility and the technical staff at Risø for producing several devices that made it possible to study the temperature effects experimentally. Although I never met him in person, I want to show my gratitude to Niels Agersnap Larsen. I learned a lot from reading his thesis and was able to use his programming to study aspects of the thermal excitation mechanisms that would otherwise not have been possible.

In the last part of 2005, the PhD study began to investigate the effects of protons on the luminescence response. This started out in Uppsala, Sweden

where we got beam time at the Theodor Svedberg institute. During this time, I had the pleasure of working with Joakim Medin whose great knowledge on protons and Monte Carlo modeling stimulated many useful discussions. After Uppsala, we got beam time together with Mayank Jain at the Poul Scherrer Institute in Switzerland. I would like to express my appreciation for the many rewarding conversations Mayank and I had on OSL in general, and protons in particular.

In the beginning of 2006, I went to spend half a year in Steve McKeever's laboratory at Oklahoma State University (OSU), USA. It was a fascinating time and I discovered many new perspectives on the OSL technique and the Al_2O_3:C material. Here I mostly worked with Eduardo Yukihara and Gabriel Sawakuchi. Eduardo has achieved great knowledge on OSL based dosimetry and possesses an impressive level of scientific skills. I had a great time working with him. When I got to OSU, Gabriel and I were both beginning to work with track structure theory but from different perspectives. Through countless scientific discussions at the whiteboard and computer, we established a highly creative environment from which we both benefited. I would like to thank Gabriel for this excellent cooperation. During this period I also learned a lot about track structure theory by reading Johnny W. Hansen's PhD thesis. I would like to express my gratitude to David Klein who introduced me to the medical OSL project at OSU and the experimental side of the pulsed OSL technique. Also, I want to acknowledge Eric Benton who made it possible for me to do experiments at the medical proton facility in Loma Linda, Carlifornia. In addition, new perspectives were added to my scientific knowledge by the input from Steve McKeever and Mark Akselrod who are also two "heavy weighters" within the field of OSL. My time in Oklahoma allowed me to grow both professionally and personally, and I highly recommend that other PhD students participate in an external laboratory for a period of time during their PhD study.

In August 2006, I returned to Risø from Oklahoma. I now had to apply the track structure theory to the experimental data from the Poul Scherrer institute and write my thesis. Through this last intense period of my PhD, I shared an office with the new post doc in the group, Steffen Greilich. Like me, he was interested in modeling protons through matter although he mainly focused on the radioluminescence signal and Monte Carlo simulation. We had many stimulating conversations on modeling and shared a constructive working environment. I want to thank Steffen for his interesting and useful contributions. During this time, a couple of workshops on modeling the interaction of heavy ions with matter were organized and I deeply appreciate the many insightful discussions I had with Niels Bassler, Johnny W. Hansen and Kjeld Olsen.

I would also like to thank my supervisor at the University of Copenhagen Stig Steenstrup. He was my supervisor from the very beginning of my academic career and, like he did in this PhD project, helped me take care of all administrative matters concerning the university.

Finally I want express my deepest gratitude to my supervisor at Risø, Claus Erik Andersen. He was, without question, my closest coworker through the entire PhD study. At one of our first encounters, Claus gave me a logbook with the comment: "You are going to need this." It was true, indeed I did. This example illustrates some of the admirable qualities that Claus possesses as a supervisor: a genuine concern for his students and a willingness to pass on the experience and knowledge that he has acquired. Throughout the whole PhD study, the door to Claus's office was always open, literally and figuratively. If I had a question, he would not hesitate to put his phone on the answering machine so we would not be interrupted. If Claus had not heard from me in a while, he would often check on me to see if I was stock on a problem with which he could help. I truly appreciate Claus's concern and dedication to my project and to me. Through conversations with other PhD students I have learned that they, in addition to the process of writing a thesis, faced extra challenges because their supervisor was rarely available and/or knew little about the details of their work. This was never a problem for me and my work benefited tremendously from Claus's remarkable guidance. Claus definitely helped me develop as a scientist and equipped me with many research skills that I profit from in my work today as a medical physicist.

I would like to end with a little scientific note. In 2003, I finished my masters thesis on laser light scattered by a solution of proteins. It was my first real encounter with matter's interaction with electromagnetic radiation. This process mainly takes place through classical Rayleigh scattering, i.e. with no energy loss. There is a negligible contribution from the other processes by which photons interact with matter, namely through the photo electric effect, the Compton effect and pair production. At that time, I had no idea that four years later I would finish a PhD thesis that primarily focuses on the latter three interaction schemes completely neglecting the Rayleigh component.

Jens Morgenthaler Edmund
Copenhagen, November 2007

References

[1] N. Agersnap. *Dosimetry based on thermally and optically stimulated luminescence*. Risø-R-1090(EN). Risø National Laboratory, Roskilde (Denmark), 1999.

[2] N. Agersnap, L. Bøtter-Jensen, and S.W.S. McKeever. Thermally stimulated conductivity and thermoluminescence from Al_2O_3:C. *Radiation Protection Dosimetry*, 84:87–90, 1999.

[3] A.E. Akselrod and M.S. Akselrod. Correlation between OSL and the distribution of TL traps in Al_2O_3:C. *Radiation Protection Dosimetry*, 100:217–220, 2002.

[4] M. S. Akselrod, 2006. private correspondance.

[5] M.S. Akselrod, N. Agersnap, V. Whitley, and S.W.S. McKeever. Thermal quenching of F-center luminescence in Al_2O_3:C. *Journal of Applied Physics*, 84:3364–3373, 1998.

[6] M.S. Akselrod, V.S. Kortov, and E.A. Gorelova. Preparation and properties of alpha-Al_2O_3:C. *Radiation Protection Dosimetry*, 47:159–164, 1993.

[7] M.S. Akselrod, V.S. Kortov, D.J. Kravetsky, and V.I. Gotlib. Highly sensitive thermoluminescent anion-defective alpha-Al_2O_3:C. *Radiation Protection Dosimetry*, 32:15–20, 1990.

[8] M.S. Akselrod, A.C. Lucas, J.C. Polf, and S.W.S. McKeever. Optically stimulated luminescence of Al_2O_3. *Radiation Measurements*, 29:391–399, 1998.

[9] M.S. Akselrod and S.W.S. McKeever. A radiation dosimetry method using pulsed optically stimulated luminescence. *Radiation Protection Dosimetry*, 81:167–175, 1999.

[10] C.E. Andersen, M.C. Aznar, L. Bøtter-Jensen, S. Å. J. Bäck, S. Mattsson, and J. Medin. Development of optical fibre luminescence techniques for real time in vivo dosimetry in radiotherapy. *IAEA, Vienna*, 2:353–360, 2003.

[11] C.E. Andersen, L. Bøtter-Jensen, and A.S. Murray. A mini x-ray generator as an alternative to a $^{90}Sr/^{90}Y$ beta source in luminescence dating. *Radiation Measurements*, 37:557–561, 2003.

[12] C.E. Andersen, J.M. Edmund, J. Medin, E. Grusell, M. Jain, and S. Mattsson. Medical proton dosimetry using radioluminescence from aluminium oxide crystals attached to optical fiber cables. *Nucl. Instrum. Meths A*, 580:466–468, 2007.

[13] C.E. Andersen, C.J. Marckmann, M.C. Aznar, L. Bøtter-Jensen, F. Kjaer-Kristoffersen, and J. Medin. An algorithm for real-time dosimetry in intensity-modulated radiation therapy using the radioluminescence signal from Al_2O_3:C. *Radiation Protection Dosimetry*, 120:7–13, 2006.

[14] M.C. Aznar. *Real-time in-vivo luminescence dosimetry in radiotherapy and mammography using Al_2O_3:C.* Risø-PhD-12(EN). Risø National Laboratory, Roskilde (Denmark), 2005.

[15] M.C. Aznar, C.E. Andersen, L. Bøtter-Jensen, S. Å. J. Bäck, S. Mattsson, F. Kjaer-Kristoffersen, and J. Medin. Real-time optical-fibre luminescence dosimetry for radiotherapy: physical characteristics and applications in photon beams. *Physics in medicine and biology*, 49:1655–1669, 2004.

[16] M.C. Aznar, B. Hemdal, J. Medin, C.J. Marcmann, C.E. Andersen, L. Bøtter-Jensen, I. Adersson, and S. Mattsson. In vivo absorbed dose measurements in mammography using a new real-time luminescence technique. *British Institute of Radiology*, 78:328–334, 2005.

[17] N. Bassler. *Antiproton cancer therapy.* PhD thesis, University of Aarhus, Denmark, 2006.

[18] Kræftens bekæmpelse, 2007. www.cancer.dk.

[19] J. Bethe. In E. Segré, editor, *Experimental nuclear physics, vol. 1*, page 166. John Wiley and Sons, London (UK), 1953.

[20] A.J.J. Bos. On the energy conversion in thermoluminescence dosimetry materials. *Radiation Measurements*, 33:737–744, 2001.

[21] L. Bøtter-Jensen. *Developments of optically stimulated luminescence tecniques using natural materials and ceramics, and their application to retrospective dosimetry.* Risø-R-1211(EN). Risø National Laboratory, Roskilde (Denmark), 1984.

[22] L. Bøtter-Jensen, S.W.S. McKeever, and A.G. Wintle. *Optically Stimulated Luminescence Dosimetry.* Elsevier Science B. V., 1 edition, 2003.

[23] J.J. Butts and R. Katz. Theory of RBE of heavy ion bombardment of dry enzymes and viruses. *Radiation research*, 30:855–871, 1967.

[24] R. Chen, V. Pagonis, and J.L. Lawless. The nonmonotonic dose dependence of optically stimulated luminescence in Al_2O_3:C. analysis and numerical simulation results. *Journal of Applied Physics*, 99:033511, 2006.

[25] Z. Chen, F. dErrico, and R. Nath. Principles and requirements of external beam dosimetry. *Radiation Measurements*, 41:2–21, 2006.

[26] M.A. Clift, P.N. Johnston, and D.V. Webb. A temporal method of avoiding the cerenkov radiation generated in organic scintillator dosimeters by pulsed mega-voltage electron and photon beams. *Physics in medicine and biology*, 31:1421–1433, 2002.

[27] P. Dalgaard. *Introductory statistics with R.* Springer Verlag, New York (USA), 2002.

[28] R. Gaza. *A fiber-optics, real-time dosimeter based on optically stimulated luminescence of Al_2O_3:C and KBr:Eu, for potential use in radiotherapy of cancer.* PhD thesis, Oklahoma State University, May 2004.

[29] R. Gaza, E.G. Yukihara, and S.W.S. McKeever. The response of thermally and optically stimulated luminescence Al_2O_3:C to high-energy heavy charged particles. *Radiation Measurements*, 38:417–420, 2004.

[30] O.B. Geiß. Efficiency of thermoluminescent detectors to heavy charged particles. *Nucl. Instrum. Meths B*, 142:592–598, 1998.

[31] K. Günter and W. Schulz. *Biophysical theory of radiation action.* Akademie-Verlag, Berlin (Germany), 1983.

[32] dr. med. N. E. Hansen. Kræftens bekæmpelse, 2007. private correspondance.

[33] J.W. Hansen. *Experimental investigation of the suitability of the track structure theory in describing the relative effectiveness of high-LET irradiation of physical radiation detectors.* Risø-R-507. Risø National Laboratory, Roskilde (Denmark), 1984.

[34] J.W. Hansen and K.J. Olsen. *High-LET dose-response characteristics described by track structure theory of heavy charged particles.* Risø-M-2308. RisøNational Laboratory, Denmark, 1981.

[35] J.W. Hansen and K.J. Olsen. Experimental and calculated response of a radiochromic dye film dosimeter to high-LET radiations. *Radiation Research*, 97:1–15, 1984.

[36] P.C. Hansen. Regularization tools. (notes), Technical University of Denmark, Denmark, 1993.

[37] P.C. Hansen. Regularization tools: A Matlab package for analysis and solution of discrete ill-posed problems. *Numerical algorithms*, 6:1–35, 1994.

[38] World Health Organization (WHO). www.who.int/topics/cancer/en/.

[39] Y. Horowitz and P. Olko. The effects of ionisation density on the thermoluminescence response (efficiency) of LiF:Mg,Ti and LiF:Mg,Cu,P. *Radiation Protection Dosimetry*, 109:331–348, 2004.

[40] Y.S. Horowitz. *Thermoluminescence and thermoluminescencent dosimetry*, volume 2. CRC Press, Inc., 1984.

[41] Y.S. Horowitz. Theory of thermoluminescence gamma dose response: The unified interaction model. *Nucl. Instrum. Meths B*, 184:68–84, 2001.

[42] Y.S. Horowitz, Belaish Y., and L. Oster. Theories of TL systems: Failures, sucesses, conflicts, trends: Insights into the possible future materials and techniques. *Radiation Protection Dosimetry*, 119:124–129, 2006.

[43] A.L. Huston, B.L. Justus, P.L. Falkenstein, R.W. Miller, H. Ning, and R. Altemus. Remote optical fiber dosimetry. *Nucl. Instrum. Meths B*, 184:55–67, 2001.

[44] G. Hütt, I. Jack, and J. Tchonka. Oprical dating: K-feldspars optical response stimulation spectra. *Quaternary Science Reviews*, 7:381–385, 1988.

[45] ICRP. Fundamental quantities and units for ionizing radiation. *Annals of ICRP*, 21, 1998. ICRP publication 60.

[46] ICRP. Prevention of accidents to patients undergoing radiotherapy. *Annals of ICRP*, 30, 2000. ICPR publication 86.

[47] ICRU. *Stopping Powers and Ranges for Protons and Alpha Particles*. ICRU Report 49. International Commission on Radiation Units and Measurements, 1993.

[48] M. Jain, C.E. Andersen, W. Hajdas, J.M. Edmund, and L. Bøtter-Jensen. Luminescence resoponse to proton irradiation in some natural dosemeters: implications for maritan sediment dating. *Nucl. Instrum. Meths A*, 2007. doi:10.1016/j.nima.2007.05.112.

[49] H.E. John and J.R. Cunningham. *The Physics of Radiology*. Thomas, Springfield, Illinois, USA, 4th edition, 1983.

[50] B.L. Justus, P. Falkenstein, A.L. Huston, M.C. Plazas, H. Ning, and R.W. Miller. Gated fiber-optic-coupled detector for in vivo real-time radiation dosimetry. *Applied Optics*, 43:1663–168, 2004.

[51] R. Katz. Track structure theory in radiobiology and in radiation detection. *Nuclear track detection*, 2:1–28, 1978.

[52] R. Katz, S.C. Sharma, and M. Homayoonfar. The structure of particle tracks. In F. H. Attix, editor, *Topics in radiation dosimetry, Supplement 1*, page 317. Academic press, New York (USA), 1972.

[53] J. Kiefer and H. Straaten. A model of ion track structure based on classical collision dynamics. *Physics in Medcine and Biology*, 11:1201–1209, 1986.

[54] A.H. Kitai. *Solid state luminescence, theory, materials and devices*. Chapman & Walker, London (England), 1993.

[55] K.H. Lee and J.H. Crawford Jr. Luminescence of the F center in sapphire. *Physical Review B*, 19(6):3217–3221, 1979.

[56] R.L. Liboff. *Introduction to quantum mechanics*. Addison-Westley, USA, 3 edition, 1998.

[57] C.J. Marckmann, C.E. Andersen, M.C. Aznar, and L. Bøtter-Jensen. Optical fibre systems for clinical applications based on radioluminescence and optically stimulated luminescence from Al_2O_3:C. *Radiation Proctective Dosimetry*, 120:28–32, 2006.

[58] B.G. Markey, S.W.S. McKeever, M.S. Akselrod, and L. Bøtter-Jensen. The temperature dependence of optically stimulated luminescence from α-Al_2O_3:C. *Radiation Protection Dosimetry*, 65:185–189, 1996.

[59] S.W.S. Mckeever. *Thermoluminescence of solids*. Cambridge university press, NY (USA), 1985.

[60] S.W.S. McKeever. Optically stimulated luminescence dosimetry. *Nucl. Instrum. Meths B*, 184:29–54, 2001.

[61] S.W.S. McKeever. New millennium frontiers of luminescence dosimetry. *Radiation Proctive Dosimetry*, 100:27–32, 2002.

[62] S.W.S. McKeever, N. Agersnap, L. Bøtter-Jensen, and V. Mejdahl. OSL sensitivity changes during single aliquot procedures: Computer simulations. *Radiation Measurements*, 27:75–82, 1997.

[63] S.W.S. McKeever and M.S. Akselrod. Radiation dosimetry using pulsed optically stimulated luminescence of Al_2O_3:C. *Radiation Protection Dosimetry*, 84:317–320, 1999.

[64] S.W.S. McKeever, M.S Akselrod, and B.G. Markey. Pulsed optically stimulated luminescence dosimetry using α-Al_2O_3:C. *Radiation Protection Dosimetry*, 65:267–272, 1996.

[65] S.W.S. McKeever, L. Bøtter-Jensen, N. Agersnap, and G.A.T. Duller. Temperature dependence of OSL decay curves: Experimental and theoretical aspects. *Radiation Measurements*, 27:161–170, 1997.

[66] S.W.S. McKeever, M. Moscovitch, and P.D. Townsend. *Thermoluminescence dosimetry materials: Properties and uses*. Nuclear Technology Publishing, 1995.

[67] P.W. Milonni and J.H. Eberly. *Lasers*. John Wiley & sons, USA, 1988.

[68] P. Olko, P. Bilski, N.A. El-Faramawy, H.Y. Göksu, J.L. Kim, and R. Kopec. On the relationship between dose-, energy- and LET-response of thermoluminescent detectors. *Radiation Protection Dosimetry*, 119:15–22, 2006.

[69] Paul Scherrer Institute. *Proton therapy at the Paul Scherrer Institute*. Paul Scherrer Institute, Villingen (Swizerland), 2004.

[70] C. Pedrini. Scintillation mechanisms and limiting factors on each step of relaxation of electronic excitations. *Physics of solid state*, 47:1406–1411, 2005.

[71] J.C. Polf. *A study of optically stimulated luminescence in Al_2O_3:C fibers for development of a real-time, fiber optic dosimetry system*. PhD thesis, Oklahoma State University, August 2002.

[72] J.C. Polf, S.W.S. McKeever, M.S. Akselrod, and S. Holmstrom. A real-time, fibre optic dosimetry system using Al_2O_3:C fibres. *Radiation Protection Dosimetry*, 100:301–304, 2002.

[73] J.C. Polf, E.G. Yukihara, M.S. Akselrod, and S.W.S. McKeever. Real-time luminescence from Al_2O_3:C fiber dosimeters. *Radiation Measurements*, 38:227–240, 2004.

[74] N.R.J. Poolton, L. Bøtter-Jensen, and O. Johnsen. Thermo-optical properties of optically stimulated luminescence in feldspars. *Radiation Measurements*, 24:329–333, 1995.

[75] N.R.J. Poolton, L. Bøtter-Jensen, P.J.M Ypma, and O. Johnsen. Influence of crystal structure on the optically stimulated luminescence properties of feldspars. *Radiation Measurements*, 23:551–554, 1994.

[76] N.R.J. Poolton, E. Bulur, J. Wallinga, L. Bøtter-Jensen, and A.S. Murray. An automated system for the analysis of variable temperature luminescence. *Nucl. Instrum. Meths B*, 179:575–584, 2001.

[77] W.H. Press, S.A. Teukolsky, W.T. Vetterling, and B.P Flannery. *Numerical recipes in fortran*. Cambridge university press, 2nd edition, 1992.

[78] J. E. Rodgers. Monte Carlo simulations of dose deposition applied to clinical radiation therapy. *Radiation Measurements*, 41:36–44, 2006.

[79] S. Safai, S. Lin, and E. Pedroni. Development of inorganic scintillating mixtures for proton beam verification dosimetry. *Physics in Medicine and Biology*, 49:4637–4655, 2004.

[80] M. Scholtz and G. Kraft. Track structure and the calculation of biological effects of heavy charged paritcles. *Adv. Space Res.*, 18:5–14, 1995.

[81] D. Schultz-Ertner, O. Jägel, and W. Schlegel. Radiation therapy with charged particles. *Seminars in Radiation Oncology*, 16:249–259, 2006.

[82] W.U. Shipley, J.E. Tepper, G.R. Prout Jr., L.J. Verhey, O.A. Mediondo, M. Goitein, A.M. Koehler, and H.D. Suit. Proton radiation as boost therapy for localized prostatic carcinoma. *J. Am. Med. Assoc.*, 241:1912–1915, 1979.

[83] Siemens Medical solutions. *Particle therapy - getting to the point*. Siemens AG, (CA) USA, 2004.

[84] B. Spielberger, M. Scholtz, M. Krämer, and G. Kraft. Calculation of the X-ray response to heavy charged particle irradiation. *Physics in Medicine and Biology*, 47:4107–4120, 2002.

[85] F. Spurný. Response of thermoluminescent detectors to charged particles and to neutrons. *Radiation Measurements*, 38:407–412, 2004.

[86] R. Stanton and D. Stinson. *An introduction to radiation oncology physics*. Medical physics publishing, Wisconsin (USA), 1992.

[87] Sundhedsstyrelsen. *National kræftplan : status og forslag til initiativer i relation til kræftbehandlingen*. Sundhedsstyrelsen, Copenhagen (Denmark), 2000.

[88] W.N. Venables and B.D. Ripley. *Modern applied statistics with S*. Springer Verlag, New York (USA), 4th edition, 2002.

[89] M.P.R. Waligórski, R.N. Hamm, and R. Katz. The radial distribution of dose around the path of a heavy ion in liquid water. *Nuclear Tracks Radiation Measurements*, 11:309–319, 1986.

[90] M.P.R. Waligórski and R. Katz. Supralinearity of peak 5 and peak 6 in TLD-700. *Nucl. Instrum. Meths*, 172:463–470, 1980.

[91] M.P.R. Waligórski and R. Katz. Supralinearity of peak 5 and peak 6 in TLD-700. *Nucl. Instrum. Meths*, 175:48–50, 1980.

[92] M.P.R. Waligórski, P. Olko, P. Bilski, M. Budzanowski, and Niewiadomski T. Dosimetric characteristics of LiF:Mg,Cu,P phosphors - a track structure interpretation. *Radiation Protection Dosimetry*, 47:53–58, 1993.

[93] V.H. Whitley and S.W.S. McKeever. Photoionization of deep centres in Al_2O_3:C. *Journal of Applied Physics*, 87:249–256, 2000.

[94] V.H. Whitley and S.W.S. McKeever. Linearly modulated photoconductivity and linearly modulated optically stimulated luminescence measurements on Al_2O_3:C. *Journal of Applied Physics*, 90:6073–6083, 2001.

[95] E. Yukihara, R. Gaza, S.W.S. McKeever, and C.G. Soares. Optically stimulated luminescence and thermoluminescence efficiencies for high-energy heavy charged particle irradiation of Al_2O_3:C. *Radiation Measurement*, 38:59–70, 2004.

[96] E.G. Yukihara and S.W.S. McKeever. Ionization density dependence of the optically and thermally stimulated luminescence from Al_2O_3:C. *Radiation Protection Dosimetry*, 119:206–217, 2006.

[97] E.G. Yukihara, G.O. Sawakuchi, S. Guduru, S.W.S. McKeever, R. Gazab, E.R. Benton, N. Yasuda, Y. Uchihori, and H. Kitamura. Application of the optically stimulated luminescence (OSL) technique in space dosimetry. *Radiation Measurements*, 41:1126–1135, 2006.

[98] E.G. Yukihara, V.H. Whitley, S.W.S. McKeever, A.E. Akselrod, and M.S. Akselrod. Effect of high-dose irradiation on the optically stimulated luminescence of Al_2O_3:C. *Radiation Measurements*, 38:317–330, 2004.

[99] E.G. Yukihara, V.H. Whitley, J.C. Polf, D.M. Klein, S.W.S. McKeever, A.E. Akselrod, and M.S. Akselrod. The effects of deep trap population on the thermoluminescence of Al_2O_3:C. *Radiation Measurements*, 37:627–638, 2003.

Risø's research is aimed at solving concrete problems in the society.

Research targets are set through continuous dialogue with business, the political system and researchers.

The effects of our research are sustainable energy supply and new technology for the health sector.